Optimisation of Heusler Alloy Thin Films for Spintronic Devices

James Sagar

Submitted for the Degree of Doctor of Philosophy

The University of York

Department of Physics

July 2013

Abstract

Heusler alloys are one of the leading candidate material classes for achieving high spin polarisation. A number of Co-based Heusler alloys are predicted to be half-metallic ferromagnets that would theoretically provide 100% spin polarisation at the Fermi energy. However, there are yet to be any reports of this 100% spin polarisation experimentally. To develop these materials as a viable spin source their magnetic and structural properties must be fully characterised and optimised.

In this study both epitaxial and polycrystalline thin films have been deposited and their structural and magnetic properties studied in detail using a wide variety of magnetometry and electron microscopy techniques. The polycrystalline films form an amorphous matrix in the as-deposited state which crystallises into ordered grains after annealing at 235°C. These films have a wide range of magnetic and structural properties due to the crystallisation processes. Films are found to exhibit magnetisation reversal by both single domain particle rotation and domain wall processes which lead to coercivities ranging from 100 Oe to 2000 Oe. The individual grains themselves are found to be highly ordered into the $B2$ or $L2_1$ crystal phases. In the single crystal films long range $L2_1$ ordering is observed, the extent of which increases monotonically with annealing temperature. These films also show extremely low coercivities <30 Oe. The magnetisation reversal is controlled by a series of misfit dislocations at the film substrate interface which could make these films potentially unsuitable for device applications.

To control the magnetic and structural properties a number of seed layers have been tested. Ag seed layers were found to reduce the coercivity of the polycrystalline films to similar values to those found for the singe crystal films (H_c <50 Oe). The Ag seed layer exhibits island growth resulting in Co_2FeSi grain segregation which reduces the loop squareness. The island growth can be removed and the squareness restored through the use of Cr buffer layers before the Ag layers. This reduces film roughness to sub 1 nm therefore approaching the conditions that are required for device fabrication.

Contents

List of Figures

Acknowledgments

This thesis and the work within would never have been possible without the help and support of a large number of people. First and foremost I would like to acknowledge my supervisors Dr. Atsufumi Hirohata and Prof. Kevin O'Grady. Their guidance and support has made this all possible.

I would also like to thank the JST and EPSRC for funding the last three years. This collaborative research grant has given me the opportunity to visit the magnetic materials unit at the National Institute for Materials Science (NIMS) in Tsukuba. My visits there proved fruitful and were made all the more memorable by my supervisor there Dr. Seiji Mitani, as well as Dr. Hiroaki Sukegawa who helped to carry out all the work there.

I have also had a lot of support from other researchers at York, particularly Dr. Vlado Lazarov and Dr. Leonardo Lari without whom much of my microscopy would not have been possible.

I must also thank all the residents of S/020 past and present who have made the last three years so enjoyable. There are too many people to name them all individually however I must make special mention to Luke who taught me how to use most of the kit in the lab and to Ben who is always willing to join me in the pub after a hard day.

Most of all I want to thank Laura who is there for me whenever I need her despite being at the opposite end of the east coast mainline. She is always the voice of reason that makes sure I keep going in the right direction. Her continued support has given me the drive to make this possible.

Thank you all so much!

Declaration

I declare that the work presented in this thesis is based purely on my own research, unless otherwise stated, and has not been submitted for a degree in this or any other university

Signed

James Sagar

July 2013

Chapter 1. Introduction

Since the discovery of giant magnetoresistance (GMR) spintronics has become a field of intense commercial and research interest. A magnetoresistive sensor can be found in the read head of every hard disk drive sold every year. The field of spintronics continues to grow with renewed interest and vigour as second generation magnetic random access memory (MRAM) becomes commercially viable. All spintronic devices need a source of spins. This is usually in the form of a ferromagnet. However, these typical transition metal ferromagnets have low spin polarisation or low spin injection efficiency, typically less than 50%. Half-metallic ferromagnets are a leading candidate to replace current materials and offer much greater spin polarisation, possibly up to 100%. However there are a number of key issues that must be overcome before these films can be used in commercial devices.

1.1. Spintronics

Today the integrated circuit and semiconductors are the backbone of modern technology. Complementary metal-oxide-semiconductor (CMOS) and metal-oxide-semiconductor field effect transistor (MOSFET) technologies form the building blocks of this backbone **[1]**. In recent years there have been a number of astonishing advances in this technology, driven by advances in the scalability of these devices. The drive towards the current state of technology is due to Moore's law **[2]** which states that the number of transistors on a single chip doubles every 18 months. This has held true for over 30 years to the point where today's most advanced home computer components have 7.1bn transistors per chip **[3]**. However, this trend cannot continue. We are approaching the physical limit where these devices can function, either due to high leakage currents **[4]** or simply the limitations of lithography to pattern them. This technological advancement is mirrored in the magnetic storage industry where the

same trend is seen for areal density, information stored per unit area. However this is beginning to plateau due to material limitations in both the hard disk and the read head sensor. New technologies are required to overcome these difficulties and continue the technological advance.

Spin-electronics is a promising candidate to allow further development of current semiconductor technologies as it is widely used in the hard disk industry for read head sensors. This means that the processes for commercialising spintronics are already in-place. To improve spintronic devices beyond their current limitations new materials and device technologies must be implemented. Spintronics is a field comprising many sub disciplines although these can be broadly divided up into semiconductor spintronics **[5]** and magnetoelectronics **[6,7]**. The latter is concerned with all metallic systems such as magnetoresistive devices and will form most of the foundation of this work.

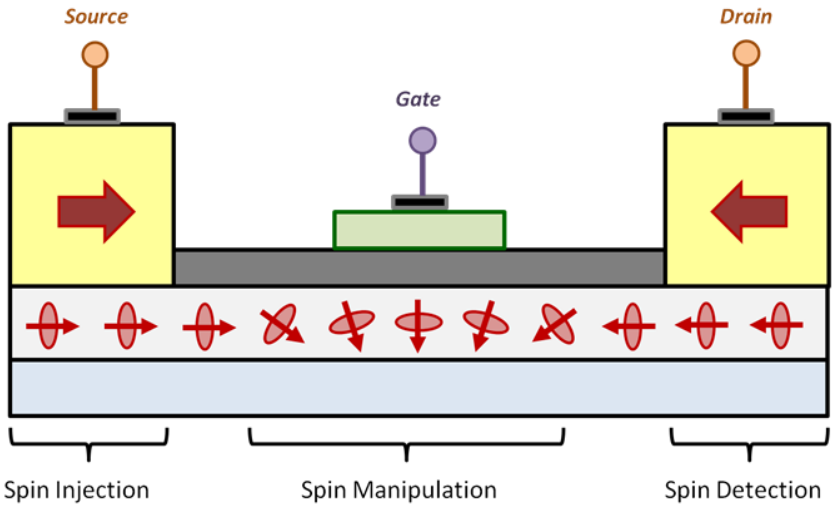

Figure 1.1. Schematic diagram of Datta-Das SpinFET. **[8]**

Spintronics is based around the concept of using quantised angular momentum, spin, of an electron instead of or as well as its charge. Although the effects of the spin of the electron had been observed experimentally in the late 19th century it was not defined until the early 20th century by *Dirac*. In 1857 *Lord Kelvin* (formally W. Thomson) observed anisotropic magnetoresistance (AMR) **[9]** . AMR is the directional dependence of the resistivity of a material relative to a magnetic field. AMR is one of many forms of magnetoresistance which shall be discussed more thoroughly in the next section. Since these early observations of spin dependent electron transport

many different devices have been designed and fabricated all using slightly different spin dependent phenomena. The most basic and best example of the requirements of a spintronic device is the spin field effect transistor (SpinFET) as designed by *Datta* and *Das* **[8]**, shown in Figure 1.1.

This work is primarily concerned with the spin source where a high spin polarisation is required. The simplest spin source is a typical ferromagnet interfaced with non-magnetic metal or semiconductor. The Heusler alloys used in this work are intended for use in such a spin source. However spin generation has also been achieved through the manipulation of magnetisation dynamics, resulting in a phenomenon known as spin pumping **[10]**.

1.2. Magnetoresistance

Although AMR was discovered in 1857 it was mainly of academic importance due to it only having a small effect (a few per cent). It was used for a number of early hard disk designs until superseded by the discovery of other magnetoresistive effects such as giant magnetoresistance (GMR).

GMR was discovered in 1988 through electrical magnetotransport measurements of ferromagnetic/non-magnetic/ferromagnetic multi-layered systems. This was an attempt to further understand the dependence of interlayer exchange coupling on the spacer thickness in thin film multilayers **[11]**. *Grünberg* **[12]** and *Fert* **[13]** discovered the effect simultaneously while measuring Fe/Cr/Fe superlattices spaced sufficiently to induce antiferromagnetic coupling between the two Fe layers. The pair received the Nobel prize in Physics for their discovery in 2007. In their initial publications both observed a large change in resistance for the structures when the spaced magnetic layers were changed from anti-parallel to parallel alignment.

This was explained using the two current model initially proposed by *Mott* in 1936 **[14,15]**. Simply that the current through a transition metal can be separated into two spin channels. This model has since been extended by *Campbell* **[16]**and *Fert* **[17]** to include a large number of different electron scattering terms that provide better agreement with the experimental data. This effect in a GMR multilayer is often best explained pictorially as shown in Figure 1.2.

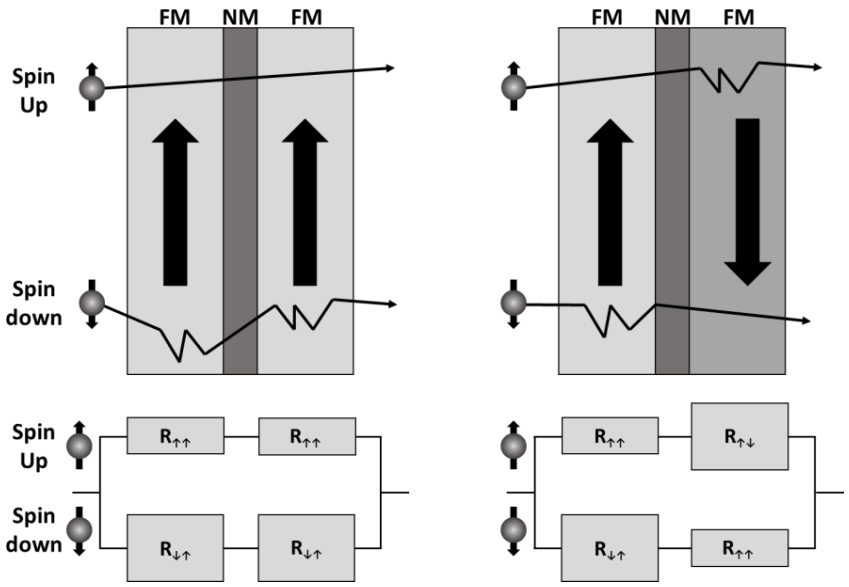

Figure 1.2. Schematic of the GMR effect **[18]**.

For the parallel aligned case, one spin channel experiences small or no spin scattering through both ferromagnetic layers. This leads to a low resistance state. In the anti-parallel aligned case, both spin channels experience spin scattering in one of the ferromagnetic layers leading to a high resistance state. Initially this effect was small (1.5% at room temperature) **[12]**. Since its discovery, large developments have seen the magnitude of the GMR effect increase to 34% at room temperature **[19]**. There have also been demonstrations of the effect in two different orientations, known as current-in-plane (CIP) and current-perpendicular-to-plane (CPP) **[18]**. These two orientations have a number of different properties, however CPP-GMR is the current focus of much research interest due to its applicability to current generation MRAM.

If the non-magnetic spacer is replaced by a non-metallic spacer then another phenomenon known as tunnelling magnetoresistance (TMR) can occur. This was first observed by *Julliere* in 1975 **[20]** with a resistance change of 14% between parallel and anti-parallel states at 4.2K. It was not until the early 1990s that this effect was observed at room temperature, initially by *Miyazaki* (18%) **[21]** and then by *Moodera* (11.8%) **[22]**. These experiments used amorphous insulating spacers such as AlO_x however, since the pioneering theoretical work of *Butler* in 2001 **[23]**, there has been much greater interest in using crystalline MgO barriers. These were predicted to allow TMR ratios of over 1000%. Experimentally, values of 600% at room temperature have

been achieved by *Ikeda et al.* using CoFeB/MgO/CoFeB multilayer films **[24]**. Although similar in many ways to GMR, TMR is fundamentally quite different.

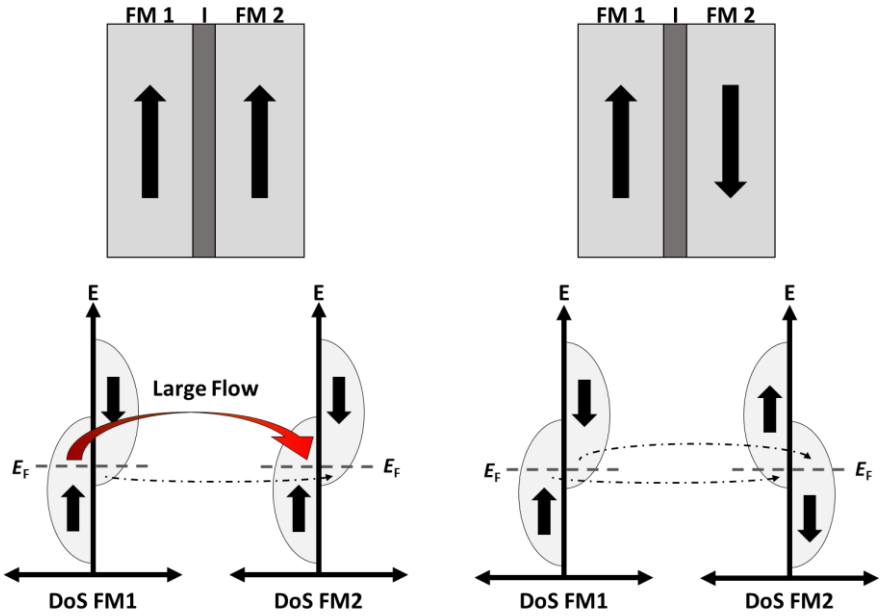

Figure 1.3. Schematic of the TMR effect.

TMR depends on the conduction states available to tunnel into across the barrier, not just the spin dependent scattering within the electrodes. This is shown schematically in Figure 1.3. For the parallel orientation there are a large number of majority conduction states and majority valance states resulting in a large electron flow and thus low resistance. For the anti-parallel orientation there are fewer majority and minority states resulting in a high resistance. This makes TMR dependent upon the number of available states for each spin direction at the Fermi energy or the spin polarisation, equation 1.1.

$$TMR = \frac{\Delta R}{R} = \frac{2P_1P_2}{1 - P_1P_2} \tag{1.1}$$

where P_1 and P_2 are the spin polarisations of ferromagnetic layers in the junction. This means that for Heusler alloys such as those studied in this work the achievable TMR should be extremely high due to large values of spin polarisation from these materials.

1.3. Spin Transfer Torques

The most promising new spintronic technology is MRAM. This will potentially replace current semiconductor based dynamic random access memory (DRAM). MRAM has a

large number of advantages, most importantly it is non-volatile. This means that when the power is turned off the information is retained. 1st generation MRAM used the Oersted field generated by a current carrying wire to write information to an array of magnetic spin valves. The 2nd generation of MRAM will use a phenomenon known as spin-transfer-torque (STT) as a much more efficient way to write data.

STT was first considered as a way to reverse the magnetisation in a magnetic multilayer by *Slonczewski* **[25]**. However the effect of spin transfer had been introduced by *Berger* 12 years earlier **[26]**. STT is easiest to consider in the case of a ferromagnetic/non-magnetic/ferromagnetic junction like those used for GMR. The two ferromagnetic layers have their magnetisations aligned at an angle to one another. When electrons flow into the junction they are initially aligned or polarised to the direction of the magnetisation in the first ferromagnetic layer. When the electrons then travel to the second ferromagnetic layer their spins align with the magnetisation of that layer. However as the spins align to the new direction of magnetisation they exert a torque on that magnetisation. This is the spin transfer torque. Figure 1.4 shows this effect schematically.

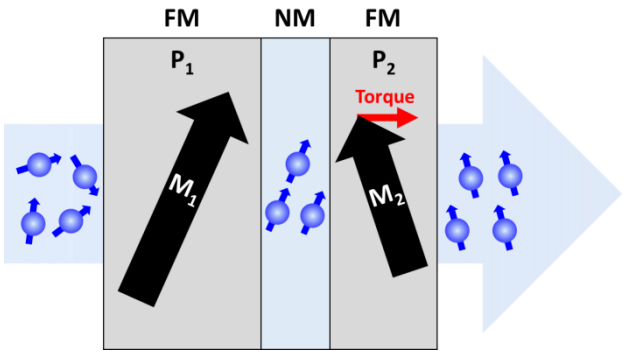

Figure 1.4. Schematic diagram of the spin transfer torque effect on magnetisation in a FM/NM/FM junction.

If a sufficient number of electrons are injected into the second ferromagnetic layer the torque can be large enough to overcome the torque due to the magnetisation of the material and as a result align the magnetisation of the second ferromagnetic layer M_2 with that of the first M_1. It is also possible to reverse the direction of M_2 back to its original state by injecting the electrons in the opposite direction. In this situation the spins align with M_2 and are then injected into M_1. However, those spins aligned antiparallel to M_1 are reflected back at the interface and injected back into the second ferromagnetic layer where they once again exert a torque on M_2. Thus the

magnetisation in one ferromagnetic layer can be switched by changing the polarity of the applied voltage. The form of the spin transfer torque is given by equation 1.2 **[10]**:

$$\tau_{STT} = \boldsymbol{M}_1 \times (\boldsymbol{M}_1 \times \boldsymbol{M}_2) P \frac{\gamma_{gm}}{M_s V e} I \qquad (1.2)$$

Here the cross products of the magnetisations M_1 and M_2 give the direction of the torque. The magnitude of the torque is then dictated by the spin polarisation of the ferromagnets P, the saturation magnetisation M_s, the volume of the magnetic layer on which the torque is acting V and the current applied to the junction I. γ_{gm} is the gyromagnetic ratio. The dependence of STT on the spin polarisation of the electrodes makes Heusler alloys a promising candidate for use in these devices due to their high spin polarisation. A detailed examination of spin transfer torques in a large number of systems can be found in *Maekawa* **[27]**.

1.4. Half Metallic Ferromagnets

Half metallic ferromagnets (HMF) are a possible route to highly spin polarised materials. This class of materials was initially proposed by *de Groot et al.* **[28]** in the early 1980s. In conventional ferromagnets, the spin polarisation arises from an imbalance in the density of states for up (majority) and down (minority) spin electrons. In HMFs the conduction properties for the minority channel are completely different to that of the majority spin channel. The majority band has filled electron states up to the Fermi energy giving metallic conduction while the minority states have a band gap resembling a semiconductor. This is shown schematically in Figure 1.5.

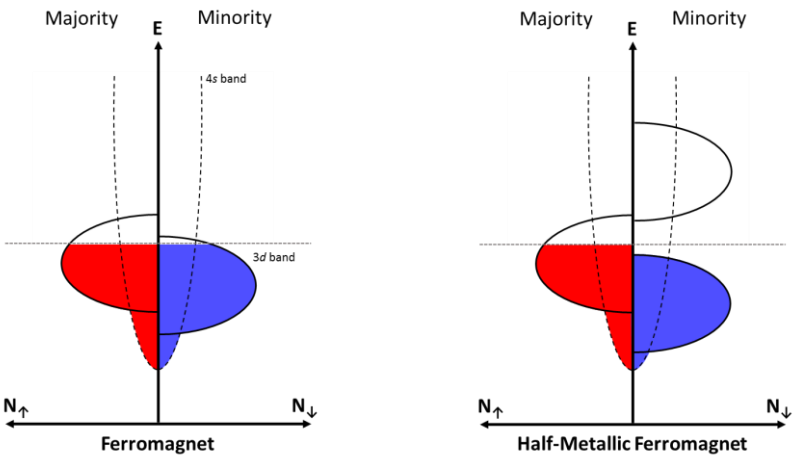

Figure 1.5. Schematic diagrams of the band structures for a ferromagnet and a half-metallic ferromagnet.

Since the original studies of half-metallic ferromagnetism on NiMnSb **[28]** a large number of compounds have been found to be half metallic. Many of these are complex alloys, predominantly Heusler alloys **[29-31]** although half-metallic ferromagnetism has been shown in CrO_2 **[32]** and even predicted in graphene **[33]**. Because of these unusual conduction properties HMFs could potentially provide a material with 100% spin polarisation. This would provide extremely high values of TMR and GMR (TMR 832% **[34]** and GMR of 80% **[19]**) as well as large spin transfer torques for future spintronic devices. A more detailed discussion of the origin of this half metallicity in Co-based Heusler alloys can be found in chapter 3.

1.5. Heusler Alloys in Magnetoresistive Devices

Since the discovery of half metallic ferromagnetism in a number of Heusler alloys they have been a field of great research interest for spintronic devices. Co-based Heusler alloys are of particular interest due to their high magnetic moment and Curie temperature, as well as their predicted 100% spin polarisation. Alloys of $Co_2(Mn_{1-x}Fe_x)Si$ **[35]**, $Co_2Fe(Al_{1-x},Si_x)$**[34]** and Co_2MnGe **[36]** have found application in many different devices. The majority of the work in this thesis will be focused towards $Co_2Fe(Al_{1-x},Si_x)$ alloys so this discussion will be focused primarily on devices using these alloys.

The properties of Heusler alloy devices are extremely dependent upon their structure. This includes the Heusler film itself as well as any effects from those films around it. As such, many different structures and growth methods have been used to optimise these properties. Initially, Co_2FeSi films deposited on V buffered Si substrates resulted in reasonable values of TMR of up to 52% at 16K (28% at room temperature) **[37]**. However this has been improved using Co_2FeSi/Co_2MnSi multi-layered electrodes **[37]**. Improved values from single layer Co_2FeSi electrodes have been achieved using MgO substrates and crystalline MgO tunnel barriers (TMR = 42% at RT) **[38]**. The real improvements to these values have occurred since the optimisation of the alloy composition to $Co_2FeAl_{0.5}Si_{0.5}$.

$Co_2FeAl_{0.5}Si_{0.5}$ is optimised so that the Fermi energy lies in the middle of the minority band gap resulting in much improved spin polarisation (90%) **[39,40]**. Optimisation of both the alloy and the deposition conditions has led to the highest reported value of TMR in a Heusler alloy system, 832% at 9K and 386% at 300K **[34]**.

GMR structures have also been created using $Co_2FeAl_{0.5}Si_{0.5}$ electrodes with both Ag **[41,42]** and Cr **[43]** spacers. Extremely high values of GMR, 80% at 14K (34% at room temperature), have been achieved in these systems **[41]**. Magnetisation switching through spin transfer torque has also been observed in these structures with critical current densities for switching as low as 10^6 A/cm^2 **[42]**. However, all these devices have a number of flaws for commercial applications. The main problems are the high temperatures required to crystallise the Heusler alloy electrodes as well as the UHV deposition conditions. In this work polycrystalline Co_2FeSi films have been characterised as a route to potentially overcoming these problems. Recently, polycrystalline films have been used in device structures resulting in GMR values of up to 10% at room temperature. These films have significant advantages of reduced fabrication temperatures as well as much lower resistance values (30mΩμm^2) **[44]**.

1.6. Notes on Units and Errors

The cgs unit system has been used almost entirely throughout this thesis. There are however a number of instances where the metric international system (SI) units have been used although these are clearly stated. The cgs system is used throughout the magnetic recording industry therefore due to the overlap between the work in this thesis and that industry it was deemed more appropriate.

Where possible, the numerical data in graphs and tables is quoted with its error. These errors have been calculated using standard Gaussian error techniques **[45]** unless otherwise stated in the text. Where values from the literature are quoted without error it is because that error is unknown.

Chapter 2. Magnetism of Heusler Alloy Thin Films

The films studied in this work show a wide range of magnetic properties. It is therefore important to understand the physical principles upon which these properties are based. The magnetisation reversal process in thin films is system dependent. Whether the film reverses through domain wall motion or single domain particle rotation it is important to understand the effects that dominate these processes. Primarily the exchange interactions and anisotropies in the system. The exchange interactions are essential to the magnetism of a material but can also control the reversal processes due to the interaction being inherently short ranged. Heusler alloys in bulk exhibit cubic anisotropy. However, in thin films, the anisotropy is known to be film structure dependent **[46]**. This has a large effect on the magnetic domain structure in the thin films which controls magnetisation reversal.

2.1. Exchange Interactions

2.1.1. Direct Exchange

Direct exchange is the mechanism by which the spins of the electrons associated with neighbouring atoms interact when their quantum mechanical wave functions overlap. The electrons become indistinguishable in this overlapping region and the atoms can 'exchange' electrons **[47]**. The energy associated with this exchange is given by equation 2.1

$$E_{ex} = -2J_{ex}\boldsymbol{S}_i.\boldsymbol{S}_j, \qquad (2.1)$$

where $\boldsymbol{S}_i$ and $\boldsymbol{S}_j$ are the spin angular momentum vectors of two atoms *i* and *j*. J_{ex} is the exchange integral. This describes the direction and strength of the alignment of the spins. The alignment is described by the sign of J_{ex}, where a negative value gives

antiparallel (antiferromagnetic) alignment whilst a positive value gives parallel (ferromagnetic) alignment **[48]**. In metallic systems where the electrons form a band structure the magnetic moment of the material is determined by the energy cost of aligning spins parallel or antiparallel in specific bands near the Fermi energy (E_F). The condition for ferromagnetism is then defined by the Stoner criterion, equation 2.2. **[49]**

$$J_{ex}(E_F)n(E_F) > 1. \qquad (2.2)$$

For ferromagnetism, a large exchange integral $J_{ex}(E_F)$ and density of states $n(E_F)$ at the Fermi energy is favourable. A full explanation of the direct exchange interaction in transition metals and alloys can be found in the comprehensive texts by *O'Handley* **[49]** and *Morrish* **[50]**.

J_{ex} itself is dependent upon the separation of atoms in the material or, more importantly, the separation of the *d* orbitals of the localised electrons. The variation in J_{ex} with atomic separation (r_a) is often shown using the Bethe-Slater curve.

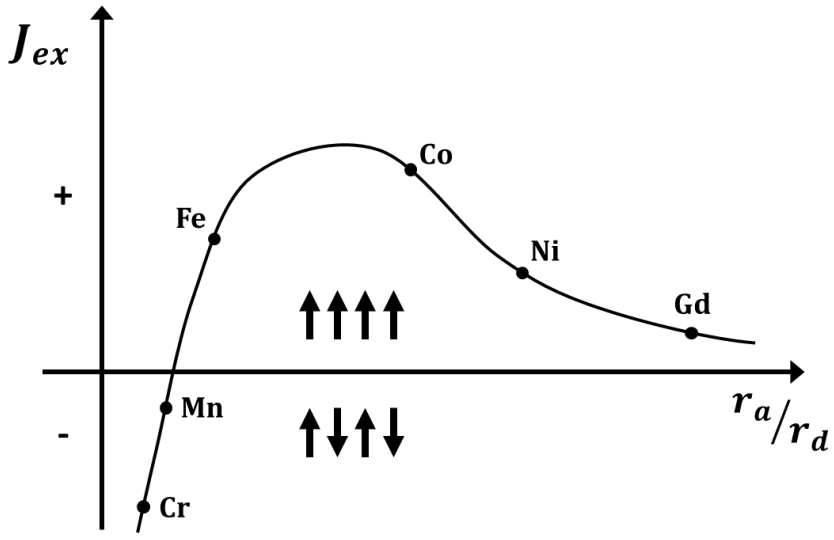

Figure 2.1 Dependence of the exchange integral J_{ex} on the atomic separation r_a normalised to the electron radius in the *d* orbital r_d **[47].**

Figure 2.1 shows that for large atomic separations J_{ex} is positive, resulting in parallel (ferromagnetic) alignment of spins to the limit at which the spacing is so great that the electrostatic interaction and as a result the exchange interaction vanishes. As r_a decreases the exchange integral reaches a peak where the most ferromagnetic elements Fe, Co, and Ni reside. At even smaller spacing the exchange integral becomes

negative and antiferromagnetic order dominates. At extremely small spacing the electrons can be regarded as having the same spatial co-ordinates. Here the Pauli exclusion principle dominates forcing the spins to align antiparallel. At larger spacing the electrons inhabit separate spatial co-ordinates but exhibit the same wave function resulting in favourable parallel alignment **[49]**. This model correctly predicts the magnetic properties for elements. However for alloyed systems such as Co-based Heusler alloys this model must be extended to consider the hybridisation of orbitals between different elements and how this affects the number of electrons that contribute to the magnetic properties. Discussion of this extended model and its relevance to Co-based Heusler alloys can be found in section 3.1.3.

2.1.2. Indirect Exchange

Indirect exchange coupling occurs when localised but separated magnetic moments in metallic systems are coupled by conduction electrons. It was proposed and developed by *Ruderman and Kittel* **[51]**, *Kasuya* **[52]** and *Yosida* **[53]** to explain the coupling of nuclear spins to *s*-electrons. This type of exchange interaction is often known as the RKKY interaction.

This model has subsequently been used to describe the magnetic moments of rare earth metals **[54]** as well as intergranular exchange coupling and the coupling between magnetic layers separated by non-magnetic spacers **[55]**. When a localised magnetic impurity is placed in a typical electron gas, that is a system of electrons free from their ions which are treated as a non-interacting gas **[56]**, the wave functions change to accommodate the impurity. This effectively adds more possible states for the conduction electrons when their spins are aligned with that of the magnetic impurity. This also forms a series of charge oscillations. These oscillations are all in phase at the impurity but as the electrons have different energies and therefore wavelengths, these charge oscillations interfere at some distance from the impurity **[49]**. These electrons all contain information about the initial spin state of the magnetic impurity so these oscillations in charge are also oscillations in the spin density. Therefore if a second localised magnetic moment is placed within the range of these oscillations it will become coupled either ferromagnetically or antiferromagnetically to the initial atom depending upon the spin density at its position in the system **[57]**.

The dependence on the position of the coupled atoms makes this exchange extremely susceptible to any change in the distance between local moments. This was shown experimentally by *Parkin et al.* in a series of experiments using different transition metal spacer layers of varying thickness to separate two ferromagnetic layers **[11,55,58]**. Figure 2.2 shows clearly the oscillatory nature of the coupling of two ferromagnetic layers on their separation. The strength and nature of the exchange coupling is represented by the magnitude of the applied field at which the sample saturates. Antiferromagnetic coupling requires a large field to saturate while ferromagnetic coupling requires a lower saturating field.

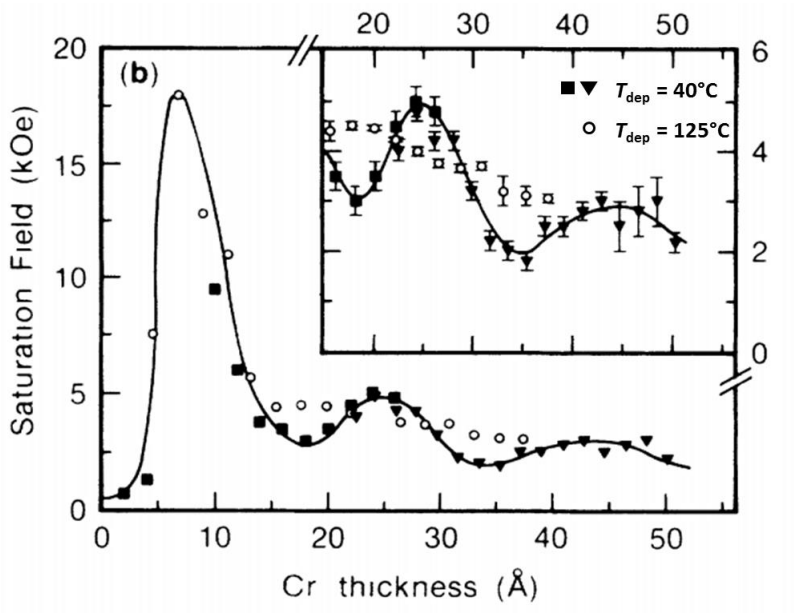

Figure 2.2. The dependence of indirect exchange coupling on the thickness of a Cr interlayer separating two ferromagnetic layers. The symbols represent three different films of the same structure. **[55]**.

The other point to note about Figure 2.2 is the range over which the interaction can take place. The coupling extends to a range of about 4 nm . This means that the coupling can occur across grain boundaries making the RKKY interaction particularly important in granular thin films. Individual grains can become exchange coupled and reverse their magnetisation as if they were a single entity. This process is well documented in thin film granular media **[59]**. This makes intergranular exchange an important consideration when studying the polycrystalline Heusler alloy films in this work.

2.2. Magnetic Anisotropies

2.2.1. Magnetocrystalline Anisotropy

Anisotropy is the term used to describe the directional dependence of the properties of a system. Magnetocrystalline anisotropy is the dependence of the ease of magnetisation of a magnetic medium relative to the orientation of specific lattice planes of the crystal. This results from the coupling of the local spin magnetic moments to the shape and orientation of the electronic orbitals of the atoms in a crystal. It is also controlled by the symmetry of the crystal field, or the electric field created by the chemical bonding of atoms within the lattice **[49]**. This quenches the direction of the orbitals along the crystal bonds. The electron spins align along these orbitals, promoting a single or several preferential axes of spin alignment.

The result of this is one, or a set of, crystallographic directions (easy axes) along which it is easier for magnetisation to align than other directions. The axis that is hardest to magnetise is known as the hard axis. The crystallographic directions away from the easy axes are harder to magnetise as aligning the spins requires the breaking of the spin-orbit interaction. This requires energy expenditure from the external field. When saturation is achieved along an axis other than an easy axis the energy required to achieve this is stored in the crystal as the magnetocrystalline anisotropy energy, E_K. For the Heusler alloys studied in this thesis, the majority of the spin (localised) contribution to the magnetisation comes from the Co atoms. These exhibit octahedral symmetry, resulting in cubic-like magnetocrystalline anisotropy. The anisotropy energy is given by equation 2.3:

$$E_K = K_0 + K_1(\alpha_1\alpha_2 + \alpha_2\alpha_3 + \alpha_3\alpha_1) + K_2(\alpha_1\alpha_2\alpha_3) + \ldots \quad (2.3)$$

Where K_0, K_1 and K_2 are the anisotropy constants for a given material and α_1, α_2 and α_3 are the cosines of the angles made between the saturation direction and the [100], [010], and [001] crystal axes respectively **[47]**. For a material with uniaxial anisotropy, for example *hcp* Co where the easy axis lies along the c-axis, E_K is given by **[47]**:

$$E_K = K_0 + K_1 \sin^2\theta + K_2 \sin^4\theta + \ldots \quad (2.4)$$

where θ is the angle between the easy axis and the magnetisation of the system. What is evident from both equations is that the K_0 term is independent of the angle, has no

influence on the easy axis of magnetisation and therefore can be ignored. K_1 is the term of most importance as it is generally much larger than K_2, thus we can generally ignore K_2. The sign of K_1 and K_2 can however be important, for positive K_1 the easy axis most likely lies along a cube edge (e.g. [100]). For materials with negative K_1 (such as Ni) the easy direction lies along the body diagonal (e.g. [111]) **[57]**.

For Heusler alloy thin films the anisotropy constants are found to be greatly system dependent, being affected by deposition technique as well as the substrate onto which the film is deposited **[46,60]**. For single crystal films of Co_2FeSi similar to those characterised in this work the values of K_1 have been measured in the range 1.8 to 4 x10^4 ergs/cm^3 **[46]**. The nature of the magnetocrystalline anisotropy itself is also discussed and is found again to be heavily system dependent. Due to the $L2_1$ structure being cubic it is expected that the magnetocrystalline anisotropy would be three-fold cubic (see section 3.1.1 for details). However in experiments it is found that in the single crystal films there is often an overlaid uniaxial anisotropy **[46,61-63]**. The origin of this is not entirely understood. It has been hypothesised that this effective uniaxial anisotropy arises from the substrate/film bonding **[62]** as previously reported for Fe/GaAs **[64]**.

2.2.2. Shape Anisotropy

In the polycrystalline films the dominant anisotropy is unlikely to be magnetocrystalline. Shape anisotropy is more likely to be dominant. This arises from the effect of the demagnetising field, H_d, if a magnetic grain is not spherical. If a grain is elongated in any way then H_d along the short axis will be greater than H_d along the long axis. A full description of the effect of shape on H_d and how this affects magnetic anisotropy can be found in *Cullity* **[47]**. In essence, the quantitative treatment uses the magnetostatic energy of the grain, E_{ms}, and how this changes with the direction of an applied field relative to the magnetisation, M, equation 2.5.

$$E_{ms} = \frac{1}{2} N_d M^2. \qquad (2.5)$$

N_d is the shape demagnetising factor which expresses how the demagnetising field changes with grain shape, $H_d = -N_d M$. The example case that will be most applicable to the specimens in a film is a prolate spheroid. This is shown in Figure 2.3 with a major axis c and a minor axis a magnetised to M at an angle θ to the major axis.

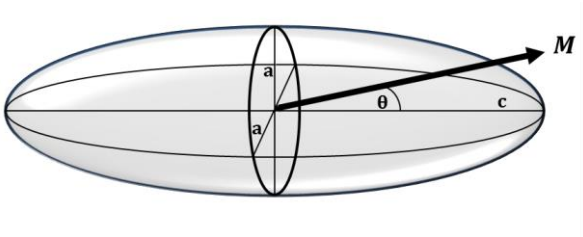

Figure 2.3. Magnetised prolate spheroid.

The condition depicted in Figure 2.3 is considered in terms of equation 2.5 when the axis dependent shape demagnetising factors N_c and N_a for E_{ms} are defined. The term for the second factor is angle dependent and takes exactly the same form as that for K_1 in the uniaxial case (equation 2.4). It is possible to express the shape anisotropy constant K_s as

$$K_s = \frac{1}{2}(N_a - N_c)M^2. \qquad (2.6)$$

Equation 2.6 shows that the magnitude of the shape anisotropy is a function of both the axial ratio c/a as well as the magnetisation of a sample. For Co_2FeSi at saturation, M_s = 1140 emu/cm^3. The variation in the shape anisotropy with the axial ratio of a prolate spheroid has been calculated using the shape demagnetising factors from reference **[65]** and the value of M_s above.

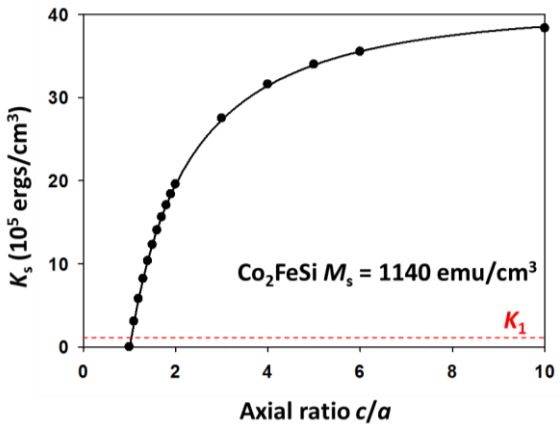

Figure 2.4. Variation of the shape anisotropy constant as a function of axial ratio for a prolate spheroid of Co_2FeSi. The magnetocrystalline anisotropy K_1 is shown by the red line.

It is shown in Figure 2.4 that this effect is quite significant. For single crystal Co_2FeSi the value of K_1 is quoted as having a maximum of 4x10^4 ergs/cm^3 **[46]**, which is achieved through the shape anisotropy with an axial ratio of just 1.1. That is to say that a prolate spheroid of Co_2FeSi with no magnetocrystalline anisotropy and an axial

ratio of 1.1 has the same uniaxial anisotropy as a spherical particle of Co_2FeSi with the measured uniaxial anisotropy as reported in reference **[46]**. More important in the context of the polycrystalline films measured in this work is that a Co_2FeSi grain with an axial ratio of just 1.5 has shape anisotropy 4 times larger than the magnetocrystalline anisotropy. This means that any elongation of Co_2FeSi grains means that shape anisotropy become the dominant term in the magnetisation reversal process.

2.3. Magnetic Domains and Single Domain Particles

2.3.1. Domain Formation

Initially proposed by *Weiss* in 1906 domain theory is now central to understanding the magnetisation processes in magnetic materials. Domains form to reduce the magnetostatic energy of a magnetic material, the energy stored in the field which attempts to demagnetise the sample. This process is shown schematically in Figure 2.5 for a material with strong uniaxial anisotropy (e.g. Co) **[66]**.

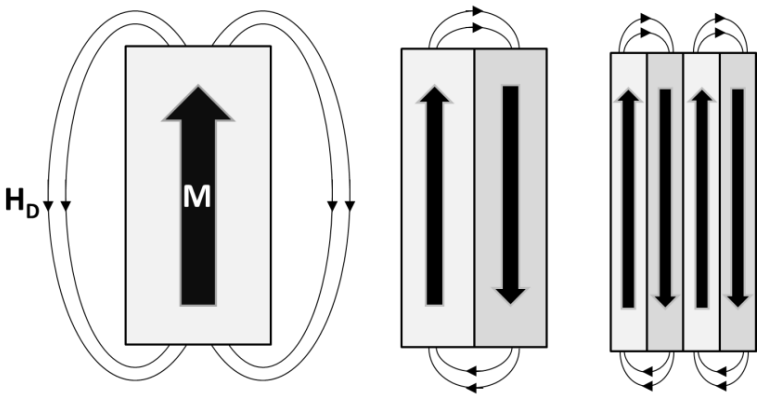

Figure 2.5. Domain structure in a uniaxial single crystal **[66]**.

The schematic shows that when a magnetic material is saturated in one direction an opposing field is created, this is the demagnetising field H_D which stores the magnetostatic energy E_{ms} (equation 2.5). The magnetostatic energy is dependent primarily on the magnitude of the magnetisation of the sample. To reduce this magnetisation, and therefore E_{ms}, a magnetic material breaks into domains **[66]**. Each domain contains magnetic moments aligned parallel to each other. Their magnetic moments preferentially lie along the easy axes of the material. In the uniaxial material in Figure 2.5, the domains form with magnetisation aligned anti-parallel along the easy axis, reducing the demagnetising field and E_{ms}. It is also possible for the material

to break into more than two domains to further reduce H_D. In systems with cubic anisotropy (like Heusler alloys) the domain structure is often more complex.

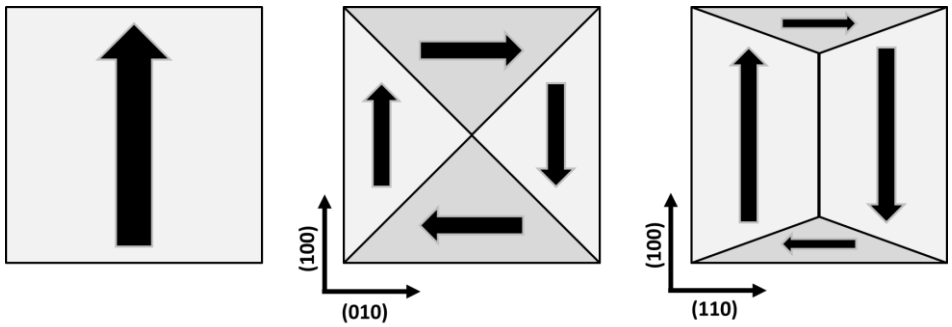

Figure 2.6. Domain structures in cubic materials **[47]**.

In materials with cubic anisotropy it is possible to have more than one easy axis. This results in domains that can have their magnetisation aligned at 90° to one another and not just 180°. In Figure 2.6 we see the typical domain structure for a material where the anisotropy is cubic with an easy axis along the cube edge, [100], and intermediate axis along the face diagonal, [110]. If the crystal is cut so that a face is formed with [100] and [010] edges all the domains are equal and align at 90° to one another in a 'flux closure' configuration. This means that the magnetostatic energy is reduced to zero as there is no stray field. For the situation where the crystal is cut with a face with edges of [100] and [110] the domains along the easy axis become elongated relative to those at 90°. As a result a system is formed where a domain can have adjacent domains aligned simultaneously at 90° or 180°. This is important for single crystal Heusler alloy films as the induced small uniaxial anisotropy can result in a similar domain formation **[67]**.

2.3.2. Domain Walls

The interface between neighbouring domains is not abrupt. The change in direction of moments occurs over some finite length, typically tens of nm. The magnetisation reverses through a series of slight rotations of the localised moments in the boundary region. These boundary regions are known as domain walls. There are two types of domain walls, Bloch walls and Néel walls, named after their respective discoverers. The difference between the two types of wall comes down to the way in which the magnetic moments rotate through the wall **[57]**.

As shown in Figure 2.7, Bloch walls change the direction of the magnetisation through confinement of the rotation of magnetic moments to the plane parallel to the domain wall. Bloch walls occur when the magnetic moments rotate perpendicular to the plane of the domain wall. Bloch walls occur in bulk samples. However, in thin films they create free poles at the sample surface which contribute significant magnetostatic energy to the system. To reduce this energy, Néel walls form which rotate in the plane so that free poles don't appear at the film surface **[47]**.

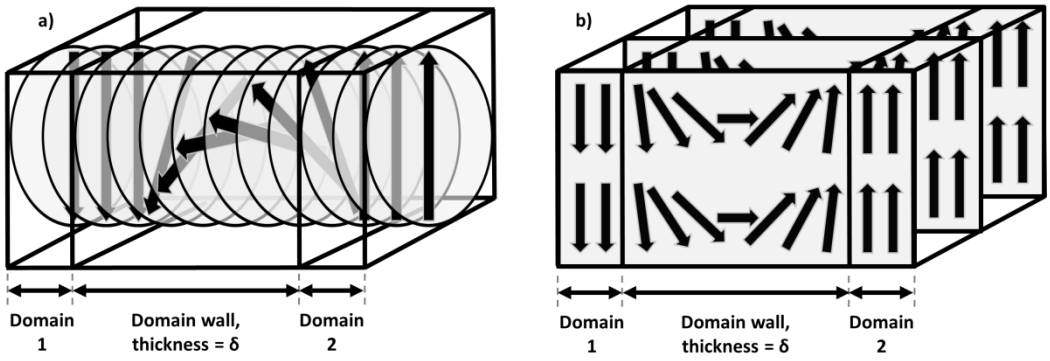

Figure 2.7. Schematic diagrams of 180° a) Bloch and b) Néel domain walls.

Domain walls have a finite width, δ. The width of the domain wall results from a balance of the anisotropy energy E_K and exchange energy E_{ex} in a magnetic material.

$$E_K = f(\phi) \tag{2.7}$$

where f is the function describing the anisotropy of the system, as per equations 2.3 and 2.4. ϕ is the angle that the magnetisation vector at a specific point in the wall makes with the easy axis of the system.

$$E_{ex} = A_{ex}\left(\frac{d\phi}{dx}\right)^2 \tag{2.8}$$

where A_{ex} is the exchange stiffness constant and x is the position of the moment within the wall. A_{ex} is a function of the exchange integral, the magnitude of the spin moment and the number of spins per unit area of wall. The domain wall energy is the sum equations 2.7 and 2.8, which when minimised, can give an expression for the effective domain wall width, equation 2.9 **[66]**.

$$\delta = \pi\sqrt{\frac{A_{ex}}{K}} \tag{2.9}$$

The width of the domain wall is thus controlled by the lowest energy state which is a function of both the exchange coupling between spins in the wall and the anisotropy constant of the system, whether that is cubic or uniaxial.

2.3.3. Formation of Single Domain Particles

If a magnetic material is not a single crystal and is instead made of fine particles or grains then it is possible that some of these grains will only contain a single domain. The phenomenological interpretation would suggest that if the width of the domain wall is greater than the size of the grain then it is impossible to fit two domains and the wall in the particle. More accurately this should be considered in terms of the various energy contributions and how the energy in the grain would be minimised. The magnetostatic energy will vary with the volume, D^3, of the grain as $E_{ms} \propto M^2$. The domain wall energy will vary as a function of the grain cross section, D^2 **[47]**. Therefore, at some point, there is a diameter of grain at which it becomes energetically favourable for the grain to be in a single domain state. If a spherical particle is taken as an example, then the critical radius, r_c, at which the single domain state becomes favourable is given by **[49]**:

$$r_c \approx 9\frac{(A_{ex}K)^{1/2}}{\mu_0 M_s^2} \tag{2.10}$$

Equation 2.10 is an approximation and only holds in the limit of large values of K. *O'Handley* **[49]** gives an extensive discussion of the effect of grain parameters on the critical radius for single domain particle behaviour. This single domain behaviour and the limiting cases are extremely important for the evaluation of the polycrystalline films studied in this work. In polycrystalline films the grain size is distributed. As such it is possible for there to be both single and polydomain particles in the film. This can have a large effect on the magnetisation reversal mechanism in these films.

2.4. Magnetisation Reversal Processes

2.4.1. Domain Wall Motion

When an external field is applied to a magnetic material the domains aligned with the field will grow. If the material is initially saturated, a field applied opposite to this saturation direction will nucleate a domain with its magnetisation aligned with the field. This nucleation occurs through the rotation of a small number of moments in the film. Magnetisation reversal through rotation will be discussed in section 2.4.3. If a

sufficiently large field is applied, the material will saturate in the direction of the applied field. The growth of domains requires the motion of the domain walls. This motion is not smooth and the domain walls move through a series of jerky steps known as *Barkhausen* jumps **[47]**. These jumps are the result of continuous pinning and de-pinning of the domain wall as it moves through the material. The domain wall must move through an energy landscape with a series of peaks and troughs. The peaks in this landscape are pinning sites where the domain wall requires extra energy to overcome this pinning energy, usually in the form of an applied field. This is shown schematically in Figure 2.8. The figure does not display a full hysteresis loop but rather the effect of activating two *Barkhausen* jumps, one in each of the positive and negative field directions.

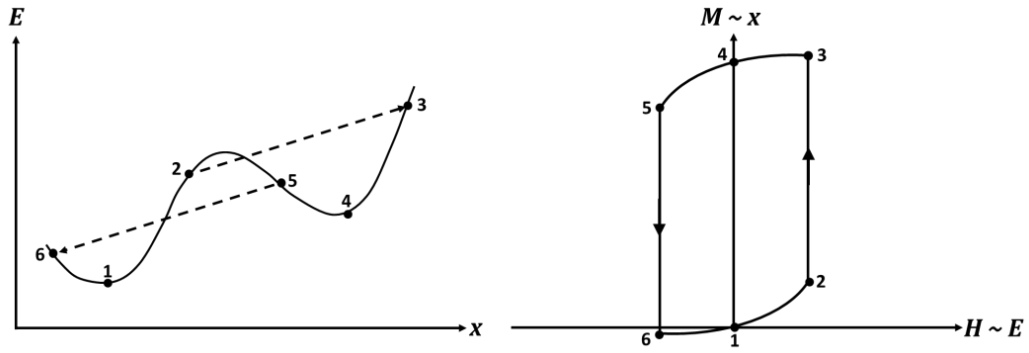

Figure 2.8. Domain wall energy landscape and its effect on magnetic hysteresis, adapted from **[47]**.

Figure 2.8 also highlights the possibility of both reversible and irreversible domain wall motion. If a field is applied to the sample the domain wall will move from position 1 to position 2. If at this point the field is removed the domain wall would move back down the energy landscape and return to position 1. However, if a slightly larger field is applied then the domain wall will make a *Barkhausen* jump to position 3. This jump is irreversible, if the field is removed the domain will return to position 4 and not position 1. What is more important than the mechanism of domain wall motion in relation to this work is the causes of the pinning sites in the films.

However, the distribution of energy barriers is extremely important for understanding magnetisation reversal in thin films. This distribution of energy barriers is known as the switching field distribution (SFD). By analysing the SFD it is possible to infer a large amount of information about the magnetisation processes in the film. The switching field distribution can be accessed by measurement of the

irreversible susceptibility χ_{irr}. This is found from the differential of the DC Demagnetised (DCD) remanence curve which will be discussed in greater detail in chapter 5. The irreversible susceptibility is a measurement of purely the irreversible components of the reversal process, such as *Barkhausen* jumps or in granular films the rotation of magnetisation through the grain.

2.4.2. Hindrances to Domain Wall Motion

The motion of a domain wall requires an energy input, therefore any regions of the film that increase this energy cost act as domain wall pins. Possible causes of these energy increases include inclusions, surface roughness and microstresses within the material. A comprehensive discussion of the many possible hindrances to domain wall motion can be found in *Cullity* **[47]**. Here there is only an overview of those hindrances relevant to this work.

Inclusions are areas of the film that have a different magnetisation than the surrounding material. Essentially, inclusions moderate the exchange interaction between moments in the wall, increasing the energy. These inclusions can take many forms. Different phases of an alloy or impurities in the magnetic material are most relevant to the work in this thesis. Vacancies in the lattice can also act as inclusions. As Heusler alloys can exhibit many different disordered phases, the effect of these different phases of the alloy on the magnetic properties is extremely important. However, as well as hindering domain wall motion, these disordered phases can also aid domain wall motion. This is due to reduced magnetocrystalline anisotropy when compared to that of the perfect $L2_1$ Heusler structure. A number of the films in this work are multilayers. Interatomic diffusion between the layers can lead to a build-up of impurities in the magnetic layers, which can also act as hindrances to domain wall motion.

Surface roughness can lead to significant domain wall pinning. A domain wall will always try to reduce its own energy. Surface roughness allows this through reduction of the domain wall area in the thinner regions of the film. Therefore the domain walls will always pin in the valleys of the film. The final hindrance to domain wall motion that is considered here is the effect of microstress. Microstresses arise from the deformation of lattice planes within the material. This can have a number of origins although the most common of these are the effects of defects and dislocations. Microstress hinders domain wall motion as it alters the local anisotropy field through

a stress anisotropy. This extra anisotropy increases the energy the domain wall has to overcome to move beyond that point, thus pinning the wall. In epitaxially sputtered films these microstresses are of particular importance as the lattice match between most Co-Based Heusler alloys and substrates is not perfect. As a result, misfit dislocations form at these interfaces to relieve the stress as much as possible. This does not completely remove the stresses and these dislocations will still deform the local lattice planes. This can contribute a significant localised stress anisotropy to the film.

2.4.3. Magnetisation Rotation

It is also possible to change the magnetisation of a magnetic material by rotation of the moments through the material. This happens to a small extent in domain wall controlled systems but is most commonly examined in terms of single domain particles. For domain wall systems this is usually the highest energy part of the hysteresis loop which occurs when the bulk of the film has already reversed its magnetisation. The single domain particle case was originally examined in the seminal paper by *Stoner* and *Wohlfarth* **[65]**. As with the shape anisotropy case it is most easily considered for the case of a prolate spheroid as shown in Figure 2.9.

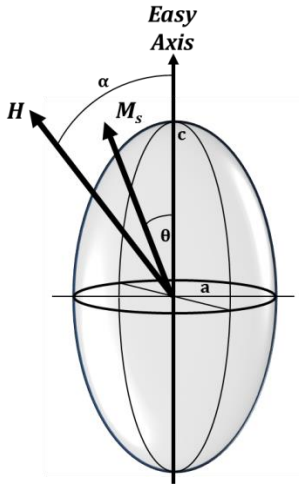

Figure 2.9. Schematic of the Stoner-Wohlfarth problem for an elongated single domain particle.

The simplest case for this situation is the one where the magnetisation and applied field both lie parallel to the easy axis of the particle, equation 2.11. In this situation the energy required to rotate the magnetisation through the particle, ΔE (energy barrier to reversal), is simply a product of the particle volume, V, and its anisotropy, K.

$$\Delta E = KV \tag{2.11}$$

The result of this is that the energy of the applied field needed to saturate the particle is exactly equal to the anisotropy energy. This energy is often expressed in terms of an anisotropy field H_K at T = 0 K.

If the applied field is not aligned with the magnetisation then the energy barrier to reversal is reduced. This reduction is proportional to the angle between the easy axis and M. Therefore, the energy required to reverse the magnetisation in the non-aligned case is a sum of the reduced energy barrier and the energy from the applied field, equation 2.12.

$$E = KV \sin^2 \theta + (-HM_sV \cos(\theta - \alpha)) \tag{2.12}$$

The effect of an applied field angle on the hysteresis of the particle can be seen in Figure 2.10. The figure shows that for the aligned case the hysteresis loop is square with the magnetisation reversal taking place at H_K. As the applied field angle increases both the remanent moment and the coercivity decrease.

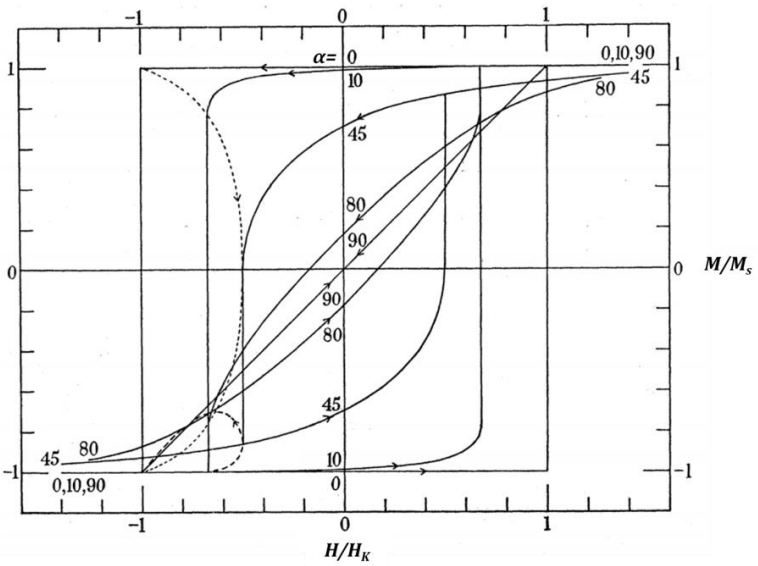

Figure 2.10. Hysteresis loops for prolate spheroids with a field applied at an angle α to the easy axis **[65]**.

This type of single particle behaviour is important for a number of films in this work. However it must be noted that the results of Figure 2.10 only hold at T = 0 K. This result does however give an excellent basic understanding of the magnetic properties of single domain particle systems. Importantly, the decrease of both M_r and

H_c when the particle is misaligned with the field is demonstrated. This is likely to be the case for the polycrystalline films in this work, where due to the sputtering process parameters α is likely to be distributed, as are both V and K.

The Stoner-Wohlfarth model makes a number of assumptions that are not true for many real systems, primarily that the spins in the material all remain parallel (coherent) whilst rotating. This is not always the case, a number of different models have been proposed for systems that do not show Stoner-Wohlfarth behaviour. The two most often observed incoherent modes of rotation are spin fanning and curling. Spin fanning occurs when an elongated particle essentially breaks into smaller magnetic entities which reverse out of phase with one another, often called the chain of spheres model. In the spin curling model the spins 'curl' through the particle always remaining perpendicular to the radius. As a result, the spins are no longer coherent with one another. Both these mechanisms are most commonly seen in extremely elongated particles. As a result, it is unlikely that these two reversal mechanism will be observed in this work. A full description of both processes can be found in the standard text **[47]**.

2.5. Magnetic Activation Volumes

2.5.1. Magnetic Viscosity

The Stoner-Wohlfarth model only applies at T=0 K. Above this temperature thermal energy excites fluctuations in the magnetisation of a sample. These fluctuations can have amplitude sufficient to reverse regions of a thin film. The characteristic time (τ) that it takes for a magnetic system to lose 37% of its magnetisation due to thermal activation is described by equation 2.13, an Arrehnius law formalised by *Néel* **[68]**.

$$\tau^{-1} = f_0 exp - \left(\frac{KV(1 - H/H_K)^2}{k_B T}\right) \qquad (2.13)$$

f_o is the attempt frequency which is often given the value 10^9 Hz **[69]**. In real thin films the volume of grains is distributed. This leads to a distribution of the energy barriers to reversal. It was found that when the distribution is wide the decay of magnetisation follows a ln(t) law **[70]**:

$$M(t) = M(t_0) \pm Sln(t/t_0) \qquad (2.14)$$

where S is the coefficient of magnetic viscosity. The sign of the second term is dependent upon whether the magnetisation is deemed to be positive or negative in the initial state. Equation 2.14 is however the 1st order approximation to a series expansion in $\ln(t)$ which can describe the magnetisation decay in any system. Equation 2.14 is sufficient to describe a system with a wide energy barrier distribution ΔE, whose magnetisation varies linearly in $\ln(t)$ such as those found in this work. In systems with distributed energy barriers, S must also be distributed as it is intrinsically linked as shown by *Gaunt* through equation 2.15 **[71]**.

$$S(H) = 2M_s k_B T f\big(\Delta E(H)\big) \tag{2.15}$$

where $\Delta E(H)$ describes the energy barrier distribution being activated at a specific applied field. $S(H)$ goes through a maximum at H_c. The coefficients of magnetic viscosity at different field values can be determined experimentally by measuring a series of magnetic time dependence curves through the method described fully in section 5.1.3.

2.5.2. The Fluctuation Field and the Activation Volume

The idea of the fluctuation field (H_f) was initially proposed by *Néel* in 1951 **[72]**. H_f is a fictitious field which is used to couple the effect of thermal energy to a magnetic system. This extended the ideas of *Street* **[70]** . The fluctuation field, equation 2.16, was considered in more detail by *Wohlfarth* **[73]** to understand the observed time dependence of magnetisation. The constant of proportionality originally used by *Néel* was found to have the dimensions of magnetic moment given by $M_s V_{act}$, where V_{act} is known as the activation volume of reversal.

$$H_f = \frac{k_B T}{V_{act} M_s} \tag{2.16}$$

For the work in this thesis it is more useful to write this equation in terms of the activation volume as this is often the parameter to be found. Thus the parameters to be measured are the fluctuation field and saturation magnetisation at the measurement temperature. H_f may be determined experimentally through measurement of the magnetic viscosity coefficients, as well as the irreversible susceptibility $\chi_{irr}(H)$ via equation 2.17 as initially proposed by *Street et al.* **[74]**. $\chi_{irr}(H)$

can be determined from the differential of a DCD remanence curve as described in section 5.1.3.

$$H_f(H) = \frac{S(H)}{\chi_{irr}(H)} \tag{2.17}$$

This determination of the fluctuation field is limited to systems where the energy barrier distribution is sufficiently wide as to allow linear decay of *M* with ln(*t)*. For systems with a narrow energy barrier distribution another formulation of H_f was proposed by *El-Hilo et al.* equation 2.18 **[75]**. This uses the difference in time for achieving the same value of *M* at different applied fields.

$$H_f = \frac{\Delta H}{\ln(t_1/t_2)}\Big|_M \tag{2.18}$$

A full description of the derivation of this form of H_f can be found in reference **[75]** but this will not be reproduced here as the films in this work can all be analysed using the linear case, equation 2.17 due to them having a sufficiently wide distribution of energy barriers.

2.5.3. The Activation Volume in Heusler Alloy Thin Films

As the fluctuation field is a fictitious field the activation volume in not a real volume in the film. It can however give a lot of information about the magnetisation reversal processes in a thin film. It has been used widely in magnetic recording media to understand the size of bits **[76]**, where a number of grains may reverse their magnetisation co-operatively. By applying this technique to Heusler alloy films it is possible to understand how the reversal mechanisms may affect possible spintronic devices.

In granular polycrystalline films, the activation volume may be representative of the magnetisation reversal of a single magnetic grain, multiple magnetic grains or in certain cases a fraction of a single magnetic grain **[77]**. In single crystal or epitaxial films that reverse via domain wall motion the activation volume is analogous to the volume swept out by a single *Barkhausen* jump. The size of these reversal events is of particular importance to nanoscale spintronic devices, such as a magnetoresistive nanopillar. It is important to understand what fraction of a magnetic nanopillar will reverse coherently during operation as this can have a large effect on the signal from the device, especially at high frequency.

Chapter 3. Co-Based Heusler Alloys

Heusler alloys are an unusual class of materials which number over 3000 compounds and can comprise of almost every element in the periodic table. These compounds can have a wide range of properties from being half-metals **[29]**, semiconductors **[78]** superconductors **[79]**, topological insulators **[80]** and many more besides. These remarkable compounds were initially discovered by Fritz Heusler in 1903 whilst studying the ferromagnetism of an alloy with composition Cu_2MnAl **[81]**. Heusler alloys are generally ternary compounds although a number of quaternary compounds such as $Co_2Fe(Al,Si)$ **[19,82]** and $Co_2(Cr,Fe)Al$ **[83]** are being studied for spintronic applications. These compounds are usually split into two groups, those with 1:1:1 (Half-Heusler) stoichiometry and those with 2:1:1 (Full-Heusler) stoichiometry. Co-based full-Heusler alloys are of particular interest for spintronic applications as they can exhibit half metallic properties above room temperature. These materials also have high Curie temperatures as well as good lattice matches with widely used III-V semiconductors and MgO substrates **[84]**.

3.1. The Heusler Structure and the Origins of Magnetism

3.1.1. Crystal Structure and Disordered Phases

Full Heusler alloys with 2:1:1 stoichiometry, often referred to as X_2YZ, crystallise in the cubic $L2_1$ structure, where the X and Y are transition metals and the Z is a main group element. This structure is formed of four interpenetrating fcc sublattices. Two sublattices are equally occupied by the X element of the compound and the other two are occupied by the Y and Z elements. The result of this is a rocksalt type structure formed from the Y and Z elements filling the octahedral positions of the lattice, whilst the atoms of the X element fill the vacant tetrahedral positions. The structure has also

been described in terms of a zinc-blende type structure or a superlattice of the CsCl-like structure **[84]**. The $L2_1$ structure is shown in Figure 3.1.

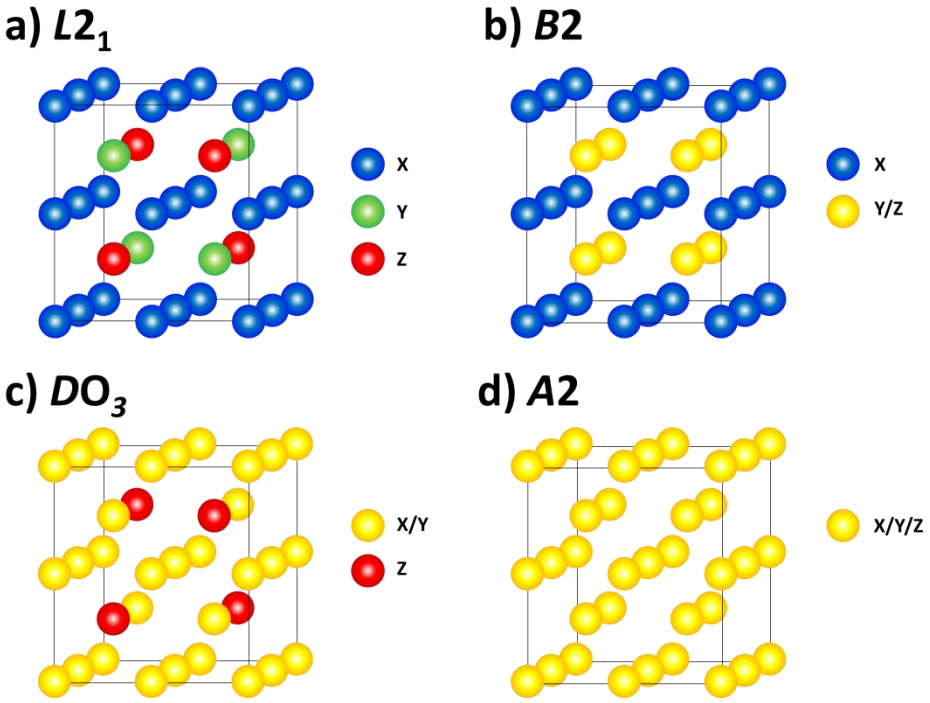

Figure 3.1. Types of order and disorder occurring in Heusler structures, a) $L2_1$ b) $B2$ c) DO_3 and d) $A2$.

The magnetic and half-metallic properties of Heusler alloys are strongly dependent on the atomic ordering. It is therefore always important, if not essential, to characterise the crystal structure of the material. There are a number of common disordered phases which vary from the $L2_1$ Heusler structure. The effect of these disordered phases will be discussed in more detail later in this chapter. If the Y and Z sites become interstitially disordered the $B2$ structure is formed as shown in Figure 3.1. Disorder between the X and Y sites can also occur which forms the DO_3 structure. This structure can however be the highest ordered phase of certain intermetallic alloys with Heusler like structure (X = Y) such as Fe_3Si **[85]**. Disorder can also occur among all atom sites resulting in the totally disordered $A2$ structure.

3.1.2. The Origin of Half Metallicity

The origin of half-metallicity in full-Heusler alloys was initially described by *Galanakis et al.* **[86]** for the compound Co_2MnGe. In the *Galanakis* interpretation the lattice is initially treated as just the Co_2 positions so the hybridisation of *d*-orbitals for the minority states in Co-Co interactions are calculated first. These are shown in Figure

3.2a. In the figure, $d1$ to $d5$ correspond to the $d_{xy}, d_{yz}, d_{zx}, d_{3z^2}$ and the $d_{x^2-y^2}$ orbitals, respectively. The differences between these orbitals are also shown in Figure 3.2a. Between two neighbouring Co atoms in the lattice two hybridised orbitals form from the $d4$ and $d5$ orbitals, forming a low energy bonding e_g orbital and a high energy e_u antibonding orbital. The $d1$, $d2$ and $d3$ orbitals hybridise to form a triply degenerate low energy bonding t_{2g} orbital and a triply degenerate high energy antibonding t_{1u} orbital. Where t_{1u}, t_{2g}, e_g and e_u are the chemical nomenclature describing the shape (angular momentum) of the hybrid orbital.

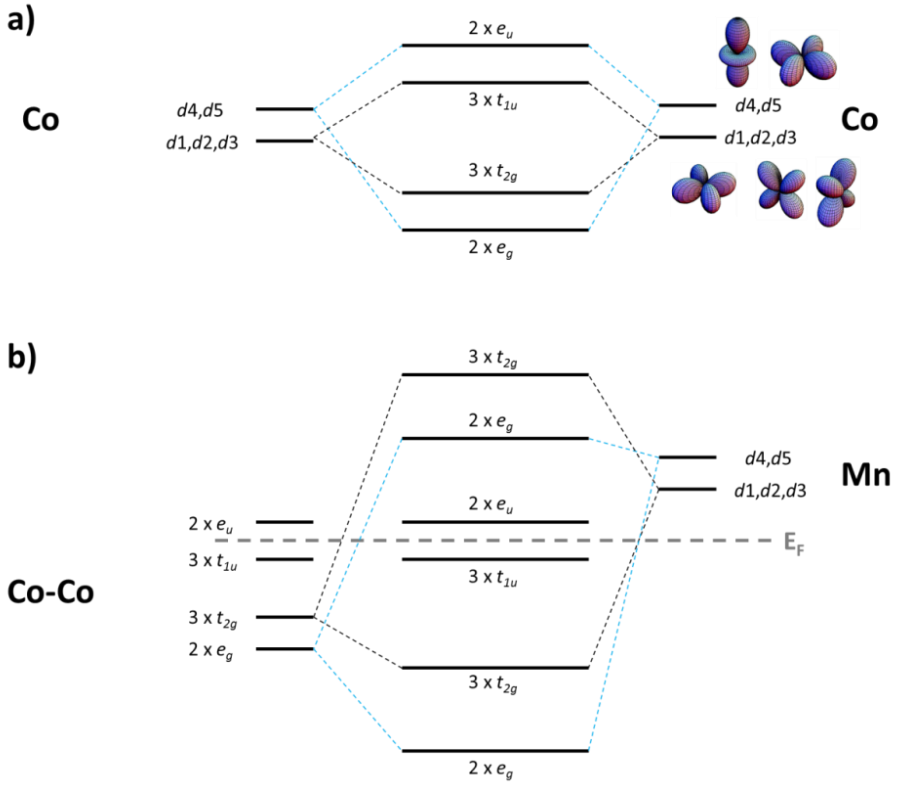

Figure 3.2. Possible hybridisation between d orbitals for minority states for the compound Co_2MnGe by considering a) the Co-Co interaction and b) the Mn-(Co-Co) interaction **[86]**. The shapes of the different d orbitals are also shown in a).

The contribution from the Mn atoms in the lattice must also be considered as well as the Co-Co interaction. The d-orbitals from the Mn atoms hybridise in a similar way to that seen for Co-Co. Figure 3.2b shows that the $d4$ and $d5$ orbitals hybridise with the double degenerate e_g orbital of the Co-Co to form two e_g orbitals, one low energy bonded and one high energy antibonded orbital. The $d1$, $d2$, and $d3$ orbitals also hybridise with the triple degenerate t_{2g} orbital from the Co-Co to form 6 more t_{2g} orbitals, three of which are bonding and sit below the Fermi energy and another three

which are antibonding and are higher energy. This interaction with the Mn leaves 5 hybridised orbitals from the Co-Co interaction free. The three t_{1u} orbitals sit just below E_F while the two e_u orbitals sit just above E_F. The result of this is a gap in the band structure at E_F for the minority spin channel.

This treatment of the interatomic interactions does not however include any contributions from the *Z* element, which in the case described above is Ge. Several interpretations using this *Z* atom have been used, although these are based upon the hybridisation between the two *X* atoms forming 6 t_{2g} hybrid orbitals and not three each of the t_{2g} and the t_{1u} hybrid orbitals as shown in Figure 3.2a **[87]**. Since these original works a number of more refined models have also been published. A comprehensive model which considers interactions between the *X*, *Y* and *Z* sites as well as the *s*, *p* and *d* orbitals for both minority and majority spin states is described in the review by *Graf et al.* **[84]**.

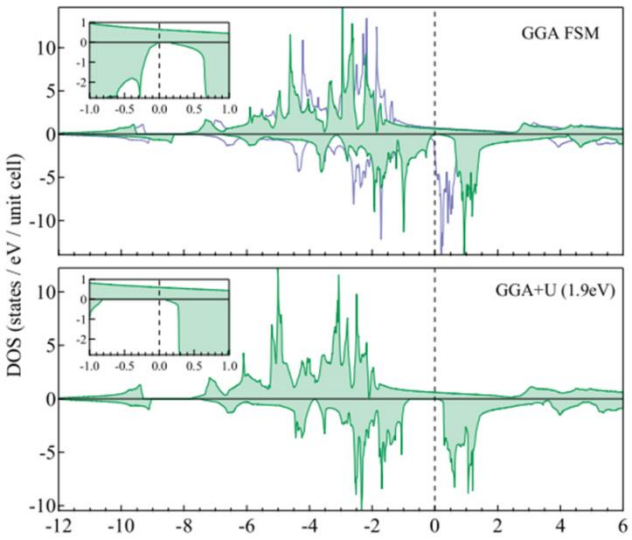

Figure 3.3. Total density of states for Co_2FeSi showing the difference between the use of the *+U* term in the DFT calculation **[88]**. The blue line represents the calculation using a standard GGA model.

Although the origin of the half-metallic properties for all Co-based Heusler alloys is well understood, there are some large variations in the reported electronic band structures for these models **[86,89-92]**. These variations are often the result of the difference between the models used in the computation of the band structure. Almost all of the theoretical investigations of this electronic band structure have been carried out using density functional theory (DFT). This gives the ground state of the system through the functional of the electron density **[93]**. The main problem with

calculations performed using this method is that the calculation uses the ground state of the system so that all calculations must be made at T= 0 K, which is unrealistic for most experimental measurements. The other main downfall of DFT is that the potentials describing the interactions between electrons are not realistic. This means that certain approximations must be made. One of these assumptions is that the valance electrons are itinerant. However, for Heusler alloys this is not true, as the valence electrons can become strongly localised to the Co *d* orbitals **[86]**. Therefore, additional correction terms must be made to account for this, such as an electron-electron correlation term, often called the *+U* term **[30,89]**, the effect of which can be seen in Figure 3.3.

The densities of states shown in Figure 3.3 have been calculated using the generalised gradient approximation (GGA) for the energy density. This is a more accurate approximation than the widely used local density approximation (LDA) as it uses terms for both the energy density and the gradient of the energy density at a specific point. The *+U* term is the DFT formulation of the Hubbard model *U* term which describes the electron repulsion term effectively splitting localised *d* or *f* electrons from the itinerant background **[94]**. The difference in the effect of this term is clear as it not only changes the position of the Fermi energy in the band gap but also the shape of the density of states around the minority spin band gap **[88]**.

3.1.3. Generalised Slater Pauling Behaviour in Heusler Alloys

Slater **[95]** and *Pauling* **[96]** both studied the origin of ferromagnetism from the band theory of transition metals, observing that ferromagnetism in these compounds results from the intrinsic properties of the bands formed from the 3*d* orbitals. They discovered that the magnetic moment of a 3*d* metal (and also its binary alloys) can be estimated through the average number of valence electrons (N_v) available per atom. This results in the curve seen in Figure 3.4, where a peak occurs between N_v = 8 and N_v = 9 where Fe sits. Below N_v = 8 the magnetism is the result of localised electrons and these elements would typically exhibit *bcc*-like structures. Above N_v = 9 the magnetism is the result of itinerant electrons and the crystal structures are typically close packed **[97]**. The Co-based Heusler alloys are found in the former 'localised' region of the curve. Although the $L2_1$ structure is comprised of 4 *fcc* lattices, the result is in effect a supercell made up of 8 *bcc* CsCl-like unit cells. In this region of the curve the Slater-Pauling rule can be approximated to **[90]**,

$$m \approx N_v - 6, \tag{3.1}$$

However, for half metallic ferromagnets, the band gap for the minority states requires that the number of filled minority states be an integer. For the rule as approximated above, the number of minority states may be non-integer if the value of the average number of valence electrons is not an integer value. For these compounds, it is better to generalise the number of valence electrons per atom to the average number of valence electrons per formula unit $N_{\text{f.u.}}$ so that for a full Heusler alloy with X_2YZ structure equation 3.1 becomes **[90]**

$$m_{X_2YZ} \approx N_{f.u} - 24. \tag{3.2}$$

This generalised Slater-Pauling rule, equation 3.2, has also been found to hold for quaternary compounds such as $Co_2Fe(Al,Si)$ **[84]**.

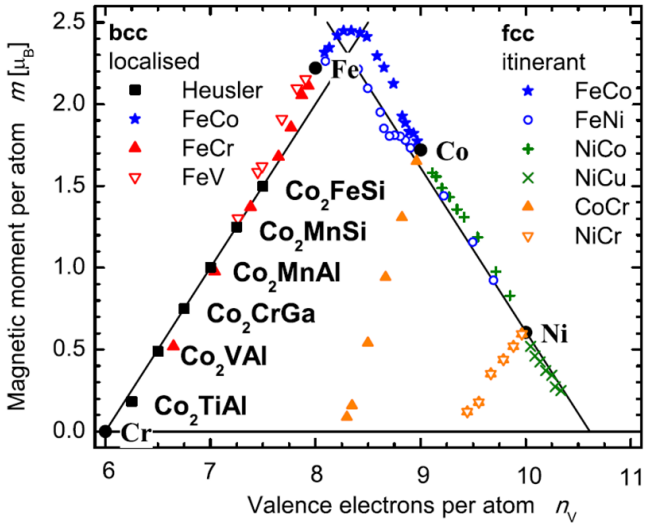

Figure 3.4. The dependence of the magnetic moment for 3*d* elements and compounds on the average number of valence electrons per formula unit showing the Slater-Pauling relationship **[84]**.

Figure 3.4 also shows that the magnetic moments in Heusler compounds can be controlled by the valance of the *Z* atom in the structure. It is clear to see that the compounds where the *Z* atom has 4 valence electrons, in this case Si, have a higher moment than an equivalent compound with 3 valance electrons (Al and Ga). This unusual behaviour is a result of an increased number of *d* electrons in the bands resulting from these *Z* atoms. This is extremely important for the development of new Heusler compounds as it means that the alloy can be engineered to provide specific magnetic characteristics.

The agreement with the Slater-Pauling curve and the dependence of magnetic moment on the valence electrons opens up the ability to engineer the properties of Heusler alloys continuously. By substituting varying amounts of the constituent atoms it is possible to change both the magnetic moment as well as the band structure. This technique has been used to engineer quaternary compounds such as $Co_2FeAl_xSi_{1-x}$ **[39,98]** and $Co_2Fe_xMn_{1-x}Si$ **[99]** that show a significant improvement in half-metallic properties. In fact the properties have been improved to such an extent that the highest ever published value of TMR (832% at 9K) was acquired using an MTJ with $Co_2FeAl_{0.5}Si_{0.5}$ electrodes **[34]**.

3.2. The Effects of Structural Disorder in Heusler Alloys

3.2.1. Magnetic Properties

Any variation away from Heusler stoichiometry or changes in the Heusler structure can have a large effect on the magnetic properties of the compound. In the previous section it was shown that the magnetism in the Heusler alloys is the result of the complex hybridisation of the atomic orbitals in the compound. As a direct result of this, any atomic swaps change this local hybridisation and as a result the band structure of the compound. Because the magnetic moments in Heusler compounds come from spin moments of valance electrons localised to the *d* orbitals of the Co atoms, any changes to the interatomic spacing also has a large effect on this localisation. In other words, any changes to the lattice constant in these materials can also have a dramatic effect on the magnetism. Because of the large variety of Heusler compounds it is impossible to describe how disorder affects all Co-based Heusler alloys. Therefore, Co_2FeSi will be the focus of this discussion due to it being the material of choice for experiments in this work.

Firstly, we consider the effect of disorder in the Heusler structure. The possible atomic swaps that disorder the $L2_1$ crystal can be reduced to Fe-Si ($B2$ disorder), Co-Fe (DO_3 disorder) and Co-Fe-Si ($A2$ disorder). The fully ordered $L2_1$ unit cell should result in a moment of 6 μ_B/f.u. In cgs units this equates to 1140 emu/cm^3 **[89]**. The effect of these atomic swaps has been calculated by *Li et al.* **[100]** using DFT. Their model predicts that Co-Fe swaps reduce the moment per formula unit to 5.5 μ_B with just 10% atomic disorder. The Co-Si swaps with the same amount of disorder are surprisingly predicted to result in an increase in the moment to 6.05 μ_B/f.u. This is due

to the resulting environment of the Co atom changing the symmetry of the interatomic bonds and promoting an increased atomic moment for the Co site. The Fe-Si swaps forming *B*2 disordered structures were found to retain the 6 μ_B moment predicted for the $L2_1$ structure up to 10% disorder. This is however contrary to a number of experimental studies which show a decrease in magnetic moment with increasing *B*2 ordering **[90,101,102]**. This is most likely due to the effect of widespread disordered regions in the materials and not to just atomic swapping localised to the unit cell.

Variation in the lattice parameter of Co_2FeSi has also been shown to affect the magnetic moment. The lattice parameter of bulk Co_2FeSi is reported to be 5.64Å **[90,103]**. However, in thin films, the lattice parameter has been shown to expand and contract dependent upon the growth mechanism and factor such as choice of substrate and buffer layers **[104]**. These variations in lattice parameter can either increase or decrease the intensity of the magnetic moment. Compression of the lattice parameter by 6% has been shown to give a reduction of the magnetic moment from the bulk value of 6 μ_B to 5 μ_B **[89]**. However, an increase in the lattice parameter of up to 10% is shown to provide only small variations ±0.15 μ_B **[89]**. These variations in magnetic properties are small when compared with the effect that structural variation and disorder have on the half-metallicity and, as a result, spin polarisation of these materials.

3.2.2. Half-Metallicity

The effect of disorder on the half-metallic nature of Heusler alloys is considerably larger than that induced by lattice changes. This is due to the sensitivity of the band gap for minority spin states to changes in the hybridisation of atomic orbitals due to changes in atomic positions **[105,106]**. In the experimental results it is extremely hard to quantify the effect of different types of disorder as they are often randomly distributed throughout a system, as well as being specific to the particular experiment. To give some understanding a number of atomic swap type disorders are considered in the literature. Fe-Si (*B*2) and Co-Fe-Si (*A*2) **[91]** disorders are most widely studied with some consideration for Co-Fe (DO_3) **[107]**. Unfortunately the models used to calculate the extent of disorder are often limited by the size of the initial unit cell considered. For example, one on the most extensive studies on the effect of disorder in Co_2FeSi-based alloys by *Gercsi and Hono* **[91]** only used a sixteen atom unit cell, which limits the minimum amount of disorder to 25% for *B*2 type and

12.5% for the *A*2 and *DO*$_3$ types. However, this is enough to acquire some understanding of how these disorders affect the half-metallicity.

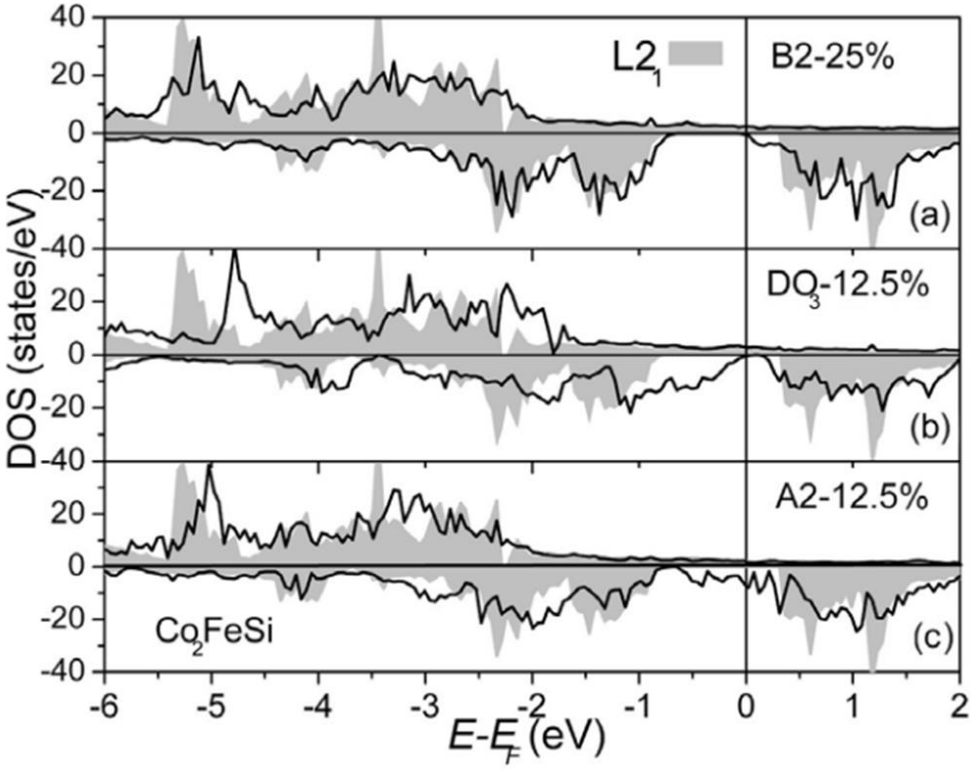

Figure 3.5. Variation in the spin dependent density of states for Co_2FeSi with different quantities of a) *B*2, b) *DO*$_3$ and c) *A*2 disorder. The *L*2$_1$ spin density of states is shown in grey as a reference **[91]**.

As can be seen in Figure 3.5, the different disorders affect the density of states in different ways. The *B*2 type disorder is seen to retain the minority state band gap and as a result the half-metallic conduction properties even at 25% disorder. This maintenance of the band gap for the *B*2 ordering is because of the lack of the disorder to the Co-Co symmetry in the lattice. It has been shown that the band gap is constructed of 3*d* states localised to the Co atoms **[108]**. Therefore, if these states are not altered by the disorder, the half-metallic electronic properties should remain. For the *DO*$_3$ disorder, the band gap is reduced and moves relative to E_F, producing a small but finite number of states for the minority channel at E_F. However with, the *A*2 disorder the band gap is completely destroyed and there is an increase in states for the minority channel resulting in a small inverse spin polarisation. The inversion of spin polarisation has been identified experimentally **[109]**.

As with the magnetic moment, the size of the unit cell can have an effect on the calculation of the spin polarisation. This effect is especially prevalent in DFT

calculations, like those used most often to predict the properties of half-metallic ferromagnets, as it manipulates the ground state charge density in the unit cell. This effect has been shown in Co_2FeSi, where predictions suggests that the bulk lattice parameter of 5.64 Å may not give the expected half-metallic behaviour. By increasing the lattice parameter to 6.20 Å the half-metallicity is regained **[89]**. The effect of the lattice parameter expansion on the half metallicity can be seen in Figure 3.6. However it must be noted that since these calculations were performed a number of works have studied more complex and accurate models, predicting Co_2FeSi with the bulk lattice parameter to be half-metallic **[91,92]**.

These calculations use the GGA and GGA+U approximations in the DFT models. This means that the shape of the potential for each of the atoms is more carefully defined, as are the inter-electron interactions. This provides a more realistic prediction of the half-metallicity as it defines the localisation of the *d* electrons on the Co atomic sites. This may be the effect exploited by increasing the lattice parameter as it separates the Co orbitals, changing the electron interaction.

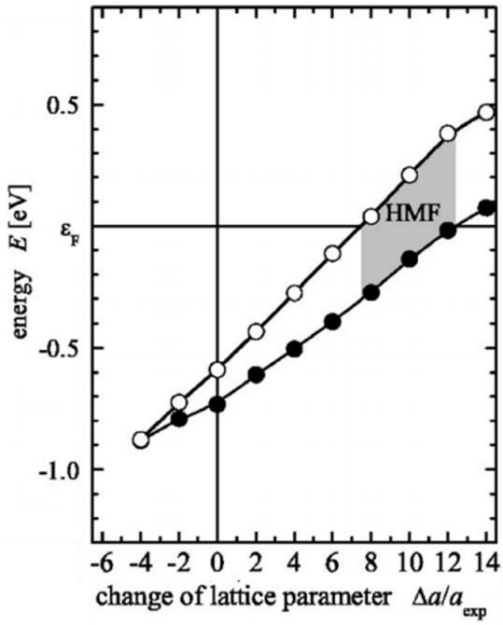

Figure 3.6. The effect of the lattice parameter on the minority band gap for Co_2FeSi. Open and closed circles correspond to the energy of the top and bottom of the band gap respectively **[89]**.

This means that any Heusler alloy samples must be extremely well characterised if any quantitative assessment of their magnetic and electronic properties is to be carried out. Measurements of the atomic ordering and lattice

constant are paramount. However, direct measurement of the band gap in the minority states is extremely difficult.

3.3. The Effects of Surfaces and Interfaces on Half Metallicity

As well as structural disorder and lattice distortion, interfacing Heusler alloys with other materials can also change their magnetic and electronic properties. When chemically bonded to another material, the hybridisation of the electron orbitals changes distorting the band structure of the Heusler alloy. The study of these interface structures has primarily been focused towards the interfaces between Heusler alloys and commonly used substrates **[110,111]** and tunnel barrier materials **[112,113]**.

It is useful initially to study the effect of terminating the Heusler alloy to form a surface. Unfortunately, there is very little data on the effects of surface termination of Co_2FeSi. However, a large amount of work has been carried out using the similar material Co_2MnSi. It is found that only a pure Mn termination with a Co subsurface preserves the band gap in the minority channel **[114]**. Due to the surface electronic structure, a number of states appear in this band gap severely degrading the half-metallic features of the other termination, e.g. MnSi or pure Si terminations.

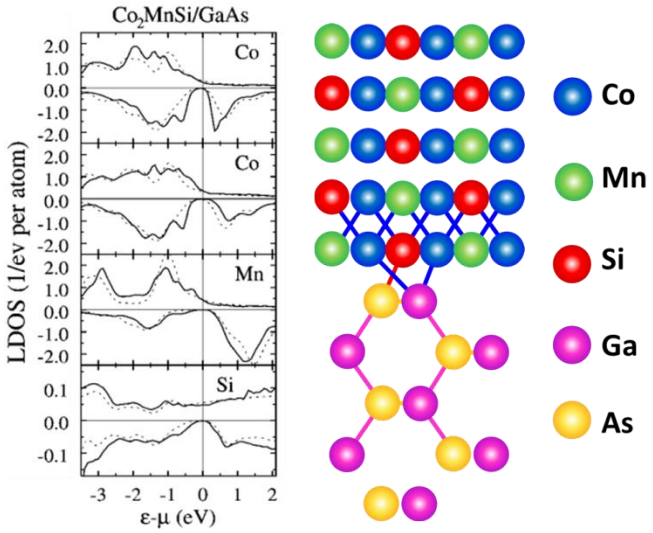

Figure 3.7. Local density of states for each atom at the GaAs(110)/Co_2FeSi(110) interface and schematic of the interface with interfacial bonds **[110]**.

When interfacing Co-based Heusler alloys with GaAs for spin injection studies it is found that the half-metallicity can be preserved, even for surfaces which when terminated show no half-metallic characteristics **[115]**. At the typical GaAs(001) /Co_2MnSi(001), interface dangling bond orbitals from the GaAs hybridise with the

Heusler alloy and create interfacial states at the Fermi energy thus destroying the half-metallicity. If the interface is constructed of two (110) surfaces the orbitals in the Heusler alloy hybridise in such a way as to force the GaAs localised state away from E_F thus preserving the half-metallicity. This interface also has no Co-As bonds which contribute localised states at the Fermi energy. The GaAs/Co_2MnSi interface and the local density of states for each atom are shown in Figure 3.7. The properties of the interface between Co-based Heusler alloys and insulating materials such as MgO or AlO_x are again different. These interfaces are extremely important as they can control the maximum achievable value of TMR for a magnetic tunnel junction, as well as the temperature dependence of that value **[115]**. Extremely high values of TMR (>500%) have been measured for systems with AlO_x **[116]** but this can be improved by using crystalline MgO barriers.

By using a crystalline MgO barrier the coherent tunnelling effect can be exploited. This was initially observed in Fe/MgO/Fe(001) junctions **[117]** after being theoretically predicted by *Butler et al*. **[23]**. Coherent tunnelling occurs when the electron wavefunction remains coherent through the entire junction. This means that the same electron band symmetry is preserved though the entire junction. In Fe/MgO/Fe(001) junctions this occurs for the Δ_1 band in the majority spins states but not for the minority states resulting in a prediction of half-metallic conduction **[23]**. The same situation arises for Co-based Heusler alloy MTJ's with crystalline MgO barriers **[115]**. Once again taking Co_2MnSi as the example, it was found that the interfacial bonding can also result in the creation of interfacial states in the minority band gap. This effectively destroys the half metallicity and therefore spin polarisation of the electrode, therefore reducing the maximum TMR ratio if considered in terms of the initial *Julliere* model, equation 3.3 **[20]**. P_1 and P_2 are the value of spin polarisation for the top and bottom electrodes respectively.

$$TMR = \frac{\Delta R}{R} = \frac{2P_1P_2}{1 - P_1P_2} \tag{3.3}$$

As well as being affected by the reduction of spin polarisation of the electrodes the TMR ratio in these films also shows large temperature dependence. This has been suggested to result from an increased contribution from the interfacial states at higher temperature. At low temperature there are relatively few spin-flip transitions which allow conduction from the minority band. However, at higher temperatures the

probability of these spin-flip transitions increases. This increases the contribution to the conductance from electrons in the minority states resulting in a further and accelerated decrease in the TMR value with increasing temperature **[118]**. The same temperature dependence is not seen in MTJ's with typical ferromagnetic (Fe or CoFeB) electrodes **[119]**.

3.4. Experimental Observations of Heusler Alloy Spin Polarisation

Many observations have been made of large spin polarisation in spintronic devices using Co-based Heusler alloy ferromagnetic layers. The devices primarily fall into the categories of MTJ's **[34,82]** or spin valves **[19,41]**, although some devices such as spin LED's **[109]** have been used to measure directly the spin polarisation. As well as many different device geometries, there has also been a broad study of Co-based Heusler alloys. For the sake of clarity, $Co_2FeAl_{1-x}Si_x$ alloys will be the focus of this discussion particularly the limiting case Co_2FeSi. Typically, Heusler alloy magnetoresistive devices have very similar basic properties. The films are predominantly grown epitaxially onto MgO(001) substrates, which are usually buffered with some combination of Cr and Ag, to form a bottom electrode **[41,82,120]**. Devices are then fabricated using a combination of electron beam and photolithography. The main variables then become the non-magnetic spacer layer, typically Ag for GMR junctions **[41,42]** and MgO for MTJ's **[38,82]**, and the annealing temperatures to form the $L2_1$ phase of the alloys.

In the context of later results, those for Co_2FeSi tunnel junctions are relatively poor, with a maximum reported value of 60% at 5K for electrodes of entirely Co_2FeSi **[38]**. This value has been increased by the use of multi-layered Co_2FeSi and Co_2MnSi to a maximum of 114% at 17K **[60]**. This relatively low value of TMR is most likely due to the destruction of the half-metallic state in the junction from the interface states, as well as deformation of the lattice at these interfaces **[38]**. As discussed earlier in this section it is debated as to whether Co_2FeSi is half-metallic at all. As a result of the differences in assumptions made and parameters used in different theoretical models, there are contradicting reports of the extent of the bad-gap for minority states in Co_2FeSi. Much more impressive results have been found using $Co_2FeAl_{0.5}Si_{0.5}$. The largest ever TMR ratio (836% at 8K **[34]**) has been observed using epitaxially evaporated $Co_2FeAl_{0.5}Si_{0.5}$ electrodes. Extremely high GMR ratios (80% at 14K **[41]**) have also been observed using sputtered films. These devices show that for

$Co_2FeAl_{0.5}Si_{0.5}$, a much higher spin polarisation is recovered due to the engineering of the position of the minority band gap about E_F. All these results have a number of problems when considering the application to commercial devices. They all require UHV deposition and high temperature (>400°C) annealing. These possible problems may be overcome by using polycrystalline films, which will make up the bulk of this work. These films have recently been shown to give reasonably high GMR ratios (>10% at RT) while also having a lower resistance area product ($3\mu\Omega m^2$) and being formed at much lower temperatures (<400°C) **[44]**. This makes devices fabricated from these types of films potentially more efficient and commercially viable.

To measure the spin polarisation directly, *Bruski et al.* **[109]** fabricated Co_2FeSi based Spin LED's. By using electroluminescence measurements, the degree of circular polarisation of emitted light is measured. This circular polarisation is directly proportional to the spin polarisation. A maximum value of 57% spin polarisation was achieved in these films. This is attributed to mixing of $L2_1$ and $B2$ phases due to low annealing temperature. One unusual result from this study is that in a film exhibiting long range $B2$ ordering a spin polarisation inversion of 27% is observed. This variation in properties occurs due to annealing the film at 300°C or not annealing it respectively. This highlights the need for extremely good characterisation of Heusler alloy film structure when creating devices.

Chapter 4. Growth and Structural Characterisation

4.1. Techniques for Heusler Alloy Growth

4.1.1. High Target Utilisation Sputtering

High Target Utilisation Sputtering (HiTUS) is a form of plasma sputtering that differs substantially from the more conventionally used magnetron sputtering. The most important distinction is the generation of the plasma remote from the target surface. In the system used at York the plasma is generated in a side arm using a 2.5kW RF antenna (Figure 4.1). The side arm consists of a quartz tube surrounded by a 3–turn copper RF antenna. The 13.56 MHz RF field is coupled inductively to the Ar gas at lower pressures than in the main sputtering chamber.

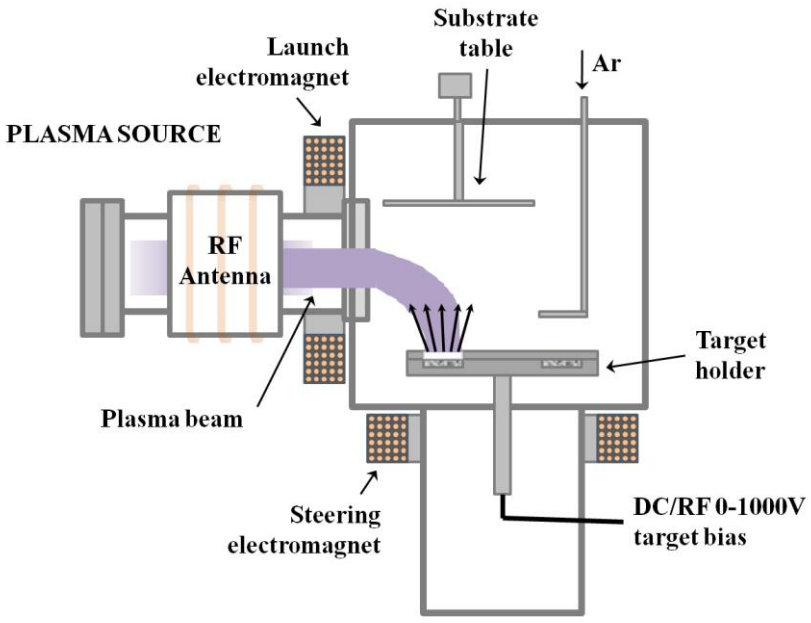

Figure 4.1. Schematic diagram of the HiTUS system.

The plasma is then launched into the sputtering chamber and steered onto the 5 cm diameter water cooled target by two electromagnets. The two magnets apply different strength fields allowing the ions in the plasma to follow the flux lines of the launch electromagnet into the chamber where the higher field steering electromagnet overcomes the field from the launch electromagnet, steering the ions towards the target surface. The ions of the Ar plasma follow field lines through a process of ambipolar diffusion. The resulting plasma beam has a high ion density (10^{12} -10^{13} ions/cm^3) **[121]** which allows sputtering at a high rate (0.8 Å/s). The plasma beam at the target surface is composed of low energy ions (<10 eV) which are not of sufficient energy to sputter material. The plasma beam is therefore coupled to a DC bias voltage applied to the target which allows an increase of ion energy to a value above the threshold required for sputtering. The bias voltage can be varied above this threshold resulting in highly controlled sputtering of the target material. The separation of plasma generation from the sputtering chamber is the key element in achieving deposition with a wide range of controlled process parameters. It is also possible to turn off the second electromagnet, resulting in a plasma of low energy ions (<30 eV) surrounding the substrate holder. These low energy ions can be used to remove surface contaminants from the substrates before film deposition **[122]**.

Controllable parameters include the Ar ion energy at the target surface through the applied bias to the target, the Ar ion density through control of the Ar gas flow rate during deposition and the initial ion energy through variation of the RF power supplied through the antenna. Variation of each of these parameters results in varying degrees of control over the grain size distribution within the sputtered films **[122]**. Bias voltage, process pressure and RF power all give a monotonic increase in mean grain diameter. As a result of this wide ranging variation in grain size with process parameters, it is important to control a number of these parameters so that the deposited films are comparable. The deposition of thin films in this work was carried out at a constant process pressure (2.5×10^{-3} mbar) and RF power (1.5 kW). The grain size or structure of the as-deposited films was therefore controlled through variation of the DC bias voltage applied to the target. The process pressure is controlled by a dedicated mass flow controller with the possibility to use set points for gas flow or chamber pressure. A chamber pressure set point of 2.5×10^{-3} mbar was used which results in an average Ar flow rate of 29.5 sccm. The RF power is controlled as a

percentage of the maximum power of the supply (2.5 kW) allowing 100 discreet settings.

The HiTUS system at York also has a number of other features that make it applicable for the deposition of a wide range of thin film structures. The sputter targets are held in an 8 target carousel. This means that complex multi-layered structures can be created from up to 8 eight different elements or alloys without breaking vacuum. Due to the HiTUS eroding material from the entire target surface, it is particularly suitable for the sputtering of alloyed targets. This feature also allows the use of composite targets where the surface composition of the target can be varied to change the sputtered film structure. The substrates onto which the films are deposited are also held within a 6 substrate carousel allowing 6 samples of variable composition to be created without breaking vacuum. Each substrate holder can hold a maximum of one 20 × 20 mm substrate. Another important feature of the HiTUS is that the substrate carousel is held 30 cm above the target and therefore out of the plasma beam. The result of this is no re-sputtering from the substrate or target during deposition, removing any unusual substrate dependent growth parameters. This target-to-substrate distance also results in a relatively slow growth rate so that the deposited films show excellent uniformity across the entire sample with low surface roughness (<2 nm peak to peak).

4.1.2. Heusler Alloy Growth

The HiTUS system has recently been used for the deposition of Heusler alloy films **[123]**. The group at York are the only group to use this technique for Heusler alloy growth. Heusler alloy films deposited through HiTUS sputtering are quite unlike any of those deposited by magnetron sputtering or MBE growth. Unlike commonly used epitaxial films, these HiTUS grown films exhibit little or no structural ordering in the "as-deposited state". Through annealing, large crystals or grains begin to form out of the as-deposited amorphous matrix. After heating for up to 6 hours, films show a remarkable distribution in grain size with median grain diameters ranging from 30 nm to 250 nm depending upon the deposition bias voltage **[124]**. These films also show a large variation in crystallographic orientation, with grains observed with [100], [111], and [112] projections out of the plane of the film. *Fleet et al.* suggest that this is a result of initial nano-crystal nucleation sites in the as-deposited matrix, with a layer-by-layer crystallisation mechanism for those films found with [112] orientation.

For films annealed for longer than 6 hours, a decrease is seen in the median grain diameters for all films. This is explained by a process of Si-segregation out of the bulk of the ordered grains **[123]**.

4.1.3. Magnetron Sputtering

Magnetron sputtering is one of the most widely used techniques for the deposition of magnetic thin films, having found widespread application in the magnetic storage industry. In the magnetron process, a glow discharge plasma is achieved above the target and the energetic ions are accelerated towards the target surface by a cathode situated below, to which a negative potential of a few hundred volts is applied **[125]**. The bombardment of the target by ions erodes material from the target. The rate at which material is eroded depends upon the energy and mass of the ions, as well as the number of ions incident on the target. This ion bombardment also leads to the emission of secondary electrons which cause further ionisation events, helping to maintain the plasma. By applying a magnetic field parallel to the target surface as shown in Figure 4.2, the secondary electrons can be confined near the target surface. This increases the number of ionisation events in this region leading to a higher density plasma and increased sputtering rates. Below the confined electrons there is a region of increased erosion leading to a characteristic 'race-track' appearing on the target surface. This limits target lifetime and prevents the use of composite targets.

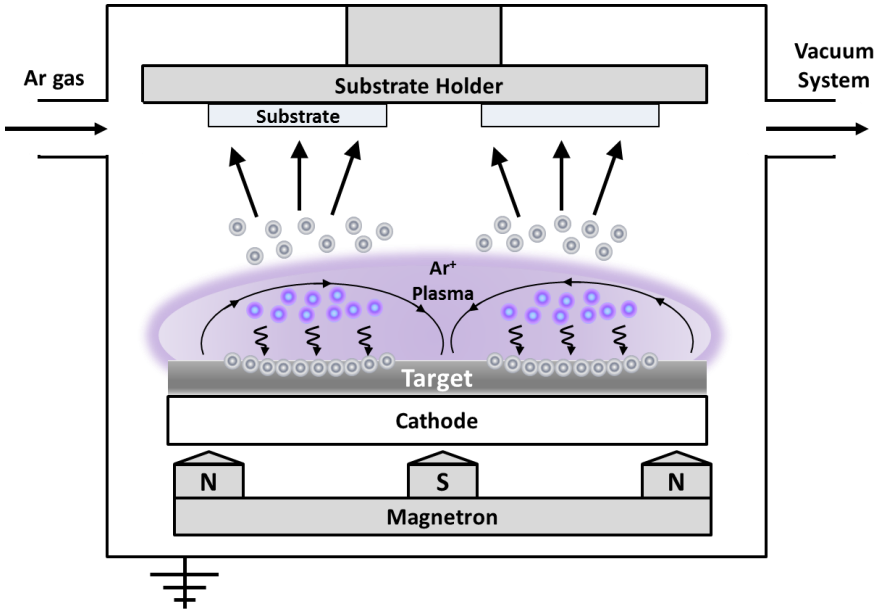

Figure 4.2. Schematic diagram of a conventional magnetron sputtering system.

One major drawback of sputtering is the difficulty of sputtering insulating materials. The placement of the cathode below the target as shown in Figure 4.2 means that the ions will still be accelerated towards the target thus sputtering will occur. However after a short time (10^{-7} s) a positive charge will build up on the target surface thus deflecting further ions as the negative potential applied to the cathode is overcome. This effect can be removed by reversing the connections and applying a positive potential to the cathode thus building up a negative charge on the target. Supplying the cathode with RF-power at a frequency of 1 MHz or greater is enough to overcome this positive charging effect while still achieving a practical sputtering rate (≥ 1 Å/s) for insulating materials **[125]**.

Magnetron sputtering is the most commonly used technique for Heusler alloy deposition. This is the result of a desire to make research appropriate to industry where sputtering is the most widely used deposition technique. Magnetron sputtering has since been used to deposit most half-metallic Heusler compounds, including the most widely studied compounds $Co_2(Cr,Fe)Al$ **[63]**, Co_2MnSi **[126]** and $Co_2Fe(Al_{0.5}Si_{0.5})$ **[120]**, with which the world record value of TMR has been achieved. These sputtered thin films typically show large amounts of $L2_1$ ordering after thermal annealing. Sputtering has also been used to carry out wide-ranging materials studies where target composition can be controlled to modify film properties.

4.2. Structural Characterisation

4.2.1. Transmission Electron Microscopy (TEM)

Transmission electron microscopy (TEM) is one of the most powerful research tools for studying the structural and chemical properties of a sample down to the atomic level. Since the first TEM went into production by the Vickers company in 1936 **[127]** a very large number of different microscopes with many different configurations and specifications have been produced. The basic, or typical, TEM set-up is shown in Figure 4.3.

In this thesis, a large proportion of the microscopy has been carried out using a JEOL JEM-2011 TEM, which is a typical TEM in that it has an optical arrangement similar to that shown in Figure 4.3. The electron source is a Lanthanum hexaboride (LaB_6) filament which emits electrons through a thermionic process. These electrons are then accelerated through a potential to high energy, typically 200 keV. Once

accelerated into the microscope column the electrons are focused into a small (2-3 μm) coherent electron beam by the condenser lens. Consisting of a number of electromagnetic lenses and apertures, this system controls the intensity and spot size of the beam incident on the specimen. The size of the beam can then be further restricted by a user selectable condenser aperture. This condenser aperture removes higher angle electrons from the beam increasing the uniformity of radiation illuminating the specimen. These apertures can also be used to limit the beam intensity for imaging of specimens that are highly susceptible to beam damage. The electrons then reach and interact with the specimen. This interaction happens through a large variety of mechanisms shown schematically in Figure 4.4. Due to the large number of interactions a number of different imaging modes can be used.

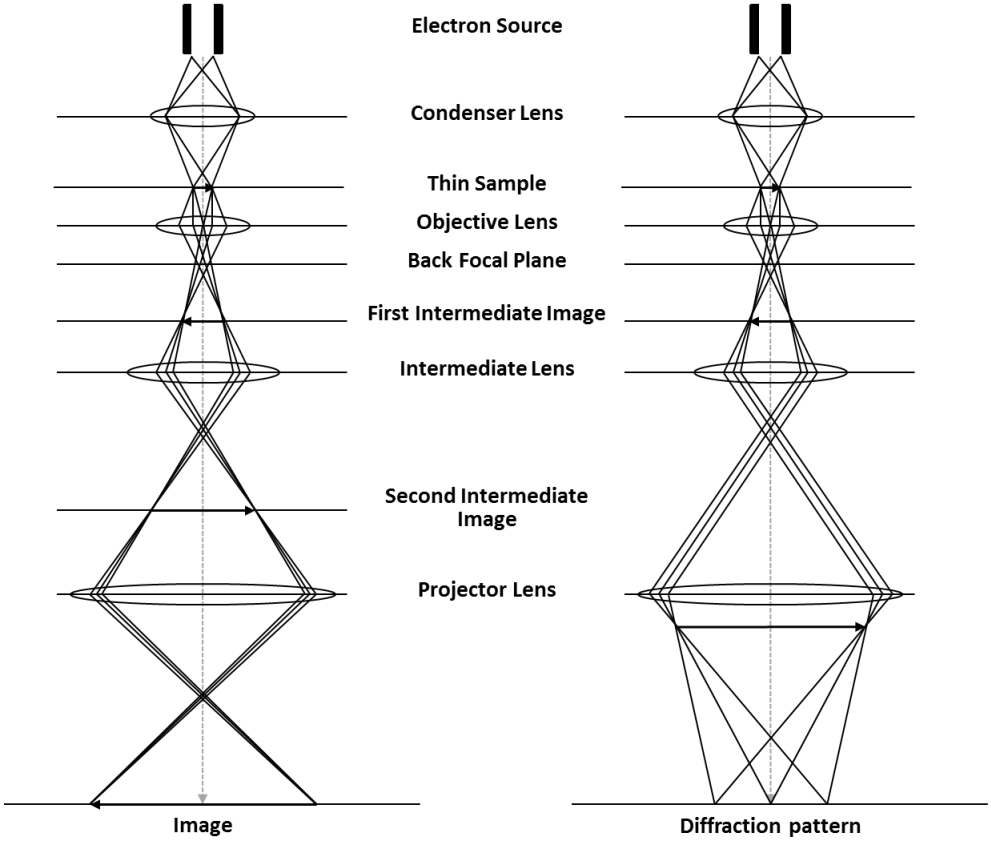

Figure 4.3. Ray diagrams for typical TEM configurations showing mechanism for the formation of images (left) and diffraction patterns (right) **[127]**.

The sample itself sits within the pole pieces of the objective lens. This lens focuses the scattered transmitted electrons to form an intermediate image between the objective and intermediate lenses. In the back focal plane of the objective lens is a

set of objective apertures. These allow selection of electrons scattered to specific positions in the diffraction pattern so that different imaging modes or improved contrast can be used. The intermediate image formed from the objective lens is further focused and magnified by the intermediate lens. This intermediate lens is of variable strength, which allows for the projection of either an image or a diffraction pattern as shown in Figure 4.3. The image is then further magnified by a number of projector lenses, not shown in the diagram, which eventually focus the image onto either a fluorescent screen or a charge-couple device (CCD) camera.

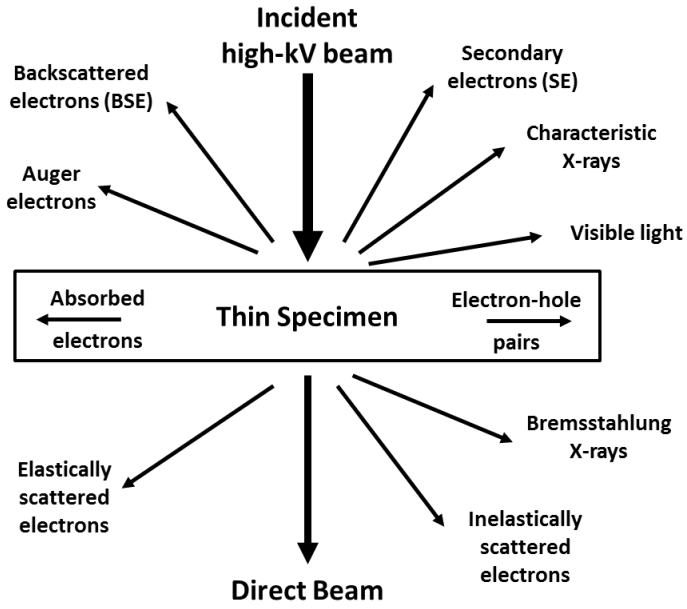

Figure 4.4. Signals generated through electron interactions with a thin specimen in a TEM **[127].**

The large number of interactions between the electron beam and the specimen allow for the use of many different imaging techniques. The most commonly used imaging mode is bright-field imaging. In this mode, an objective aperture is inserted into the back focal plane of the objective lens blocking electrons scattered to higher angles, allowing only the main electron beam to pass.

Another commonly used technique is dark-field imaging. In this mode, the objective aperture is positioned to allow only the passage of electrons scattered to a specific position while blocking out the main beam. This technique is used for the grain size analysis in this work as it allows imaging of grains diffracting to a specific part of the diffraction pattern. This reduces the error associated with measuring separate grains of similar bright field contrast as a single grain. Both these techniques

rely on diffraction contrast, that is contrast associated with the number of diffracted electrons, and the angle through which they are diffracted. For bright-field imaging, regions of significantly higher crystallinity or atomic number diffract more electrons to higher angles, resulting in dark contrast for those areas. In dark-field imaging the regions from which the selected electrons are diffracted appear light.

Dark-field imaging can be used in many different ways to give increased understanding of the complex microstructure of thin films. One of the most useful of these techniques is weak-beam dark-field imaging (WBDF). The weak beam condition is achieved through tilting of both the specimen and the electron beam. Once the specimen is tilted into the required orientation for imaging, in the case of Figure 4.5 the MgO(020) zone axis, the beam is then tilted so that a large deviation from the optical axis and intended imaging plane is achieved. The specimen is then imaged in the dark-field along the initial intended reflection. This means that although the majority of atomic planes in the film no longer fulfil the Bragg condition, a number of planes may be locally bent back towards the diffraction plane, thus fulfilling the Bragg condition. In real terms this means that atomic planes that are locally deformed such as those around a defect will appear light against the darker background highlighting the effect of the defect. Figure 4.5 shows this for the interface between MgO and Co_2FeSi, where lattice mismatch between substrate and film is compensated by a series of misfit dislocations at the interface. A full description of setting up the WBDF condition can be found in the standard text, Transmission Electron Microscopy **[127]**.

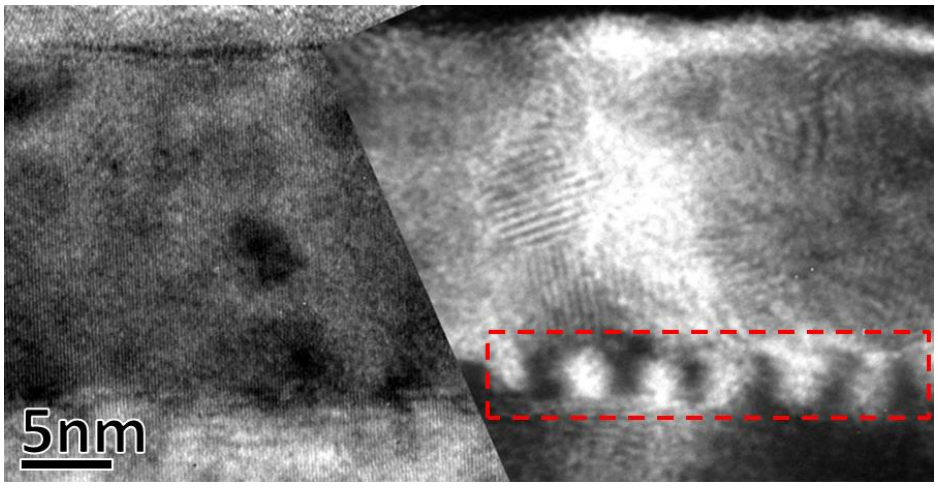

Figure 4.5. TEM images showing the interface between an epitaxially sputtered Co_2FeSi film and MgO substrate, the contrast difference between bright field image (left) and weak beam dark field image (right) is shown clearly. The highlighted region shows the contrast resulting from misfit dislocations at the interface.

4.2.2. Selected Area Electron Diffraction (SAED)

Electron diffraction allows some of the most detailed structural analysis that can be performed in a TEM. If a crystal structure is present in the specimen then electrons passing through will be diffracted by the atomic potentials to particular conditions that satisfy the Laue condition for constructive interference, equation 4.1.

$$\boldsymbol{L} = \boldsymbol{g}, \tag{4.1}$$

where $\boldsymbol{L}$ is the vector describing the difference between the incident and exit electron beam due to diffraction, and $\boldsymbol{g}$ is the vector describing the reciprocal space positions of an atomic plane. However these are often simplified to the Bragg condition equation 4.2 for specific atomic positions.

$$\boldsymbol{L}_B = \frac{2sin\theta_B}{\lambda_e} = \frac{1}{d_{hkl}} = \boldsymbol{g_B}, \tag{4.2}$$

where λ_e is the de Broglie wavelength of the electron, θ_B is the angle between the incident electron beam and the diffracting lattice planes which satisfies the Bragg condition and d_{hkl} is the spacing of lattice planes given by equation 4.3

$$d_{hkl} = \frac{a}{\sqrt{h^2 + k^2 + l^2}}. \tag{4.3}$$

For cubic crystals a is the lattice parameter and h, k, and l are the Miller indices corresponding to the particular diffracting plane **[127]**. Electron reflections that satisfy these conditions result in bright spots or rings dependent upon the specimen. The diffraction pattern can then be analysed to give information about the crystallinity of a sample (whether it is mono or polycrystalline) and if there are multiple phases of material in the specimen. This last point is particularly useful for Heusler alloys where a number of different disordered phases may exist in a single specimen. Diffraction can also give extremely important information about the epitaxial relationship between different layers in a film.

These parameters are true for any TEM beam size. However, for various reasons it is often unsuitable to take a diffraction pattern from a large area, most notably that the specimen may often be buckled giving a confused pattern. This can be overcome by a number of techniques, including converging the beam to a small spot (CBED) but most easily and usually through the use of selected area electron diffraction (SAED). In this technique an aperture is inserted exactly into the image

plane of one of the lenses subsequent to the specimen, thus creating a virtual aperture at the specimen plane. It is important to focus the diffracting beam correctly so that the aperture is exactly conjugate with the specimen. Then any electron hitting the specimen outside the defined aperture also hits the real aperture as well **[127]**.

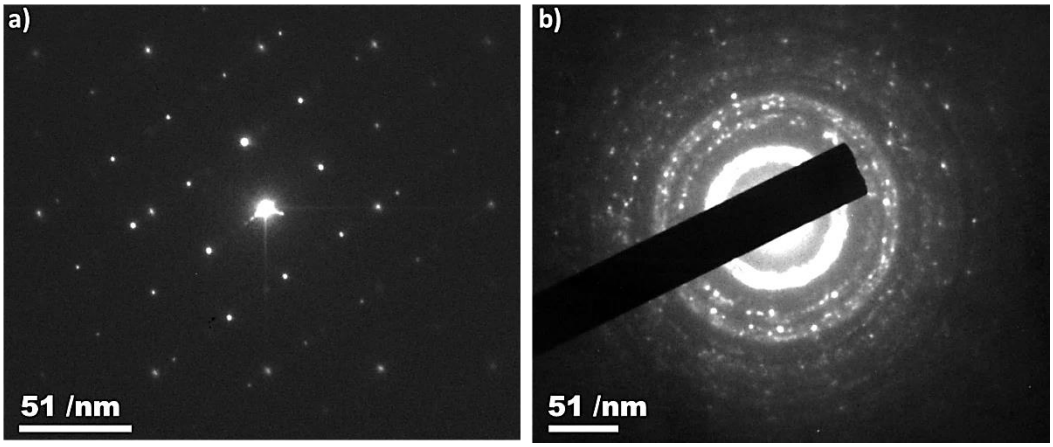

Figure 4.6. a) SAED diffraction pattern from a Fe_3Si interface showing monocrystalline diffraction pattern. b) SAED diffraction pattern of polycrystalline Co_2FeSi film.

Figure 4.6 shows typical SAED patterns for monocrystalline and polycrystalline thin films. The monocrystalline pattern shows spots in specific positions depending on the reflections that obey the Bragg conditions. This can be used to easily evaluate the epitaxial relationship between film and substrate. The intensity of spots in these diffraction patterns can in principle give quantitative information about ordering in the film. However, this is difficult to achieve as thickness variation and sample tilt can result in increased or reduced intensities across the diffraction pattern. The appearance of particular allowed reflections due to different material phases is however easily observed, which makes SAED diffraction of this type useful for identifying $B2$ and $L2_1$ ordered Heusler alloy films. The random orientation of grains in the polycrystalline specimen results in a rotation of the reciprocal lattice through all axes producing a ring pattern as seen in Figure 4.6b. This is analogous to X-ray diffraction as described in section 4.2.5. The radial separation of the rings from the main beam is the result of specific reflections. However, due to the complex structure of the polycrystalline films in this study, these rings are widened or smoothed resulting in hard to analyse patterns. Some of the rings are made of discrete spots due to the large grains in the specimen **[127]**.

4.2.3. High Resolution TEM with Aberration Correction

A large amount of work in this thesis is focused towards the characterisation of the crystallographic structure of the various samples. In order to image this crystallographic (or even atomic) structure, resolution in the sub angstrom regime must be achieved. In situations like this, a typical microscope such as the JEOL JEM-2011 used in some of this work may not be enough. The accessible resolution in a TEM image is the result of the Fourier transform of the accessible spatial frequencies resulting from the diffracted electron beam after transmission through the sample. For high resolution imaging, high spatial frequencies must be accessed. There are two main contributing factors to the resolution limit in TEM. One term from the microscope and one term from the specimen itself. The term from the specimen can be summed up as a specimen thickness term. If the specimen is thin enough that the amplitude of the project potential of the specimen is linearly related to the amplitude of the transmitted wave, this is known as the weak phase approximation.

The term from the microscope is described by what is often called the contrast transfer function of the microscope $T(u)$, where u is the spatial frequency **[127]**.

$$T(u) = A(u)E(u)B(u) \tag{4.4}$$

Here $A(u)$ is the aperture term, which is simply adjustable dependent on the radius of aperture used while imaging. The two more complex terms are the envelope term $E(u)$ and the aberration term $B(u)$. First let us address the envelope term, which forms a damping term and a cut-off point for the accessible spatial frequencies. The largest contribution to this envelope term comes from the spatial coherence of the illumination, or what is also known as chromatic aberration. To reduce this aberration the energy spread of the electrons from the gun must be controlled. The JEOL JEM-2011 typically uses a LaB_6 filament and thermionic emission to form the electron beam. The typical energy spread from such a source is ~1.5 eV (at FWHM). The JEOL JEM-2200FS also used in this work uses a field emission gun with a typical energy spread of 0.3 eV or 5 times smaller than that of hot emission guns **[127]**. The change of gun instantly improves the range of accessible spatial frequencies.

The final term in equation 4.4 is the aberration term, which is most commonly expressed in terms of an exponential with the exponent $\eta(u)$ **[127]**.

$$\eta(u) = \pi \Delta f \lambda_e u^2 + \frac{1}{2}\pi C_s {\lambda_e}^3 u^4 \qquad (4.5)$$

In equation 4.5 we see that the resolution limit becomes the product of three terms, the electron wavelength λ_e, the defocus value Δf, and most importantly the spherical aberration coefficient C_s. Spherical aberration is an inherent feature of all magnetic lenses. It is a result of the magnetic field acting in-homogeneously on electrons displaced from the optical axis. The larger the displacement from the optical axis, the larger the force exerted on the electron. This results in a broadening of a point image *P*, to a disk of finite radius *R* in the Gaussian image plane. In terms of equation 4.5, C_s adds an extra and much larger term to the aberration.

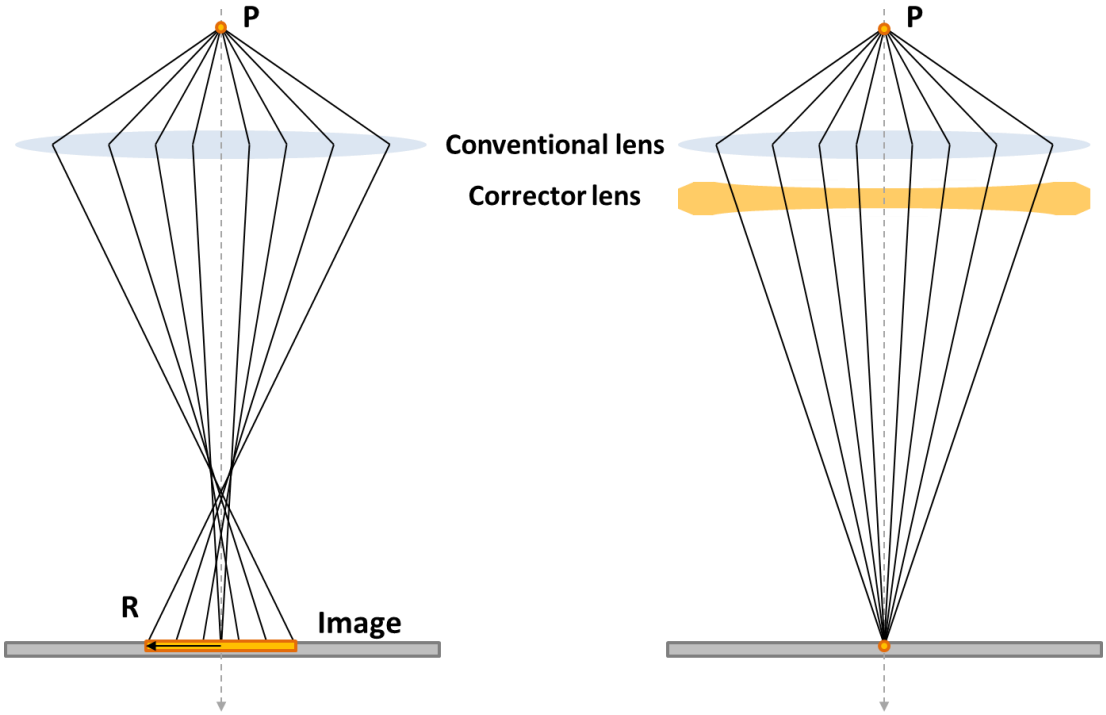

Figure 4.7. Schematic diagrams of spherical aberration of a converging lens (left) and the effect of using a second diverging lens to correct the aberration (right).

In order to reduce the C_s factor from any real microscope a complex magnetic lens arrangement must be implemented. To create not just a converging lens but also a suitable diverging lens such as that shown in Figure 4.7, the ability to correct for C_s in this way was first demonstrated by *Rose* **[128]** using a combination of round and hexapole lenses. In this system, the round lenses act to steer the electrons while the hexapole elements correct the aberration. The C_s correctors in the JEM-2200FS are based upon the long hexapole/transfer lens as initially proposed by *Rose* **[128]**,

allowing correction of spherical aberration out to the third order. This however means that a fifth order term of the aberration remains. The microscope must therefore be carefully and correctly aligned to minimise this fifth order term.

The coefficients for the aberration are calculated using a tableau of diffractograms from an amorphous sample, through an extension of the method proposed by *Zemlin et al.* **[129]**. By analysing the digital diffractograms of images taken at various beam tilts the spherical aberration coefficients can be derived. From these coefficients, the currents required by the corrector lenses are calculated by software developed by Corrected Electron Optical Systems (CEOS). This process is repeated until the aberration coefficients are sufficiently low.

4.2.4. Scanning TEM (STEM) and its Application for Heusler Alloys.

Although initially developed in the 1930s, it was not until the late 1960s that Scanning Transmission Electron Microscopy (STEM) became widely used due to the development of field emission sources **[129]**. This is because of the increased current densities (10^6 A/m^2) over the conventional thermionic filaments. This high current density allows large signals to be collected from a thin specimen whilst maintaining an extremely small probe size.

The STEM varies from the conventional TEM in a number of ways, primarily the imaging mode. In the STEM the electron beam is focused to a small probe on the specimen and then raster scanned to collect the information for the image as opposed to parallel illumination of the entire imaged region. With this optical arrangement High Angle Annular Dark Field detectors (HAADF) can be used. HAADF detectors collect electrons scattered elastically from the specimen, the result of which is an image contrast formed from the atomic numbers of elements in the specimen (z-contrast). This technique is particularly useful for the structural analysis of Heusler alloys where the z-contrast allows direct analysis of atomic elements in the lattice **[35]**. A schematic of the STEM set up can be seen in Figure 4.8.

STEM can also be used in bright-field mode, where the signal is similar to those seen in conventional TEM. Both HAADF and bright field images taken with the JEOL JEM-2200FS can be seen in Figure 4.9a. The contrast difference is distinctive. In HAADF mode the elements of higher z scatter more electrons to higher angles and

therefore appear bright, the opposite of conventional TEM diffraction contrast. Conventional diffraction contrast is used to form the bright field image.

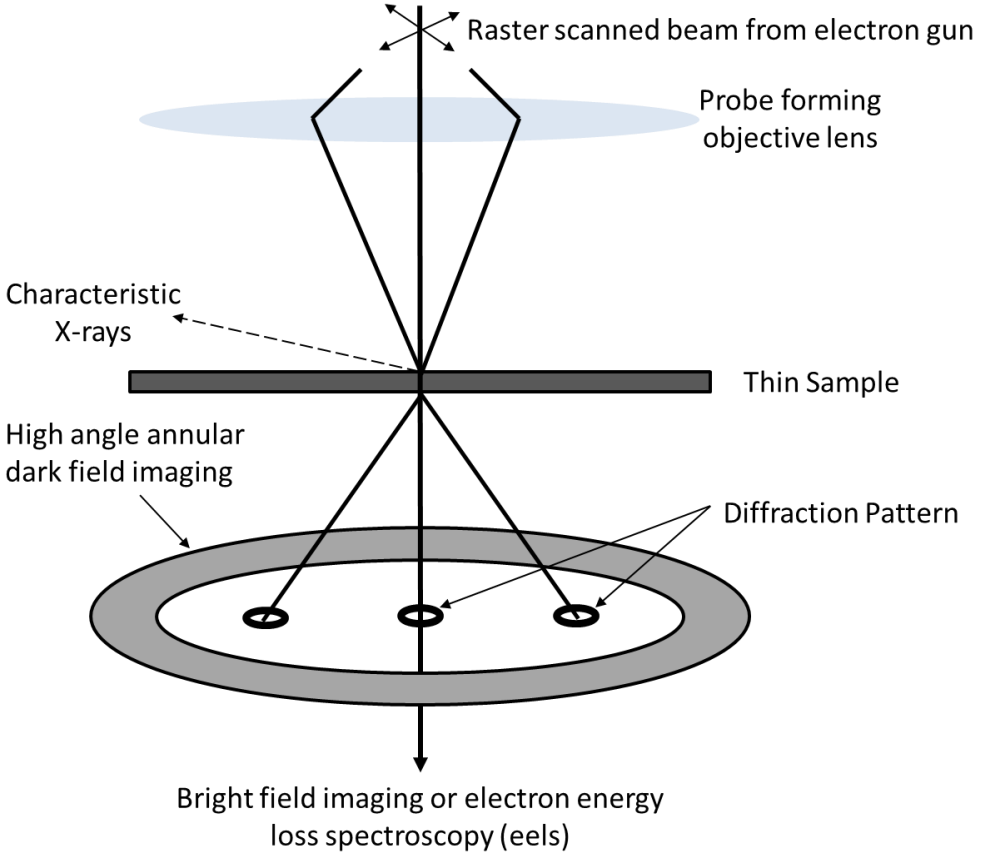

Figure 4.8. Schematic diagram of STEM probe and specimen with resulting interactions **[127]**.

Figure 4.9b shows a high resolution HAADF STEM image of an area of $L2_1$ ordered Co_2FeSi. The ordering in this area of film can be inferred directly from the intensities in the image. The atomic columns of Co have the greatest intensity due to having the highest atomic number as well as the entire column being composed of Co atoms. The Fe and Si sites however show reduced intensity, due to the change in atomic number and the variation of atoms in the atomic column. The intensity profile in the figure shows the intensity variations between atomic columns. Apart from small variations in the intensity across the profile due to film thickness or probe scanning effects it is shown that Co, Fe, and Si sites have specific associated intensities.

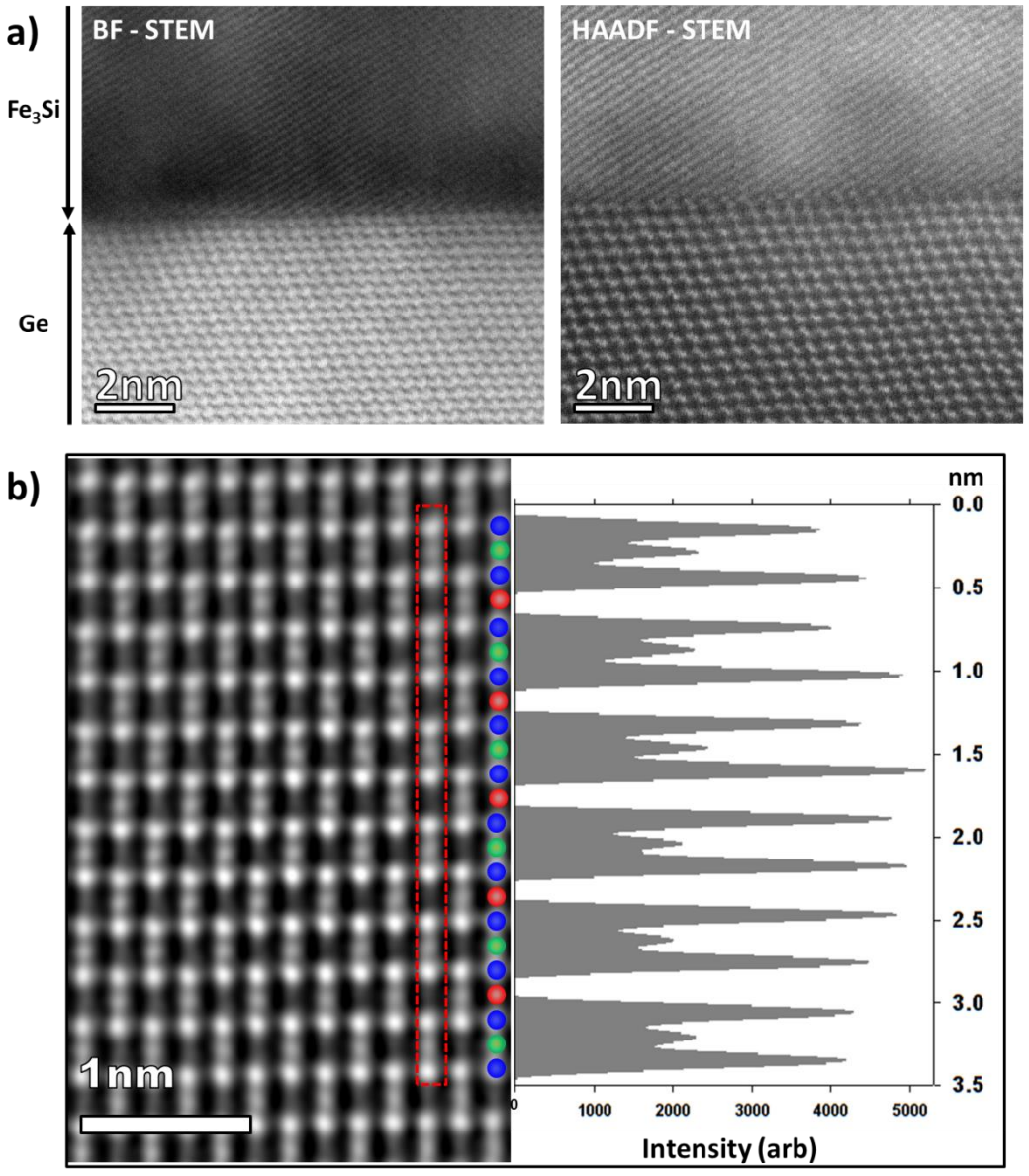

Figure 4.9. a) Bright field and HAADF STEM images of an Fe_3Si/Ge interface. b) Filtered high resolution HAADF STEM image of a Co_2FeSi film cross section. Intensity profile along the [001] plane shows z-contrast of atoms in the alloy. Atoms are highlighted for reference, Blue (Co), Green (Fe) and Red (Si).

Another advantage of using a focused probe for electron microscopy is high resolution elemental mapping through energy dispersive x-ray (EDX) spectroscopy. Using the rastered electron beam, elemental maps of entire regions or line scans through multilayer films can be acquired. The information from these is difficult to quantify. This difficulty arises for a number of reasons. One of the most prevalent is specimen drift during the measurement. The extremely long exposure times involved in these measurements also results in increased specimen damage and contamination.

4.2.5. X-Ray Diffraction and its Applications for Heusler Alloys

X-rays are diffracted by atomic planes in crystals to angles fulfilling the Bragg condition in much the same way electrons are. This can once again be used as a characterisation tool. The large advantage of X-rays over electrons is the ability to measure average lattice spacing over large samples. The X-ray diffraction (XRD) measurements taken in this study were carried out using a Rigaku SmartLab X-ray diffractometer. This system allows for a number of different X-ray sources and most importantly has a 3-axis goniometer allowing for many different X-ray measurements to be carried out. The goniometer, X-ray source and detectors have a minimum step size of 0.001° degrees allowing for extremely high resolution diffraction scans.

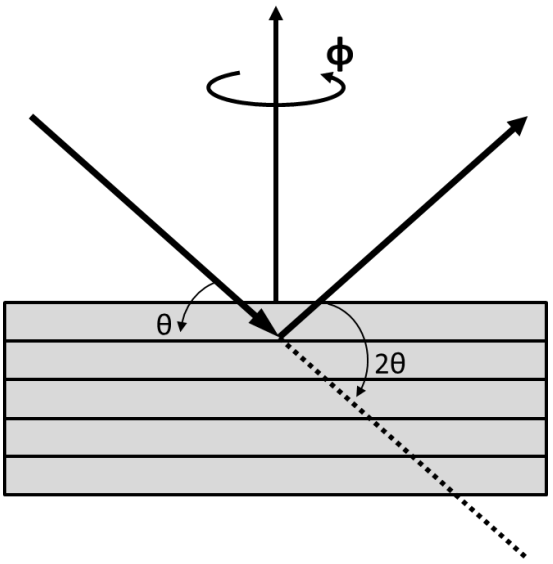

Figure 4.10. Schematic of geometries and associated angles for XRD measurements.

Two main types of scan have been carried out in this work, the typical $\theta/2\theta$ scan and the φ-scan. The geometries of these two angles with respect to the sample can be seen in Figure 4.10. In the $\theta/2\theta$ scan the detector moves twice the angle moved by the incident radiation source. This gives a scan of all the reflections from planes perpendicular to that of the substrate normal. The φ-scan however is somewhat more complicated to align. By aligning to a specific lattice plane out of the plane of the film reflections can be collected from a 360° rotation of the sample. For Heusler alloys this can be particularly useful as reflections from the (111) planes are only allowed for the $L2_1$ structure, therefore its presence can easily be determined.

The full width half maximum (FWHM) of a peak can be used to estimate the crystallite size within a film using the Scherrer relationship, equation 4.6.

$$D_{\mathrm{XRD}} = \frac{\lambda_x}{\beta cos\theta_B} \tag{4.6}$$

where D_{XRD} is the crystallite size , λ_x is the wavelength of the incident X-ray radiation, β is the FWHM and θ_B is the Bragg angle of the peak **[130]**. This is used in this work to estimate the size of $L2_1$ ordered regions in films. It should be noted however that for large particles this equation will provide an underestimate. This is due to the effect of lattice strain on the diffraction patterns for these particles.

Chapter 5. Magnetic Characterisation

5.1. The Alternating Gradient Force Magnetometer (AGFM)

5.1.1. Background

As the amount of material in thin film magnetic devices becomes ever smaller the requirement for highly sensitive instruments capable of measuring the magnetisation reversal in these systems in an accurate and reproducible manner increases. One of the most sensitive instruments available without the need for cryogens is the alternating gradient force magnetometer (AGFM), with a noise base as low as $2x10^{-8}$ emu in air and lower (10^{-11} emu) under vacuum conditions **[131-133]** . The AGFM can trace its origin to the vibrating reed magnetometer initially proposed as a device to measure the magnetisation reversal of single particles of hard magnetic materials **[134]**.

This type of magnetometer operates by attaching a sample to a fine wire or reed. The reed is then suspended in an inhomogeneous magnetic field and the deflection of the reed is measured. The deflection of the reed in the field is used to determine the force exerted on the sample (via equation 5.1) and as a result, the magnetic moment. The sensitivity of the device can be increased through the use of an alternating magnetic field to hold the reed and sample assembly at mechanical resonance. Zijlstra's initial design used a synchronised stroboscopic lamp and microscope to measure the sample deflection **[134]**.

From 1980, higher sensitivity vibrating reed magnetometers were developed through the advent of piezoelectric materials **[133,135]**. The first commercial AGFM became available in 1989 through Princeton Measurements Corporation (PMC). A PMC Micromag model 2900 has been used for measurements of magnetisation

reversal of continuous thin film samples in this work. The AGFM is a force based instrument. The AGFM arrangement of the PMC system is shown schematically in Figure 5.1.

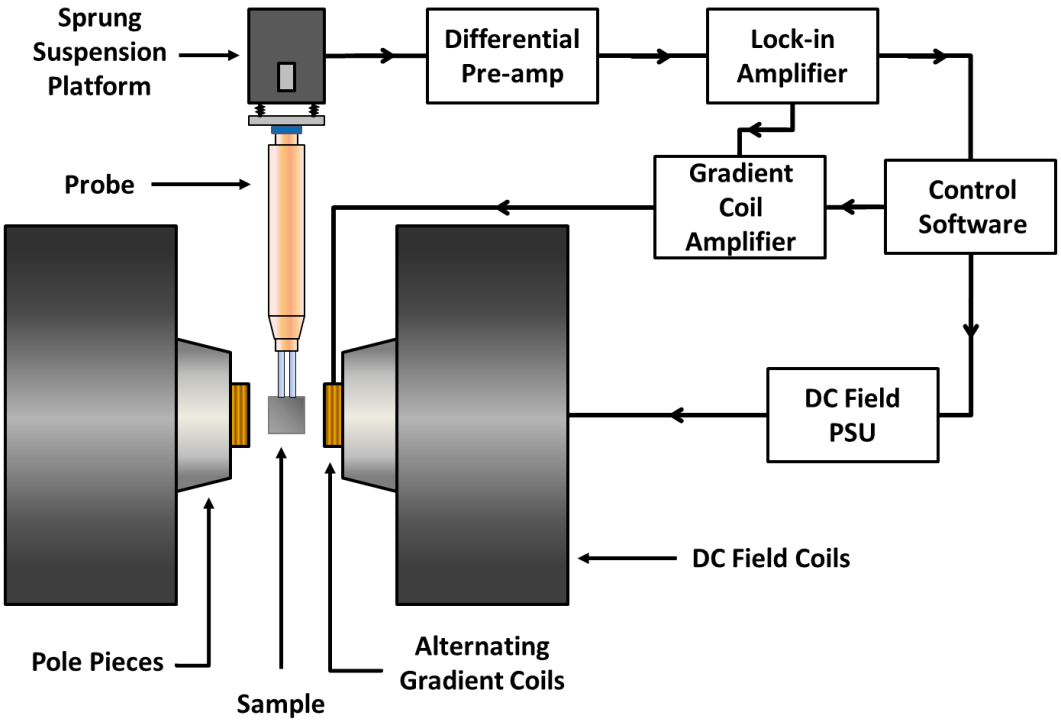

Figure 5.1. Schematic diagram of a typical AGFM.

The alternating gradient field produced by the small coils attached to the pole pieces induces small deflections (~nm) in the sample and as a result a stress upon the sample mounting assembly. This assembly is in turn attached to a silver-coated lead-zirconate-titanate (PZT) piezoelectric bimorph. This bimorph converts the stress exerted on it by the sample deflection into a measurable voltage. The force exerted on the sample by the gradient field is given by:

$$F_i = \mu_i \left(\frac{dH_i}{di}\right), \qquad (5.1)$$

where i is an arbitrary direction along which all components of the equations are measured (i= x, y, z) and μ_i and ($\mathrm{d}H/\mathrm{d}i$) are the magnetic moment and field gradient measured along i respectively. As previously discussed, the sensitivity of the AGFM can be maximised by operating at the mechanical resonance of the sample mounting assembly. This mounting assembly consists of two tubular quartz legs, roughly 25 mm

long with 0.4 mm outer diameter, attached to a quartz glass plate of similar size to the sample. Equation 5.2 gives the resonant frequency (υ_{res})

$$\upsilon_{\mathrm{res}} = \frac{1}{2\pi}\frac{w}{l^2}\left(\frac{Y}{\rho}\right)^{1/2}. \qquad (5.2)$$

Where the variables refer to the dimensions and properties of the quartz legs and mounting plate, the width *w*, the length *l* and density ρ and Young's modulus *Y*. Operating at υ_{res} should give a high mechanical Q-factor (25-250) **[131]**, although the Q-factors of probes used in this work varied between 25 and 74. A measurement of the noise base of a typical probe is shown in Figure 5.2. The standard deviation in 1000 measurements of a moment of $3.56\text{x}10^{-4}$ emu over 100 seconds is $1\text{x}10^{-6}$ emu whilst using a field gradient of 0.4 Oe/mm. The noise base is somewhat higher than that previously quoted from the reference**[132]**. This is due to the use of a much smaller field gradient, 0.4 Oe/mm instead of 4 Oe/mm, resulting in smaller deflections of the probe. The resonant frequency of the combined assembly and sample is determined before taking measurements by sweeping the gradient field through a frequency range, typically 100-1000 Hz, and measuring the output voltage, which peaks at υ_{res}.

Once υ_{res} has been determined the magnetic properties of the sample can be measured. A wide range of magnetic measurements can be performed with this instrument, most commonly hysteresis loops, DC demagnetised (DCD) and isothermal remanence curves (IRM) as well as measurements of magnetic time dependence. The PMC Micromag model 2900 AGFM is equipped with a water-cooled low impedance electromagnet, producing a maximum field of 24 kOe at a pole spacing of 10 mm with a high sweep rate. The typical measurement time for a simple symmetric hysteresis loop between ±5 kOe is 90 seconds. It is also possible to adapt the system for use with a continuous-flow cryostat allowing measurement at temperatures between 4 and 300K although this is known to raise the noise base of the system to 2×10^{-5} emu with a field gradient of 4 Oe/mm at 5 K **[132]**.

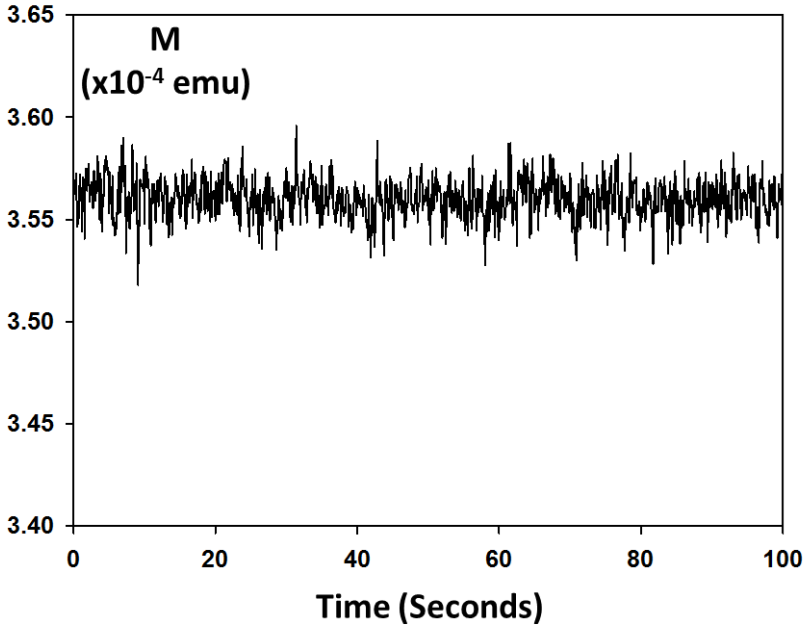

Figure 5.2. Noise base measurement of a typical AGFM probe loaded with a 5 mm x 5 mm Si substrate and 20 nm thick Co_2FeSi film at an alternating field gradient of 0.4 Oe/mm.

5.1.2. The Effect of Gradient Coils

One extremely important parameter to consider when taking magnetic measurements with the AGFM is the effect of the field gradient. For the system used in this work there are three selectable field gradients: 4, 0.4 and 0.04 Oe/mm. At the centre of the gradient field the net AC field is zero, so there is no effect upon the magnetic properties, but at positions away from this point the field gradient can affect the measurement. This effect is particularly prevalent for measurements taken with the field in the plane of the sample, where the lateral dimensions of the sample are typically of the order of 5 mm. The AC field will induce an incremental fluctuating field at the sample edges, thus increasing the effective field applied to the sample through the combination of AC and DC fields. For example, a typical square sample with sides of length 5 mm will feel an extra AC field of 10 Oe at the sample edges when measured with a field gradient of 4 Oe/mm. This effect becomes of great concern when measuring samples with extremely low coercivities like a number of those studied in this work. It has been shown that by careful selection of the field gradients the effect of this induced field on the magnetic properties of a sample can be minimised **[132]**.

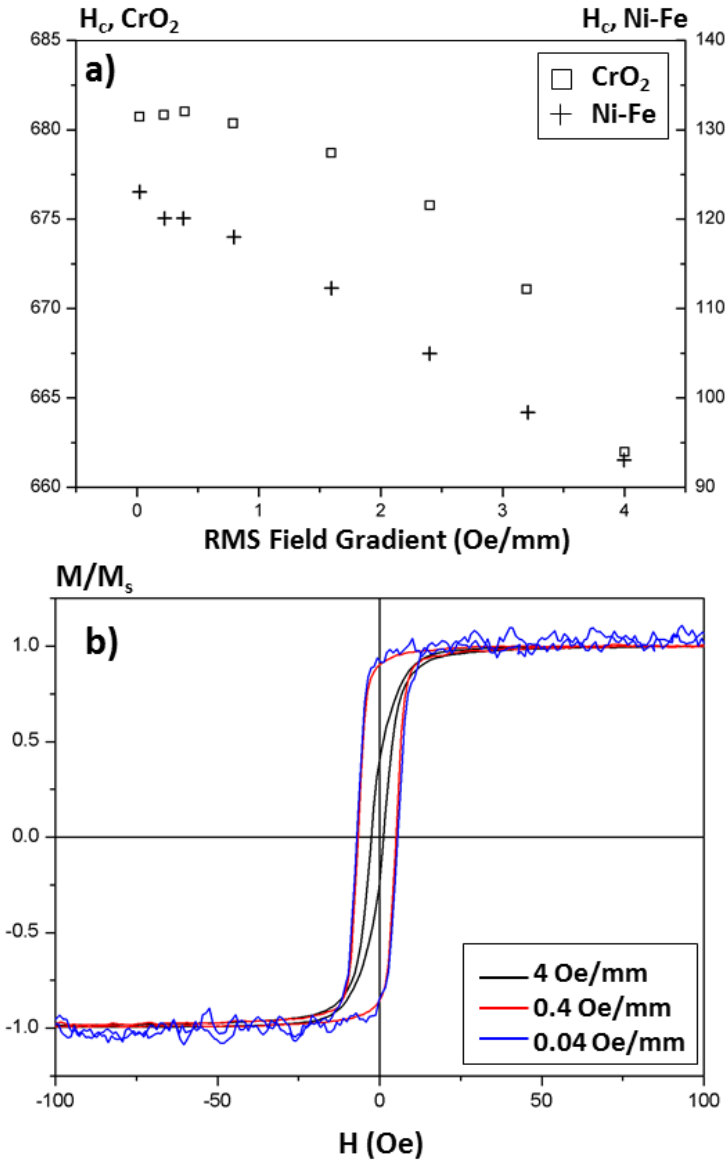

Figure 5.3. a) The effect of the AC field gradient on coercivity **[132]**. b) Hysteresis loops for Co_2FeSi polycrystalline thin films deposited on 6 nm Ag seed layer taken at alternating field gradients of 4 Oe/mm, 0.4 Oe/mm and 0.04 Oe/mm.

Figure 5.3a shows how large an effect the gradient field can have on the measured coercivity of samples with H_c of 100 Oe or greater. A reduction of 20 Oe in a 4 Oe/mm gradient is typical. This effect is amplified even further for a number of the Co_2FeSi films measured in this work where the typical coercivity when measured is ~40 Oe. This value has been verified using a VSM where the demagnetising effect of the gradient field is not an issue. Such large reductions in H_c as those seen in Figure 5.3 are at first difficult to understand. One would expect a reduction no greater than

10 Oe due to the demagnetising effect of the AC field at the sample extremities, as opposed to 20 Oe or more seen in the figure. However, the alternating field couples not to H_c directly but to the fluctuation field (H_f) resulting from the effect of thermal energy. This creates a much larger effect than would be expected.

The effect on the hysteresis loops for three different gradients is shown clearly in Figure 5.3b. The 4 Oe/mm loop is completely different to those measured at 0.4 Oe/mm or 0.04 Oe/mm, with a much reduced remanence and coercivity. The difference between 0.4 Oe/mm and 0.04 Oe/mm is less remarkable although the loop taken with an AC field gradient 0.04 Oe/mm shows much more noise in the measurement of saturation moment (M_S). This is due to the smaller deflections of the sample resulting from the much smaller gradient field. Therefore, in order to minimise the gradient coil effect, all measurements of samples with H_c of up to 500 Oe in this work have been measured using a field gradient of 0.4 Oe/mm.

5.1.3. AGFM Measurement Techniques

The most common measurement carried out on magnetic systems is the hysteresis loop. This measurement gives a large amount of information about the magnetic structure of a sample. It cannot however give you the complete picture of the magnetic properties of a sample as it contains information about the reversible and irreversible contributions to the magnetisation reversal simultaneously.

Both the single crystal and polycrystalline thin films measured in this work exhibit extremely complex hysteresis loops as a result of a number of co-existing reversal mechanisms. The presence of different reversal mechanisms in these films is often highlighted through variations in gradient of the curve in different regions of the hysteresis loop. Another important point on the hysteresis loop for spintronic device applications is the remanent magnetisation, M_r, often represented through a normalisation to M_s, M_r/M_s, which is known as the squareness. A value close to 1 is desirable for spintronic devices where it is important to have all spins in the same state at zero field, such as the free layer in magnetoresistive sensors. Whilst the coercivity, H_c, is often quoted as a defining parameter for magnetic materials it only really represents the limits on an integral for a point on the loop where reversible and irreversible components of M combine to give M=0, i.e.

$$\int_0^{\Delta E_c} g(H) f(\Delta E)\, d\Delta E + \int_{\Delta E_c}^{\Delta E_{H_c}} f(\Delta E)\, d\Delta E = \int_{\Delta E_{H_c}}^{\infty} f(\Delta E)\, d\Delta E, \qquad (5.2)$$

where $g(H)$ is the Langevin function describing the reversible component, $f(\Delta E)$ is the distribution of energy barriers in the system and ΔE_c is the critical energy barrier that is undergoing thermal activation at the measurement time.

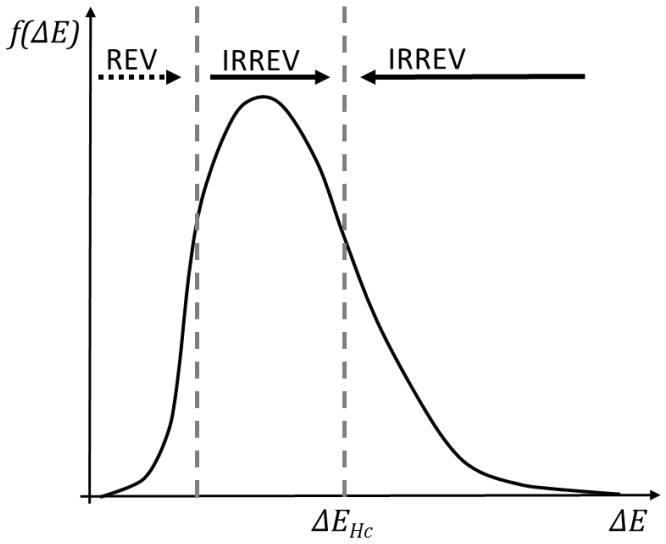

Figure 5.4. Coercivity of a magnetic system described through a distribution of energy barriers.

This expansion of integrals in equation 5.2 describes the coercive mechanism through a distribution of energy barriers shown schematically in Figure 5.4. The coercivity is the point where the volume of reversible and irreversible energy barriers in one magnetisation direction balances the irreversible component in the opposite direction resulting in a net magnetisation of zero. The reversible component can be due to thermal energy or misalignment of the easy axes which gives the dependence of H_c on measurement parameters. As a result, it is often more important to measure the irreversible components of the magnetisation, which can be achieved through measurements of remanence curves.

Measurements of M_r provide an important understanding of a number of properties of magnetic thin films, through which it is possible to determine both the reversible and irreversible components of the magnetisation. These measurements are one route to determine H_f and as a result the magnetic activation volume (section 2.5). Remanence can be measured either by taking the system from an initially demagnetised state to positive saturation in an isothermal remanence (IRM) curve, or from positive saturation to negative saturation known as a DC demagnetisation (DCD)

curve. Both curves are shown schematically in Figure 5.5. The differential of the DCD curve is known as the irreversible susceptibility (χ_{irr}) and once normalised gives a measure of the switching field distribution in a specimen **[136]**.

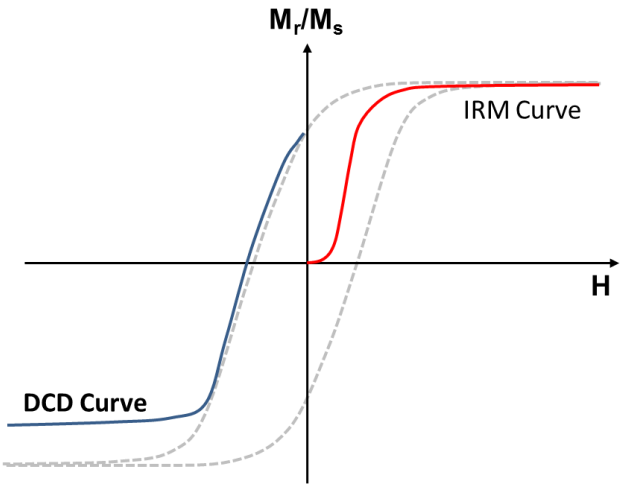

Figure 5.5. Schematic diagram of DC demagnetised (DCD) remanence and isothermal remanence (IRM) curves in the context of the hysteresis loop.

To remove the noise from the DCD curves and IRM curves a 5 point sliding quadratic fit is used. Initially developed by *Mayo* and *O'Grady,* this samples the first 5 points of a curve and fits a quadratic. The midpoint of the quadratic is taken and the first point of the curve removed and the 6th point added. By this mechanism the quadratic slides along the curve. A quadratic is found to be optimum as any fit with an order higher than 2 has two turning points which allow noisy points to be followed. The quadratic can also be positive or negative so sigmoidal curves such as hysteresis loops can be followed with great accuracy. These techniques have been widely used in the characterisation of magnetic recording media but have found limited applicability in the characterisation of spintronic devices **[137]**.

These measurements can be combined with measurements of magnetic time dependence to give an estimation of the activation volume previously discussed in section 2.5. In the time dependence measurement, a magnetic sample is first saturated in positive field (H) typically 15 kOe. The field is then reduced to zero and a small reverse field (H) is applied. The magnetisation is then left to decay for 600 seconds at the reverse field. After 600 seconds, the saturating field is applied again and a slightly larger reverse field applied. The magnetisation decay is again measured. This is

repeated through the entire reversal curve of the hysteresis loop from remanence to negative saturation. The result of this is a series of decay curves at different values of reverse field such as those shown in Figure 5.6. It is shown that in this case $M \propto \ln(t)$.

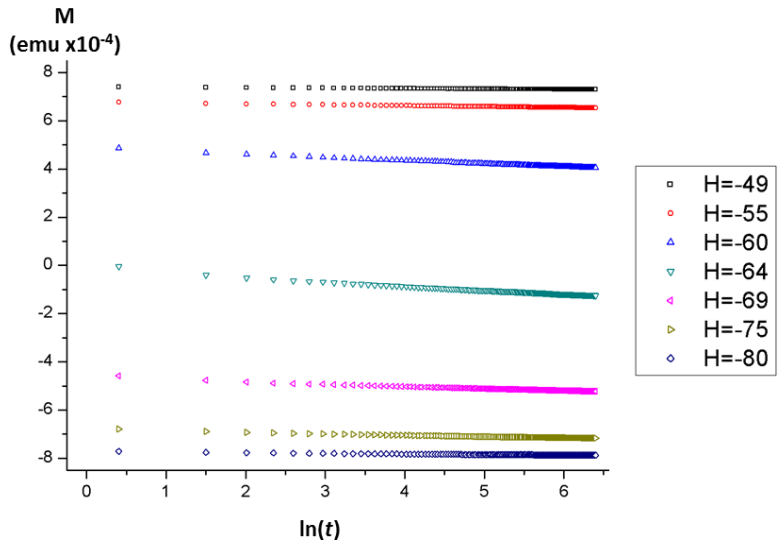

Figure 5.6. Time dependence curves taken every 5 Oe showing variation of *M* with ln(time) for polycrystalline Co_2FeSi film deposited at 800 V and annealed at 500°C for 6 hours.

$$M(t) = M(0) \mp S(H)\ln(t) \tag{5.3}$$

Plotting the decay curves versus $\ln(t)$ allows access to the magnetic viscosity coefficients, $S(H)$, needed for the estimation of the activation volume. In some magnetic systems however the simple linear case may not be applied. $S(H)$ is intrinsically linked to the energy barrier distribution. For systems with a very narrow energy barrier distribution variation of M with $\ln(t)$ becomes non-linear. In these situations the decay of M is more accurately described by the series expansion of equation 5.3 **[138]**.

$$M(t) = M(0) \pm S_1(H)\ln(t) \mp S_2(H)[\ln(t)]^2 \pm \cdots \tag{5.4}$$

From the values of $S(H)$ and the irreversible susceptibility it is possible to find an estimation for H_f which is essential for any calculations of the activation volume (V_{act}). It is also possible to acquire a value of H_f directly from the magnetisation decay curves using the waiting time method **[75]**. With a series of magnetisation decay

curves closely spaced in H it is possible to select a point of constant magnetisation which has a number of intercepts from which H_f can be determined **[77]**.

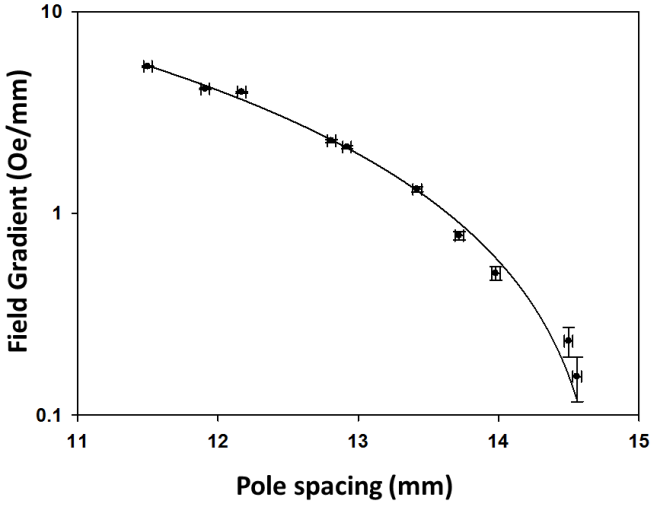

Figure 5.7. The effect of pole piece separation on the AC-gradient field in the PMC micromag 2100 AGFM.

Unfortunately, for samples with extremely low coercivities like the epitaxial films measured in this work, it is impossible to acquire decay curves with sufficient resolution to perform a waiting time measurement (or even a high resolution calculation of H_f using the $S(H)$ and χ_{irr} method). This is due to the limit of controllability of the DC field from the AGFM. It is possible to improve this resolution by separating the pole pieces of the magnet so that each incremental current step produces a smaller step in field. However, this also results in a reduction of the gradient field from the calibrated 4 Oe/mm at 11 mm spacing.

The effect of pole spacing on AC field magnitude was then measured. A 620 turn coil was fixed between the pole pieces and connected to a digital oscilloscope through a lock-in amplifier. A sine wave from a signal generator was used as the reference with a frequency set to the operating frequency of the AGFM probes used for measurements. The peak-peak (p-p) voltage induced in the coil could then be measured to high accuracy. By using the initial PMC calibration this p-p voltage could be converted to a field gradient value in Oe/mm. The effect of pole spacing on the gradient field can be seen in Figure 5.7, where the field gradient drops off as the square of the pole piece separation. To maintain reproducibility of the measurements the spacing was set so that the relative gradient 1 setting in the AGFM software now

gave a signal equivalent to that received for the relative gradient 0.1 setting at 11mm pole spacing.

5.2. Vibrating Sample Magnetometer (VSM)

The vibrating sample magnetometer was initially proposed by *Foner* **[139]**. In the standard arrangement, a sample is attached to one end of a fixed rod and oscillated between pick-up coils situated in the gap of the pole pieces of an electromagnet as schematically shown in Figure 5.8. In the ADE model 10 VSM used in this study the maximum DC field from the electromagnet is 20 kOe with a pole piece spacing of 40 mm.

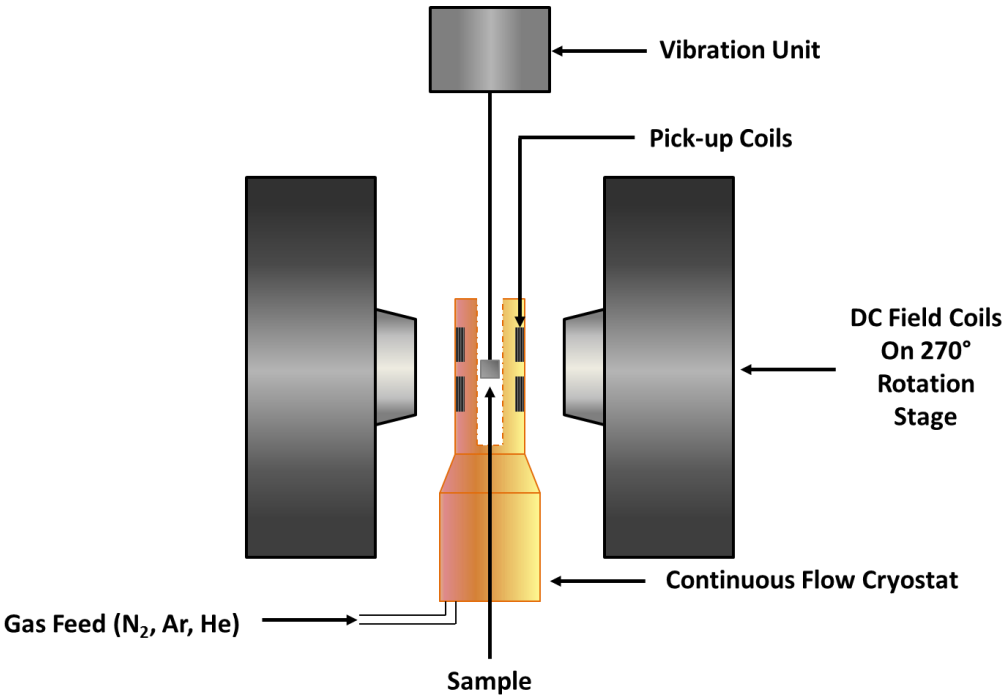

Figure 5.8. Schematic diagram of ADE model 10 VSM.

The motion of the magnetised sample causes a change in the flux through the pick-up coils, thereby inducing an electromotive force (e.m.f.) in the coils via Faraday's law equation 5.5. The e.m.f. is proportional to the magnetic moment of the sample (m). The pick-up coils are arranged in the optimum configuration outlined by *Mallinson* **[140]**.

$$e.m.f. = -N\left(\frac{d\varphi}{dt}\right) \propto m, \tag{5.5}$$

where N is the number of turns in the pickup coils and $d\varphi/dt$ is the rate of change of the flux in the coil. The voltage induced is measured using a lock-in amplifier.

The advantage of the VSM over the AGFM is the lack of the gradient field, thus removing the demagnetising effect and allowing for more precise measurements of the coercivity in magnetically soft materials. The ADE model 10 also has a number of other significant advantages over the AGFM, predominantly the ability to work at a range of temperatures. In the ADE model 10 the pick-up coils are mounted inside a continuous flow cryostat, which allows measurements to be made between 100K and 770K with a temperature stability of ±1K over 60 minutes. The other large advantage is the ability to rotate the DC field coils through 270° about the sample centre, allowing for directional dependent measurements of the magnetic moments. To aid this ability two different sample rod designs are available, the 'steering wheel' where the sample plane is fixed perpendicular to the vibration direction and the 'lollipop' where the sample plane is fixed parallel to the vibration direction. These allow for the magnetic properties of the sample to be probed 270° around the plane of the sample, and 180° out of the plane of the sample. The ability to probe the magnetic properties around the plane of the sample is particularly useful for measurement of the easy axis in single crystal films like the ones measured in this thesis.

Chapter 6. The Effect of Structure on Magnetisation Reversal

The structure of magnetic thin films has long been known to have a significant effect on magnetisation reversal **[47]**. The volumes of the particles within a film, as well as any defects within those particles, all control the magnetisation reversal of the film. Reversal is dominated by the exchange interaction between neighbouring spins, any local structural anomalies can have a profound effect on the reversal process. This can be in the form of domain wall pinning, reduced nucleation fields and even the point at which particles begin to exhibit single domain behaviour. It is important to understand how changes in the structure of Heusler alloy thin films affect the magnetic reversal characteristics. Whether that is the change from polycrystalline to epitaxial films, the differences between $L2_1$ and $B2$ ordering or the appearance of defects in the crystal structure. A wide range of structural and magnetic characterisation has been carried out on epitaxially sputtered and polycrystalline thin films, sputtered using the HiTUS system, to compare the differences in magnetisation reversal in the context of their different structures.

6.1. Film Growth and Sample Preparation

Magnetic and structural characterisation has been carried out on Co_2FeSi thin films deposited via HiTUS and UHV magnetron sputtering. 20 nm thick Co_2FeSi films were deposited and capped with a 3 nm thick Ta layer. HiTUS sputtered samples were deposited onto both Si and MgO substrates as well as carbon coated Cu and SiN TEM grids. The magnetron sputtered films were deposited onto MgO (001) substrates at an average deposition rate of 0.3 Å/s. Before the Heusler layer deposition the MgO(001) substrates were annealed for 30 minutes at 800°C to out-gas. A 10 nm MgO buffer layer was deposited using e-beam evaporation to improve surface roughness. Magnetron sputtered films were post-deposition annealed for 1 hour under vacuum of

$5x10^{-5}$ Pa at temperatures of 500°C and 600°C. This allows recrystallisation of the film from the as-deposited state, which is predominantly $B2$ ordered, to a state with increased $L2_1$ ordering. Samples grown using the HiTUS system were post-deposition annealed at 500°C in an Ar atmosphere. Specimens were annealed for increasing periods of time from 1 hour to 9 hours. This allows crystallisation of grains from the as-deposited matrix. The films deposited onto SiN TEM grids have been annealed inside the JEOL JEM-2200FS to observe the grain crystallisation and development process.

6.2. Structural Characterisation

6.2.1. Polycrystalline Films

6.2.1.1. In-Situ Observation of Grain Formation

After deposition using the HiTUS system, the films were annealed in the HRTEM to facilitate the growth of Co_2FeSi grains from the nano-crystalline matrix. To characterise the as-deposited matrix, TEM images were taken at a magnification of $x10^6$. These images were then Fourier transformed to form the digital diffractograms which are shown in Figure 6.1. The images show crystalline diffraction spots with increasing intensity within the disk associated with an amorphous film. Although these spots are present in the sample deposited with a DC bias (V_B) of 500 V, their intensity and number are shown to increase in the diffractograms of the films deposited using a higher bias of 750 V and 990 V. This is evidence that the crystallographic ordering in the as-deposited matrix increases with sputtering bias voltage (V_B). It also suggests that the initial crystallites in the matrix are larger when samples are grown at higher V_B. Electron dispersive X-ray spectroscopy (EDX) was used to analyse the elemental composition of the as deposited matrix. The EDX spectra show no significant variation in elemental composition of the matrix with V_B, thus the increased intensity of diffraction spots is purely due to the variation in film structure and initial crystallite size induced by V_B.

V_B alters the initial state of the film indirectly. The voltage applied to the target during sputtering accelerates the Ar^+ ions towards the target. Higher V_B therefore leads to higher ion velocity at the target surface. This higher velocity means that the material sputtered from the target has an increased initial energy. Because of this the adatoms of material sputtered at higher V_B will have an increased energy and

therefore mobility upon reaching the substrate. The increased mobility results in more of the deposited atoms forming energetically favourable ordered structures within the film. The result of this is an increased size and number of crystallites in the as-deposited film as shown in Figure 6.1.

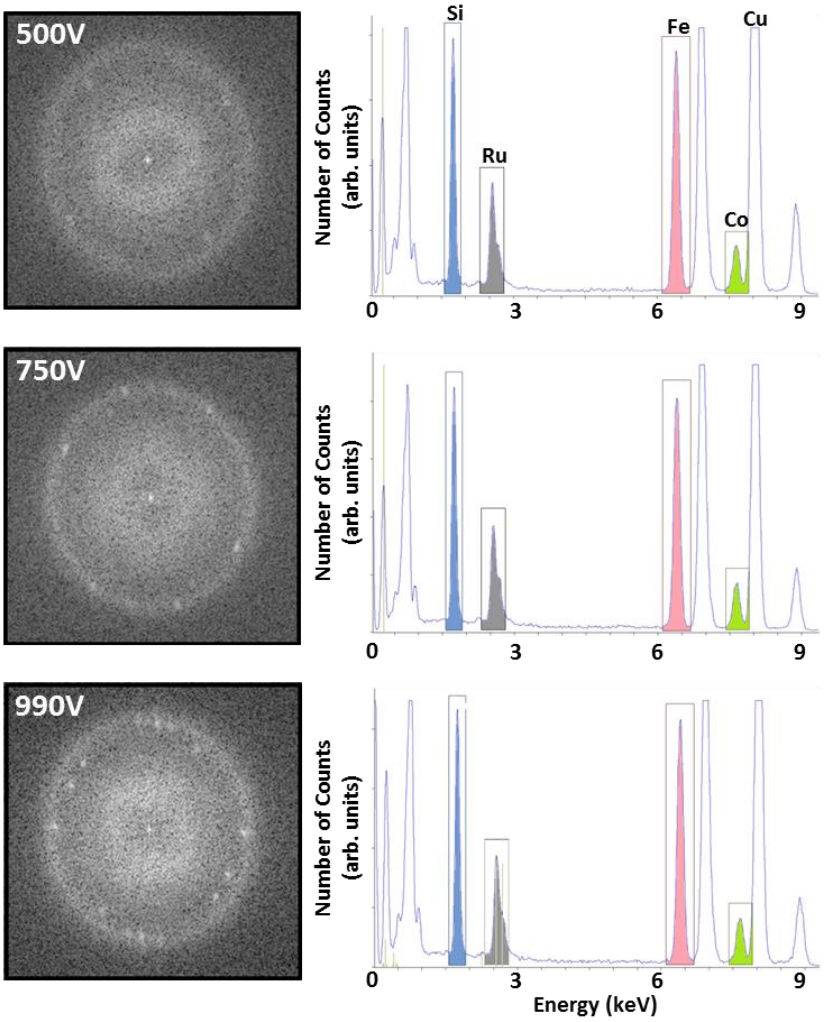

Figure 6.1. Digital diffractograms from HRTEM images as well as EDX spectra for as-deposited Co_2FeSi thin films with DC bias voltages of 500V, 750V and 990V.

To observe the crystallisation process induced by annealing, HRTEM with an in-situ heating stage was used. Initial crystallisation occurs above 235°C with further grain growth occurring after continued heating either at 235°C or higher temperatures. Figure 6.2a shows the process of crystallisation whilst holding the specimen at 235°C for 3 hours. It is worth noting that this experiment was carried out with the sample continuously exposed to the electron beam during heating. However the experiment was repeated with the beam isolation valve only opened

intermittently to image the specimen. The grain development process was found to be the same in both experiments showing that the electron beam has no observable effect on the crystallisation or grain growth processes. The crystallisation of the Co_2FeSi film was imaged from an initial amorphous matrix to 75% - 80% crystallised film at 180 minutes.

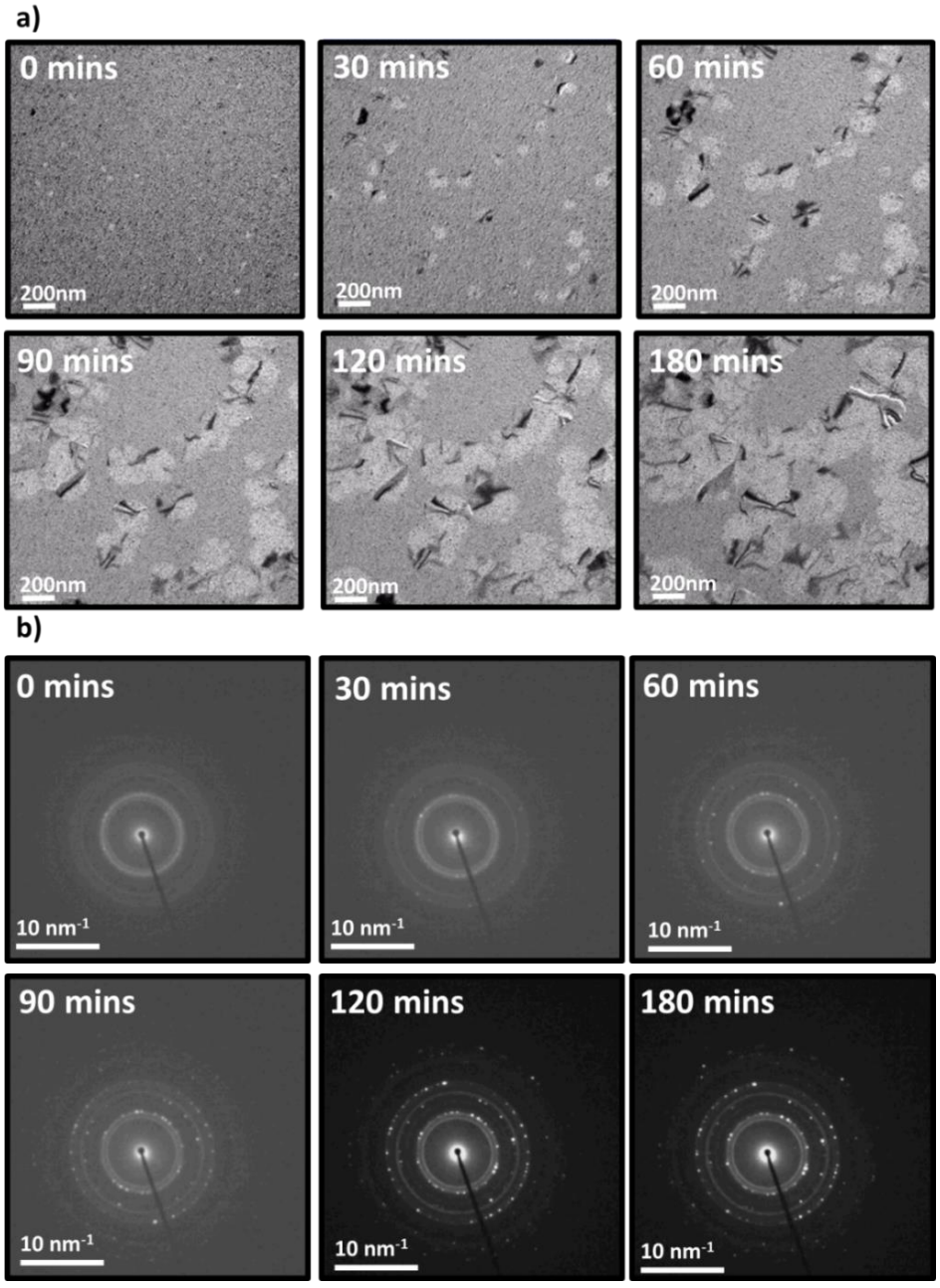

Figure 6.2. a) Montage of bright field TEM images showing Co_2FeSi grain growth at 235°C for up to 3 hours. b) The corresponding montage of SAED patterns.

The grains in the film are easily visible due to the large contrast change between the amorphous matrix and the crystallised region, as seen in Figure 6.2. After an hour of heating, fringes of contrast within the grains themselves also appear. There are two likely causes for this contrast variation. The first is re-crystallisation within the grains. This warps the atomic planes affecting the diffraction contrast. The second possibility is 3 dimensional growth of the grains leading to changes in height from region to region within the grains. This results in changes of the defocus value and as a result the contrast across the grains. The same experiment has also been carried out with the TEM in diffraction mode allowing observation of the crystallisation through change in the diffraction pattern, Figure 6.2b.

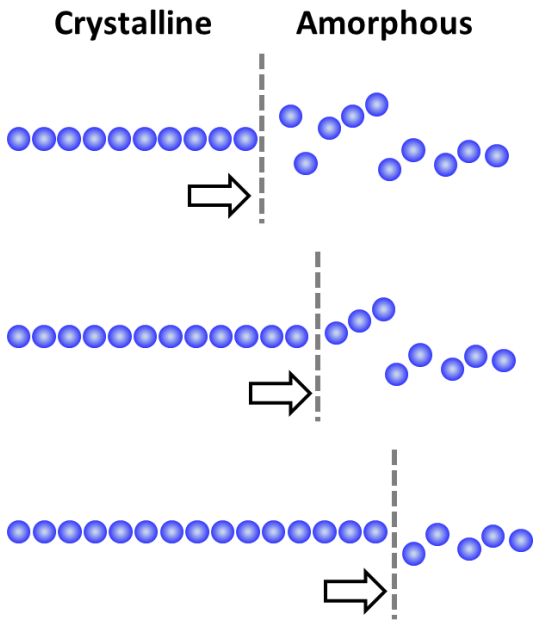

Figure 6.3. Schematic diagram illustrating the crystallite growth process in HiTUS sputtered Co_2FeSi thin films **[141]**.

A similar crystal growth mechanism has been observed for $Ni_{80}P_{20}$ alloys **[141]**, where a few extremely small regions within the homogenous matrix display a heterogeneous structure and act as a scaffold for the development of larger crystals. The crystals develop as shown in Figure 6.3, where the crystal front moves forward by two processes; either single atoms jumping from the amorphous matrix or already formed clusters depositing on the front of the crystal and assuming the crystalline orientation of the larger crystallite. With enough energy it is also possible to nucleate nanocrystals from a totally disordered matrix, although the energy required will be much greater. This crystallisation mechanism can be described using classical phase

transformation theory **[142]**, where the crystal growth velocity (v_{cg}) is described by an Arrhenius relationship, equation 6.1 **[143]**:

$$v_{cg} = a_0 v_0 \exp(-E_{act}/k_B T). \quad (6.1)$$

Where a_0 is the atomic radius, v_0 is the atomic jump frequency from the amorphous to the crystalline phase, E_{act} is the energy required for an atom to leave the amorphous phase and join the crystal and T is the temperature at which the crystallisation is taking place. However, for ternary alloys such as Co_2FeSi this simplistic relationship cannot be applied directly, as there are a large number of possible atomic jumps dependent on the atoms at the front of the crystal growth direction. For instance, a Co-Si jump will have a different E_{act} to a Co-Fe jump. These parameters should be intrinsic to the homogeneous as-deposited matrix for all Co_2FeSi films deposited using the HiTUS system. These parameters should also be independent of the deposition bias voltage. What will change depending upon the bias voltage is the initial film state, as the bias voltage applied to the target during deposition increases the energy of the deposited material. This will increase the initial crystallite density as well as the atomic intermixing in the films so that although the post nucleation growth rate should remain constant, the rate of initial grain nucleation will increase significantly with DC bias voltage.

To understand the change in the crystal structure of the film with annealing time, selected area electron diffraction was used whilst carrying out in-situ heating. It is clear from Figure 6.2b that as the specimen is held at 235°C, the diffraction patterns begin to change with the formation of distinct diffraction rings and spots as the annealing time increases. The diffraction spots are situated primarily on the diffraction rings corresponding to the [220] and [422] atomic planes of Co_2FeSi. This suggests that even when annealing at 235°C the films are $L2_1$ or possibly $B2$ ordered as these two superlattice reflections are allowed for both phases of ordering. The number of diffraction spots is also a measure of the number of grains in the film. The crystalline diffraction spots show that these grains are large. This gives further evidence for the nucleation and growth of grains in these films with annealing.

6.2.1.2. TEM for Grain Size Analysis

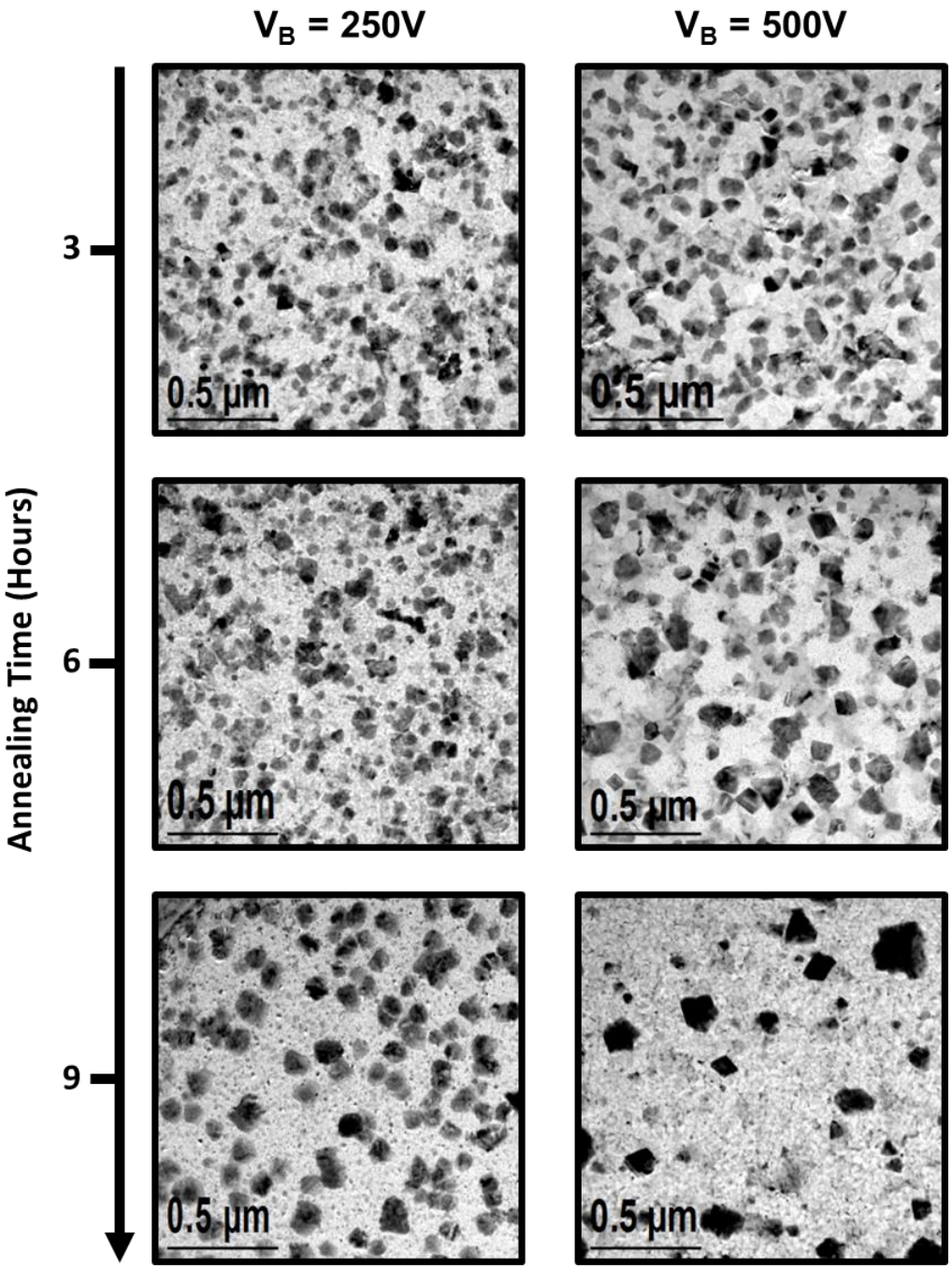

Figure 6.4. Montage of bright field TEM images showing change in film structure with V_B (left to right) and annealing time (top to bottom).

Post-deposition *ex-situ* annealed Co_2FeSi films were also imaged using the JEOL JEM-2011 TEM. From these images particle size analysis was carried out to measure the distribution of particle sizes within the film. This is particularly important because the size of grains in the film can have a profound effect on the magnetic properties

[47]. The films deposited onto the carbon coated Cu TEM grids were imaged after annealing at 500°C for 3, 6 and 9 hours. The change in the film structures with deposition bias voltage and annealing time can be seen in Figure 6.4. It is clearly observable, even without detailed analysis, that the films deposited at higher V_B have an increased average grain size. There is also a clear development of the grains with annealing time. These films do however look significantly different to those annealed *in-situ*. This is due to the difference in the annealing environment between the vacuum of the TEM and the Ar atmosphere, as well as the rates of heating. The annealing temperature was considered as the possible reason for this variation in film structure but further studies of *in-situ* films showed that annealing at 500°C still did not produce films similar to those shown in Figure 6.4.

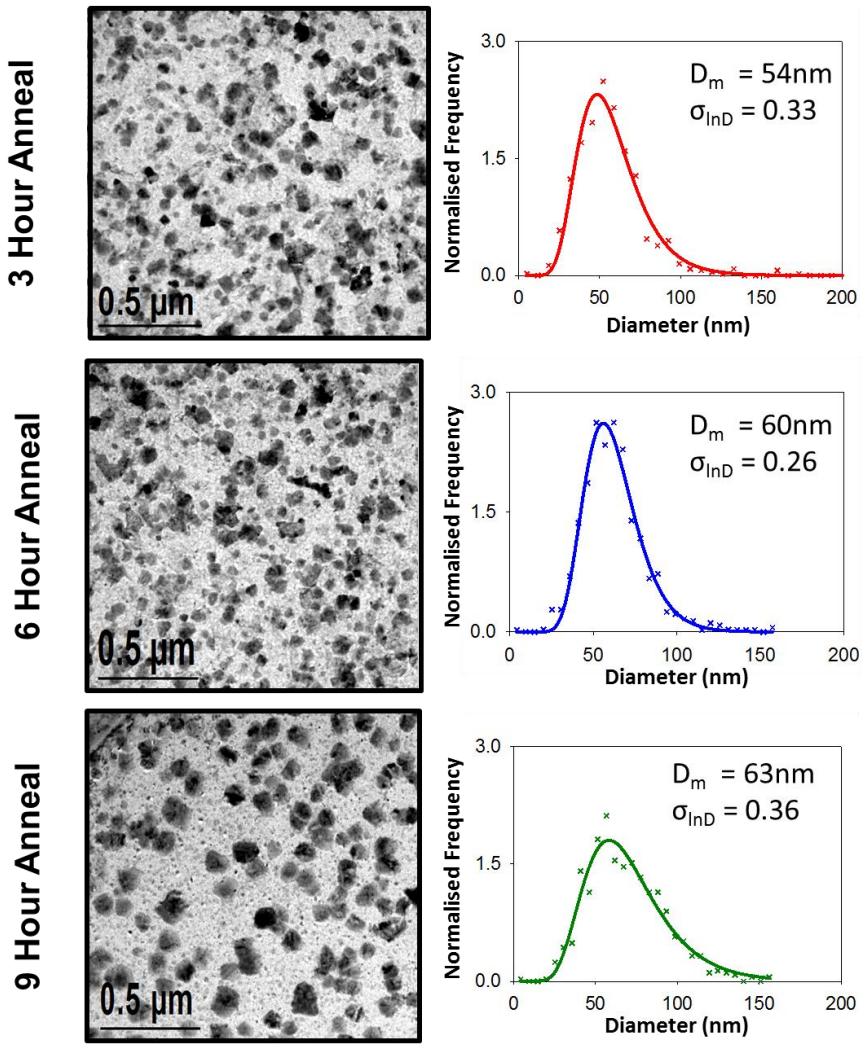

Figure 6.5. Grain size distributions and example TEM images for HiTUS deposited Co_2FeSi films with V_B=250 V.

It is immediately clear from the TEM images that the grain size of the Co_2FeSi is large when compared with typical films deposited using the HiTUS system **[121]**. The images were all taken at a magnification of x12k. This is an extremely low magnification for conventional TEM and a factor of 10 lower than that typically used to image films deposited using the HiTUS system **[122]**. This means that the grains have a diameter an order of magnitude larger, with grain sizes in the region of 40 nm – 200 nm. This immediately removes the majority of the grains from the single domain particle regime which has a profound effect on the magnetisation reversal of these films.

Figure 6.4 also shows a difference in how the films vary with annealing time. After 3 hours of annealing the films look similar but after 9 hours of annealing they are very different. For the sample grown with V_B = 500 V there are a small number of extremely large grains (~180 nm) which have most likely formed through coalescence of neighbouring grains. The grains in the sample grown at a bias voltage of 250 V however have a much greater number of grains with a smaller average diameter than those seen in the sample grown at V_B = 500 V. This is the result of the increase in the number of initial crystallites in the film deposited with V_B = 500 V. The initial crystallite density in this film is greater so neighbouring grains coalesce. In the film deposited with V_B = 250 V the initial crystallite density is lower so the grain are too sparsely distributed to coalesce.

Particle size analysis was performed on all the specimens. The diameters of over 800 grains were measured for each sample using an equivalent area method **[144]**. This was carried out using a Zeiss particle analyser, where a variable diameter light spot can be fitted to the approximate area of each grain. The diameter of the light spot is recorded as a voltage supplied to the bulb using a LabView VI routine. The distribution of particle diameters can then be fitted to a lognormal distribution function, described by equation 6.2, using the method outlined by *O'Grady* and *Bradbury* **[144]**.

$$f(D)dD = \frac{1}{\sqrt{2\pi}\sigma_{\ln D} D} \exp\left(\frac{-(ln(D) - \bar{x}_{\ln D})^2}{2\sigma_{lnD}^2}\right) dD, \qquad (6.2)$$

where D is the measured particle diameter, $\sigma_{\ln D}$ and $\bar{x}_{\ln D}$ are the standard deviation and the mean value of $\ln(D)$. The particle size analysis shows that the median particle diameter in the film deposited with V_B=250 V increases with annealing time. However

an unusual trend is seen in the standard deviation. The decrease in $\sigma_{\ln D}$ to 0.26 after annealing for 6 hours and subsequent increase to 0.36 after 9 hours is unusual. This can be explained by a two stage growth mechanism. Up to 6 hours, new particles are nucleating and previously nucleated particles are using material from the surrounding matrix of Co, Fe and Si to continue growth via the process outlined in section 6.2.1.1 **[143]**. After 6 hours the majority of the film is crystallised and any subsequent growth is facilitated by coalescence of neighbouring grains. This leads to the formation of some extremely large grains and a number of much smaller grains remaining from particles unable to coalesce. This would lead to an increased width of the distribution as shown in Figure 6.5. A summary of the particle size analysis for the films grown at different bias voltages is shown in Table 6.1.

Table 6.1. Summary of particle size analysis data for HiTUS deposited Co_2FeSi thin films.

V_B (V)	T_A (Hours)	D_m (± 1 nm)	$\sigma_{\ln D}$ (±0.05)
250	3	54	0.34
	6	60	0.26
	9	63	0.36
500	3	78	0.46
	6	75	0.32
	9	72	0.40
750	3	79	0.44
	6	84	0.35
	9	75	0.35

A general trend of increasing grain size with V_B is immediately observable, particularly for the films annealed for 6 hours. This confirms that the initial film deposition conditions have a larger effect on the final structure of the film than any annealing carried out, beyond that which facilitates the initial crystallisation of the as-deposited film. This is due to the mobility of the constituent elements to form the complex $L2_1$ phase. The data in Table 6.1 also shows that for the samples deposited at 750 V the grain size begins to decrease when the samples are annealed for 9 hours. In Co_2MnSi films created under similar conditions this has been explained as being due to Si segregation from the ordered grains **[123]**. It can however be seen that for the film deposited with V_B = 250 V, this trend is not followed. The grain size in these films is still much smaller than that for the films deposited with V_B=500 V and V_B = 750 V.

This suggests that the films deposited with V_B=250 V have still not achieved a maximum size or a degree of ordering after which Si segregation would take place.

6.2.1.3. HRTEM for Structural Characterisation

Whilst carrying out the TEM observation a number of grains were also selected for HRTEM imaging. High resolution imaging can give information about the crystal structure and planar orientation of individual grains. This is particularly interesting as the polycrystalline films can contain grains with crystallographic orientations that are inaccessible through epitaxial growth. Grains have been found with a number of different crystallographic orientations out of the plane of the film. Most prevalent are the [111], [112] and [101] projections. Possible layer by layer crystallisation mechanisms associated with the [112] projection have previously been described by Fleet *et al* **[124]**. However, in the films grown in this work the most common projection is [111], an example of which is shown in Figure 6.6a

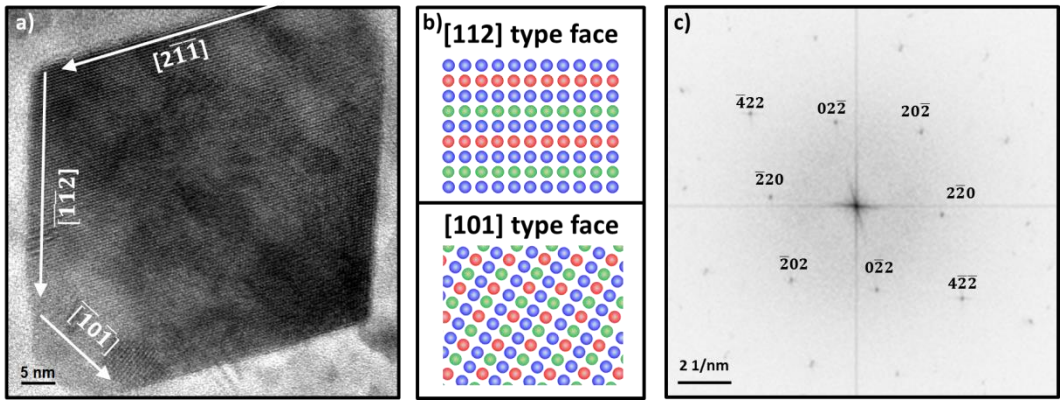

Figure 6.6. a) TEM image of a single Co_2FeSi grain. b) Schematic diagram of the [112] and [101] projections for Co_2FeSi (Co (Blue) Fe (Green) and Si (Red)) c) FFT of a single [111] oriented grain from a polycrystalline Co_2FeSi film.

The two faces of this crystal are shown schematically in Figure 6.6b. From this figure it can be seen how the layer by layer crystallisation results in a crystal consisting of stacked Co, Fe and Si atomic layers. This would also suggest that all observed grains formed through the same mechanism and the variation of observed projections is due to tilting of the grains in the film. Figure 6.6c shows the digital diffractogram (FFT) of the left hand image. From measurements of the spot spacing it has been found that the grain has a lattice constant of (5.6±0.1) Å, which is within error of the bulk lattice constant of $L2_1$ ordered Co_2FeSi, which is reported to be 5.64 Å **[60]**. The appearance of (111) diffraction spots in the FFTs gives more evidence for

the grains in the film being $L2_1$ ordered as these spots are known to diminish for disordered phases of Co_2FeSi **[145]**.

6.2.2. Epitaxially Sputtered Films

6.2.2.1. X-ray Diffraction

Detailed structural analysis has been carried out on the epitaxial sputtered films using X-ray diffraction (XRD). $2\theta/\omega$ (out of plane) and φ ((111) plane) scans have been carried out for all the epitaxial films and are shown in Figure 6.7. The $2\theta/\omega$ scan can give an indication of increasing $L2_1$ ordering but this cannot be confirmed without the φ scan, as the [200] and [400] superlattice reflections observable in Figure 6.7a are common to both the $L2_1$ and $B2$ phases of Co_2FeSi. The (111) reflection is only allowed for $L2_1$ ordering **[145]**.

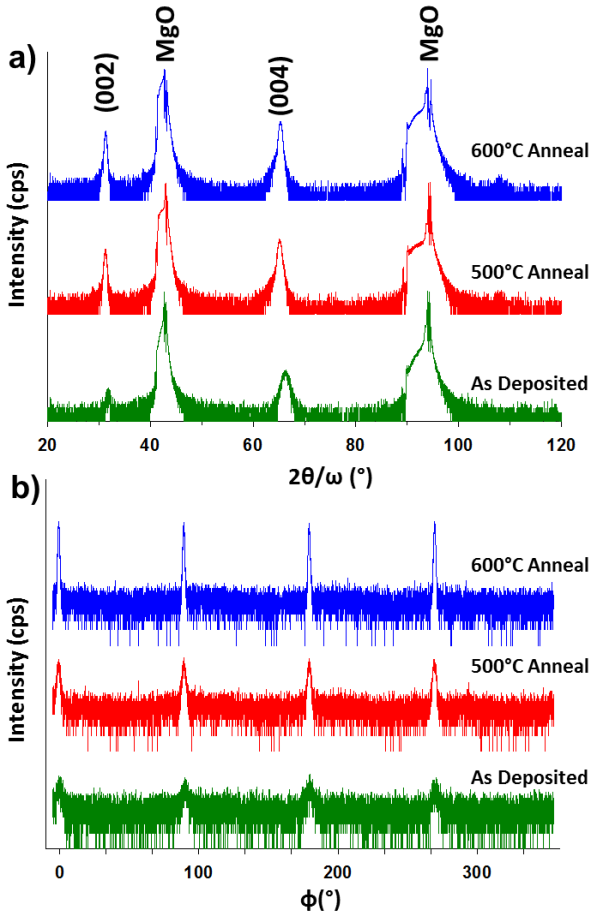

Figure 6.7. a) $2\theta/\omega$ and b) φ ((111) plane) XRD scans for epitaxially sputtered Co_2FeSi films deposited on MgO(001) substrates.

Figure 6.7a shows increasing intensity of both the (002) and (004) superlattice reflections with annealing temperature. These peaks are also seen to become sharper with annealing which means that not only is there a larger degree of $B2$ or $L2_1$ ordering but that the size of these regions is increasing. Figure 6.7b confirms the presence of $L2_1$ ordering in these films due to the presence of (111) diffraction peaks. The intensity and sharpness of these peaks is seen to increase dramatically with annealing temperature, showing that the film is becoming predominantly $L2_1$ ordered. Widespread $L2_1$ ordering is observed in the films annealed at 600°C. To quantify the extent of this ordering, an approximation of the size of the ordered regions has been made using Scherrer's formula (equation 4.6) using the FWHM of the (111) peaks in the φ scan **[130]**. In the as-deposited films, it was found that the $L2_1$ ordered regions extended an average of (70±15) nm without a change of phase. This increased to (180±10) nm for the sample annealed at 500°C and reached (374±8) nm for the sample annealed at 600°C. The decreasing error on these measurements is an estimation of the accuracy to which the FWHM can be measured. This final result for the sample annealed at 600°C is particularly important as the grain size is much greater than the typical dimensions for a nano-pillar device, typically 75 - 200 nm diameter **[42]**. As a result, devices made from films such as these are unlikely to have any changes of ordering within the volume of the Co_2FeSi layers. This would mean that the bulk spin polarisation and magnetic characteristics are constant in each of the ferromagnetic layers of the device.

6.2.2.2. HRSTEM Observation of Atomic Ordering and Film Interfaces

To confirm the degree and nature of the ordering a large amount of TEM and STEM analysis was performed. Specimens were imaged at high magnification after preparing film cross sections using the mechanical thinning method described in **[35]**. The specimens were then imaged using the JEOL JEM-2200FS STEM. This allows direct imaging of the ordering in the film. This is shown in Figure 6.8a.

The film was imaged along the (100) plane resulting in an image of the (110) face of the Co_2FeSi. A schematic of the atomic structure of this face is shown overlaid on the image. When compared to the HRSTEM image it is clear that this region of the film is $L2_1$ ordered. The brightest spots correspond to the rows of Co, whilst the alternating bright and dark spots correspond to the Fe and Si respectively. The intensity of the Fe spots is diminished from that of the Co due to the alternating Fe and

Si in the atomic column. Intensity line profiles through the atomic rows of the film were also carried out to confirm this $L2_1$ ordering over a larger area of the film. The atomic spacing was measured directly using these intensity profiles. As the Co peaks are the strongest the measurements were made Co to Co. This was carried out over an integer number of atomic peaks. For the ease of processing the data this was usually a multiple of five (as five atoms make up the edge of the [110] orientated $L2_1$ unit cell). The information is then easily converted to the lattice constant. This was then repeated up to 50 times per sample. The in-plane and out-of-plane lattice constants were found to be (5.67±0.05) Å and (5.69±0.05) Å, respectively. These values are an increase of 1.0% over the bulk value of 5.64 Å **[60]**.

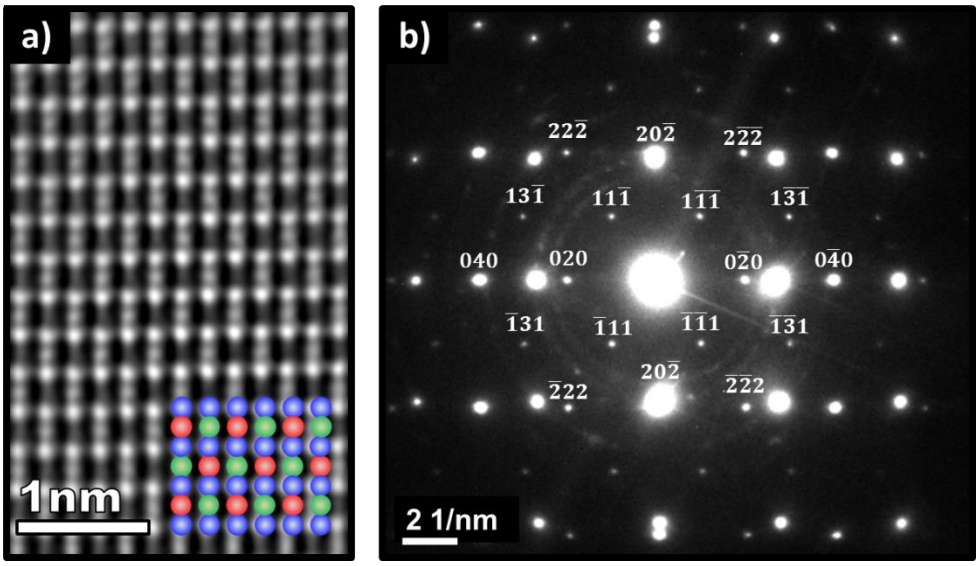

Figure 6.8. a) HRSTEM image of a Co_2FeSi epitaxial film showing atomic ordering with overlaid crystal structure showing Co (blue), Fe (green) and Si (red) atomic positions. b) SAED pattern of a Co_2FeSi film and MgO substrate with the diffraction spots corresponding to Co_2FeSi indexed.

Figure 6.8b shows the SAED pattern for the Co_2FeSi film and the MgO substrate. Only the diffraction spots corresponding to the [101] Co_2FeSi projections have been indexed. The appearance of (111) and (131) type spots is further evidence for the extent of $L2_1$ ordering in these films as these reflections are disallowed for the $B2$ structure. The SAED pattern also shows the epitaxial relationship between film and substrate, in this case MgO(001)[100]//Co_2FeSi (001)[110]. This relationship is the result of a mechanism to compensate the large lattice mismatch of 35% between the bulk lattice constant of MgO (a=4.21 Å) and Co_2FeSi (a = 5.64 Å). A 45° rotation of the Co_2FeSi unit cell allows it to cover two unit cells of the MgO thus reducing the mismatch to 5.3%. This mismatch is reduced further to 3% by the expansion of the

Co_2FeSi in-plane lattice spacing to the previously measured (5.67±0.05) Å and a contraction of the MgO lattice constant to (4.13±0.05) Å at the interface, as found from the HRSTEM.

The effect of this mismatch at the interface has been further investigated using weak-beam dark-field imaging in the JEOL JEM-2010. By imaging selectively from the MgO(020) diffraction spots, it is possible to highlight a periodic contrast variation at the film/substrate interface (Figure 6.9a). This is a result of atomic planes bending away from the imaging axis around misfit dislocation cores which appear to relieve the stress caused by the remaining 3% lattice mismatch. Using the HRSTEM it is possible to resolve these misfit dislocations and their effect on the structure of the film/substrate interface. Figure 6.9b shows this HRSTEM image of the interface whilst Figure 6.9c is a filtered image showing only the (020) planes. Superimposed onto this is a strain map created using geometric phase analysis (GPA) from the FRWRtools digital micrograph plug-in **[146]**.

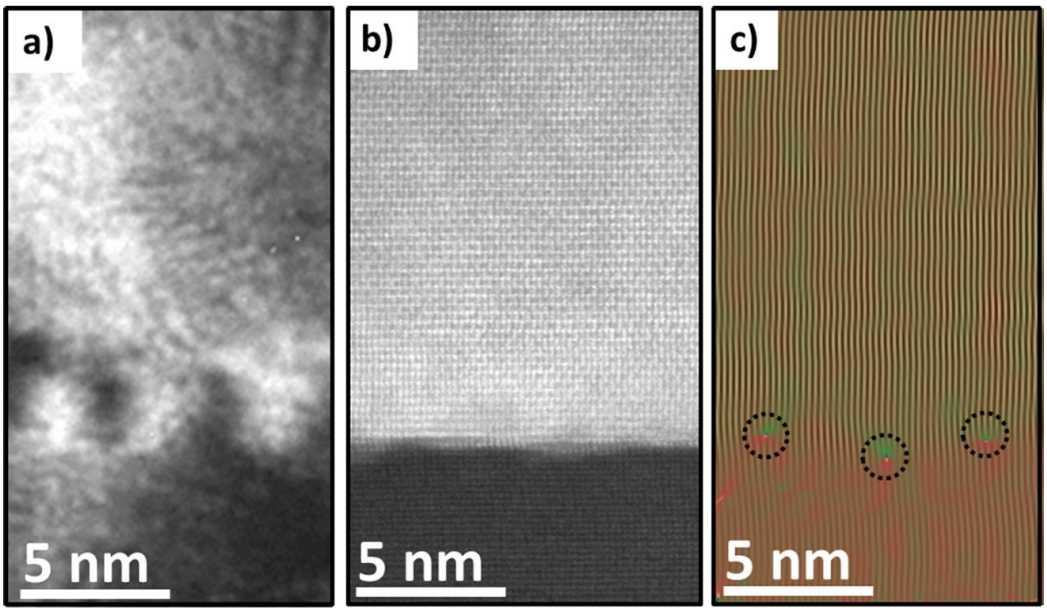

Figure 6.9. a) Weak-beam dark-field image of the Co_2FeSi/MgO interface. b) HRSTEM image of a similar region of the Co_2FeSi/MgO interface. c) Co_2FeSi/MgO interface image filtered using the (020) spots in the FFT, with superimposed strain map and highlighted dislocation cores.

GPA is based on the analysis of the phase components of the spatial frequencies which form HRSTEM images. By masking two selected Bragg spots in the Fourier transform the phases of the selected spatial frequencies can be measured. The phases of the two images can then be compared relative to one another to create a strain map

across the image. An area in the image is selected as a reference from which the relative distortion of spatial frequencies can be measured. A full discussion of the theoretical foundation of GPA can be found in reference **[147]**. To form Figure 6.9c, a region of the MgO away from the interface was chosen as the reference. This strain map highlights the cores of the dislocations at the interface and shows that these occur due to the epitaxy missing a single plane of every 20-25 MgO atomic planes. The GPA also shows that away from the interface the Co_2FeSi film becomes fully relaxed with a lattice mismatch of (4.4±1.0)% relative to the MgO substrate.

These films have been shown to have a considerably different structure to that found in the polycrystalline thin films. Samples annealed at 600°C show long range $L2_1$ ordering in the XRD measurements. This was confirmed using HRSTEM to image directly the atomic ordering. This is in contrast to the granular structure found in the polycrystalline films. The single crystal films also have a specific planar orientation defined by the epitaxy between substrate and film unlike the distributed orientations seen in the granular films. This epitaxy relationship does however result in a periodic array of misfit dislocation at the film/substrate interface which could potentially act as domain wall pins.

6.3. Magnetic Properties

6.3.1. Hysteresis

The measurement that allows the most obvious comparison of the magnetic properties of the magnetron and HiTUS sputtered films is the hysteresis loop. This allows for a comparison of coercivity (H_c), remanence (M_r) and nucleation field (H_n). A relative comparison can also be drawn for saturation magnetisation (M_s), although as these measurements are taken using the AGFM this value is dependent upon the characteristics of the probe and the sample dimensions, as discussed in section 5.1.1. The error in the reproducibility of a single measurement of M_s for a specific sample was shown by *Lewis* **[148]** to be 5.4%. This does not include any factors arising from the variation in shape, size and mass of samples or probes. Hence, it should be considered impossible to measure M_s with an accuracy of better than 10%. Therefore, most measurements are shown with the normalised or reduced moment M/M_s. any direct measurements of M_s have been carried out using the VSM as these

measurements are not probe dependent, although they are made relative to a calibration sample.

As previously discussed (section 4.1.1), the HiTUS system controls film deposition through the strength of a DC bias applied to the sputter target. This changes the deposition rate and film structure which has an extremely large effect on the hysteresis of the films. Thus, the films have been characterised both by V_B and annealing time (T_A) as shown in Figure 6.10.

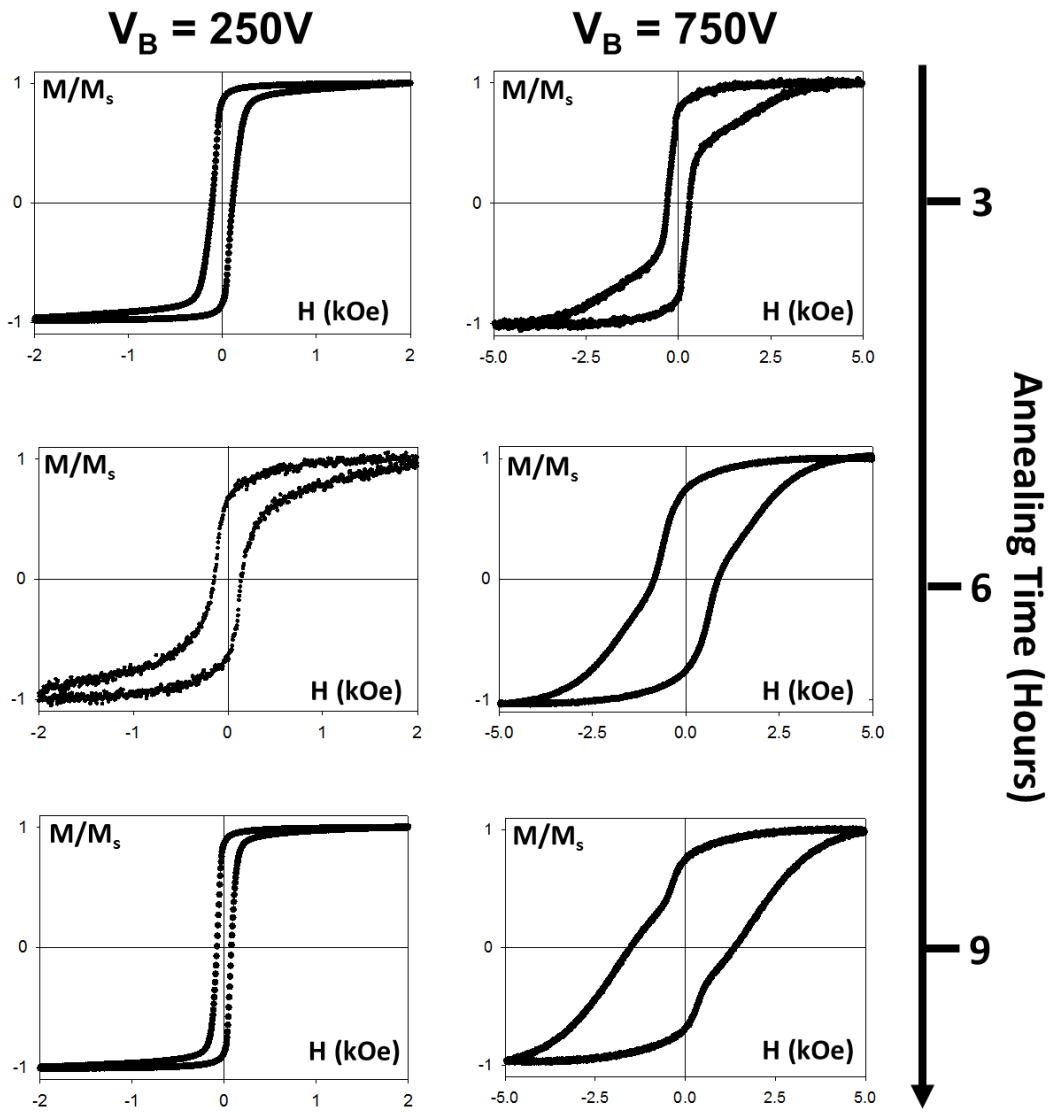

Figure 6.10. Hysteresis loops for polycrystalline Co_2FeSi films deposited at DC bias voltages of 250 V and 750 V, annealed at 500°C for 3, 6, and 9 hours.

It is shown quite clearly that V_B has a larger effect on the magnetic properties of the thin film than the annealing time, where increasing V_B results in a monotonic increase in H_c. Annealing time also shows a somewhat different variation in magnetic properties. The main difference seen in Figure 6.10 is in the shape of the hysteresis loops. The magnetisation reversal of specimens grown with a DC bias of 250 V is dominated by a single process. In contrast, the film deposited with the higher bias of 750 V shows a clearly defined two stage reversal process. Importantly the hysteresis loops for the specimen deposited with V_B =250 V and annealed for 3 and 9 hours have M_r/M_s = 0.85 and 0.87. This suggests that the grains in these films exhibit a cubic structure with a 3D random distribution of easy axes. Hysteresis loops for such systems were initially modelled by *Gans* **[149]**. The model was extended to include the entire reversal process by *Joffe* and *Heuberger* **[150]**. This model is based upon the assumption that the magnetisation reversal process takes place through coherent rotation of the spins through the material. If the reversal process becomes incoherent this model breaks down. Both these references predict M_r/M_s = 0.83 - 0.87 dependent upon the magneto-crystalline anisotropy of the material, which is in good agreement with the results presented here. The intermediate stage of annealing at 6 hours represents an intermediate step in grain development where growth and re-crystallisation result in a decrease in M_r and an increase in H_c. This is due to hindrances to the rotation of spins through the cubic crystals occurring as a result of the re-crystallisation process.

The hysteresis loops for the sample deposited with V_B = 750 V are very different, with the initial reversal taking place at a relatively small reverse field (~400 Oe) and reversing almost 70% of the material, the remaining 30% then takes a much larger reverse field to fully saturate (H_{Ms} = 4500 Oe). This two stage reversal can be seen in all samples to varying degrees. The amount of material reversing via the second process increases with annealing time. These films also show lower values of M_r/M_s. This is an indication that the structure within the grains has changed to prevent coherent reversal of the magnetisation. This, as well as the increasing secondary reversal stage, is most likely due to increased grain volume allowing the formation of domain walls within the grain. A summary of the measured quantities from all the samples studied is shown in Table 6.2.

Table 6.2. Summary of important magnetic data for polycrystalline Co_2FeSi thin films.

V_B (V)	T_A (Hours)	M_s (±10% emu/cm^3)	M_r/M_s	H_c (Oe)
250	3	300	0.85	131
	6	90	0.67	154
	9	370	0.87	80
500	3	210	0.78	220
	6	460	0.69	825
	9	620	0.78	450
750	3	210	0.80	300
	6	570	0.75	850
	9	570	0.75	1430

These unusual two stage hysteresis loops are quite easily understood when looked at in the context of the structural properties of these films. The wide distribution of grain sizes in these films means that there are a number of small grains which formed due to single nucleation events. These particles are more than likely to be polydomain as the critical size for single domain behaviour, (r_c), in these materials is estimated to be 10 nm using equation 6.3 **[49]**.

$$r_c \approx 9\frac{(A_{ex}K)^{1/2}}{\mu_0 {M_s}^2} \tag{6.3}$$

where A_{ex} is the exchange stiffness and K is the anisotropy constant. The values used for this estimation are from single crystal films of the same material **[60]**, and as a result the value for the critical size is likely to be an underestimate. Although these particles are polydomain they have very few hindrances to domain wall motion and thus reverse their magnetisation in low field. Due to their formation through coalescence, the larger grains take an extremely high applied field to reverse their magnetisation. This is the result of a number of extremely strong domain wall pins in the regions where a grain boundary would have previously existed.

In contrast to the polycrystalline samples the epitaxially sputtered samples have hysteresis loops with much lower H_c (>15 Oe). These films are all sputtered at a constant bias voltage set by the magnetron system. Therefore, the variation in these films comes from the temperature at which the samples were annealed. It is important to note that the AGFM measurements were taken along the easy axis of these films, that is along the (100) crystal edge of the MgO substrate. This corresponds to the

(110) direction of Co_2FeSi as per the epitaxial relationship shown in Figure 6.11. It should therefore follow that taking a measurement at 90° to this direction would also produce an easy axis loop. By measuring M_r/M_s as a function of the applied field angle it can be seen that the easy axis corresponds to the (110) direction of Co_2FeSi, however at 90° a value of M_r/M_s = 1 is not achieved. This is due to the presence of a small applied field (<100 Oe) during the annealing process from the remanent magnetisation of the pole pieces of the magnet in which the furnace was situated.

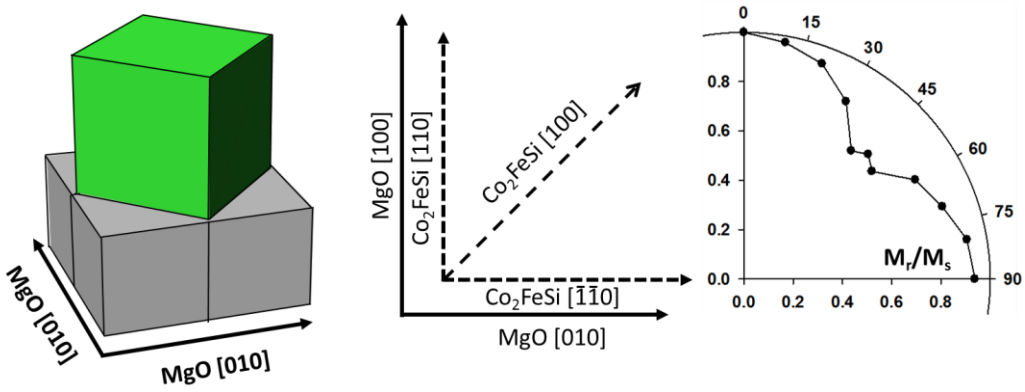

Figure 6.11 Schematic diagram of epitaxial relationship between MgO and Co_2FeSi with the resulting crystallographic directions and the effect on the anisotropy.

This applied field during annealing induces an extra anisotropy in the direction of the field (110) which must be overcome when measuring along the $(1\bar{1}0)$ direction. This applied magnetic field during annealing results in a change in the cubic symmetry of the exchange interaction in the lattice. This results in an offset of domain wall energy therefore stabilising the domain walls in the easy direction. This induced anisotropy behaviour has been documented in cubic materials since 1955 **[151]**. This stabilisation results in the change in remanence observed between the measurements along the (110) and $(1\bar{1}0)$ directions, as the increased anisotropy reduces the susceptibility of the film to nucleation of reverse domains due to thermal activation. *Costa-Kramer et al.* **[152]** observed similar behaviour in 20 nm thick Fe films grown on MgO(001) which was explained by a change of domain wall type in the films. The magnetisation reversal along the induced easy axis (110) is through the nucleation and propagation of 180° domain walls, whilst along the $(1\bar{1}0)$ direction the reversal process is facilitated through the nucleation and propagation of 90° domain walls. Another feature of the angular dependence is a small peak at an applied field angle of 45°, corresponding to the (100) direction of the Co_2FeSi. This result is analogous to

that shown by *Trudel et al.* **[46]** in the similar material $Co_2CrFeAl$. It does however contradict the distribution of easy axes shown by *Gaier* **[153]**. This is a result of a Cr buffer layer used in the latter which distorts the crystal symmetry resulting in strong uniaxial behaviour.

In the easy axis loops taken using the AGFM, H_c can be seen to increase monotonically with annealing temperature, or if related back to the XRD analysis, the extent of $L2_1$ ordering in the film. It can also be seen from Figure 6.12 that the only significant variation comes from the field at which magnetisation reversal nucleates (H_n). This nucleation field controls both H_c and the squareness of the loops. The variation in H_n is a result of the mixture of various phases of Co_2FeSi existing within the thin film. In the as-deposited film, there is a larger concentration of low anisotropy $A2$ and $B2$ phases, resulting in lower energy barriers to reverse domain nucleation. H_n is shown to increase with the extent of $L2_1$ ordering, as this reduces the number of regions of lower anisotropy which give lower energy barriers to reversal, thus reducing the density of possible nucleation sites at any given field.

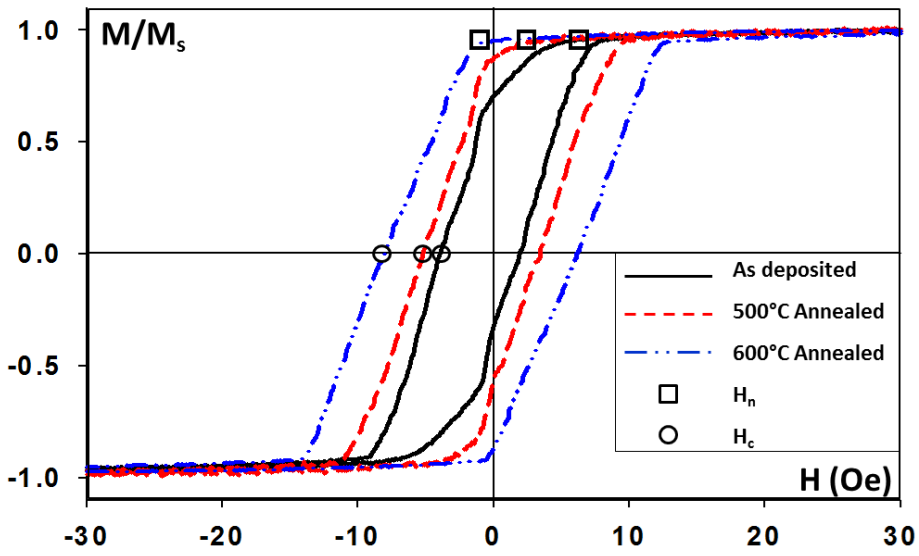

Figure 6.12. Hysteresis loops for epitaxially sputtered Co_2FeSi thin films.

The hysteresis loop for the as-deposited sample , and to a lesser extent of the sample annealed at 400°C, shows a reversal process which takes place in at least two if not three stages. This is due to an unusual distribution of energy barriers to reversal in these films. This arises from the co-existence of a number of crystallographic phases of Co_2FeSi in these films, as shown from the XRD. The intermixing of these phases

results in areas of the film with lower magneto-crystalline anisotropy which reduces the energy barrier to reversal so reverse domains can nucleate at lower reverse field. These regions have such low energy barriers that they are thermally unstable at room temperature. This is shown by values of M_r/M_s that are less than 1 for these films.

The distribution of reversible and irreversible magnetisation reversal steps for the as-deposited film and the film annealed at 500°C would be distinctly bi-modal. The first peak is due to disordered material where reverse domains can nucleate easily, while the larger second peak is the reversal of the remaining well-ordered film by domain wall motion. For the bi-modal distributions, the blocking temperature (T_B) for these films lies within the distribution. T_B is the temperature above which magnetic entities will become superparamagnetic. For uniaxial single domain particles this is given by equation 6.4 **[47]**:

$$T_B = \frac{KV}{25k_B}(1 - H/H_K)^2. \qquad (6.4)$$

Where K is the anisotropy constant for the material and V is the volume of the particle. The factor 25 is a direct result of the typical measurement time of 100 seconds. For epitaxially sputtered single crystal cubic films such as these this will not hold exactly. However, it does show that this superparamagnetic behaviour of the regions within this film will be controlled by both the volume of the region and the anisotropy. Therefore, any regions of the low anisotropy $A2$ phase of Co_2FeSi or the amorphous as-deposited matrix will most likely result in superparamagnetic regions in the film. This is due to both the low anisotropy and the small volume of these regions.

6.3.2. DCD Curves

As the first stage to understanding the reversal processes in both the polycrystalline and epitaxial films, DC demagnetised (DCD) remanence curves have been measured for all the specimens. As previously discussed in chapters 2 and 5 remanence curves give a great detail of understanding about the fundamentals of the magnetisation reversal process as they measure only the irreversible component of the magnetisation at any given field. Because of the need to differentiate these curves to find χ_{irr}, which is needed for the estimation of V_{act}, it is crucial that the noise in the measurement is limited as it will be amplified when taking the gradient between two points. To remove any noise from the measurement, the data is smoothed using a five point moving quadratic as described in section 5.1.3. The DCD curves for an epitaxial

film and a polycrystalline film are shown in Figure 6.13. Both DCD curves are shown with the specimens' hysteresis loop for ease of comparison.

The data in Figure 6.13 shows that the two film structures have fundamentally different reversal mechanisms. Figure 6.13a shows the DCD curve from the polycrystalline film. Here the DCD curve follows the hysteresis loop until 800 Oe at which point the DCD curve diverges from the hysteresis loop at a much greater rate. This suggests that there are two different mechanisms in the reversal process. At fields below 800 Oe the magnetisation reversal is controlled by domain nucleation and growth within the ordered cores of the grains which nucleated during the initial annealing process. Above 800 Oe much stronger domain wall pins exist which require much greater fields to overcome. These domain wall pins most likely form during the coalescence phase of the grain growth. The film also contains a large number of thermally unstable grains, shown by the difference in moment between the hysteresis loop at saturation and the DCD curve at the same field. Almost 25% of the saturation moment can be attributed to these grains, which consist of the material from the as deposited matrix which has failed to crystallise.

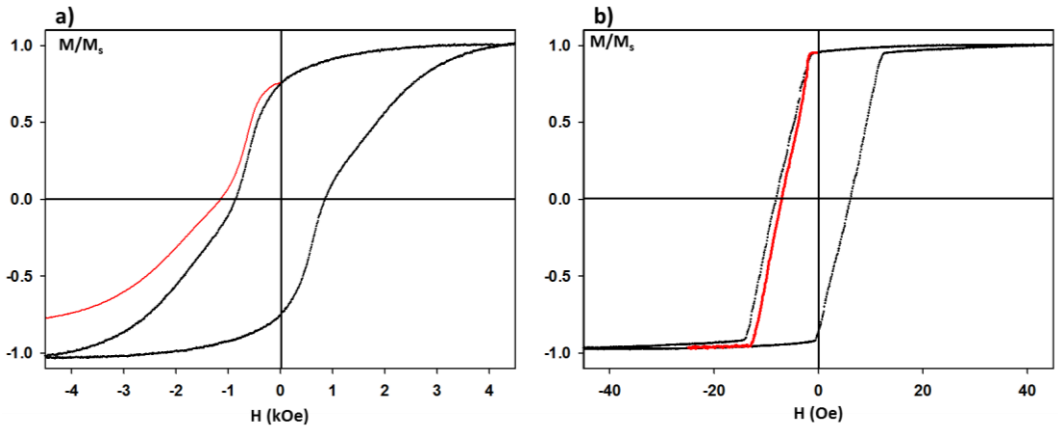

Figure 6.13. Hysteresis loops (black) and DCD remanence curves (red) for a) a polycrystalline Co_2FeSi film deposited with V_B=750 V and annealed at 500°C for 6 hours and b) an epitaxially sputtered Co_2FeSi film annealed at 600°C for 1 hour.

In Figure 6.13b, for the epitaxially sputtered film the DCD curve follows the hysteresis almost exactly, suggesting a single reversal mechanism consisting of entirely irreversible processes. This behaviour is consistent with a series of periodically spaced low energy domain wall pins which must be overcome in turn to reverse the magnetisation of the entire sample. The previously discussed misfit

dislocations at the film/substrate interface are a possible origin of this periodic pinning.

6.3.3. Activation Volumes

Measurements of magnetic time dependence have been made for all the samples, allowing access to the magnetic viscosity coefficients which are needed for calculation of the activation volume (V_{act}). The decay of magnetisation was measured at 150 points over 600 seconds for each field step. All the decay curves have been found to be linear in $\ln(t)$, a small selection of these can be seen in Figure 6.14b. Because of this, the fluctuation field (H_f) and hence V_{act} can be obtained through the $S(H)/\chi_{irr}(H)$ method using equations 6.5 and 6.6 **[154]**.

$$V_{act} = \frac{k_B T}{M_s H_f} \tag{6.5}$$

$$H_f = \frac{S(H)}{\chi_{irr}(H)} \tag{6.6}$$

Figure 6.14a shows the $S(H)$ and χ_{irr} curves for a polycrystalline Co_2FeSi film annealed for 9 hours. The χ_{irr} curve is noticeably bi-model as is the $S(H)$ curve. This is a result of the previously discussed two phase reversal process. It must also be noted that not all the polycrystalline specimens exhibit such behaviour. It is therefore important to remain consistent when describing the activation volume. As all the samples exhibit the initial nucleation phase of the reversal the measurement of the activation volume will take place in this part of the process indicated by the first peak in the χ_{irr} curve shown in Figure 6.14a.

V_{act} calculated in this way, (for all polycrystalline specimens) can be seen in Table 6.3. The measured value of saturation moment has been used for each sample after calibrating the AGFM probe before each measurement. The saturation magnetisation has been calculated by setting the volume of the film equal to the film thickness multiplied by the area of substrate covered by the film. In the case of these specimens the film covered 100% of the substrate surface.

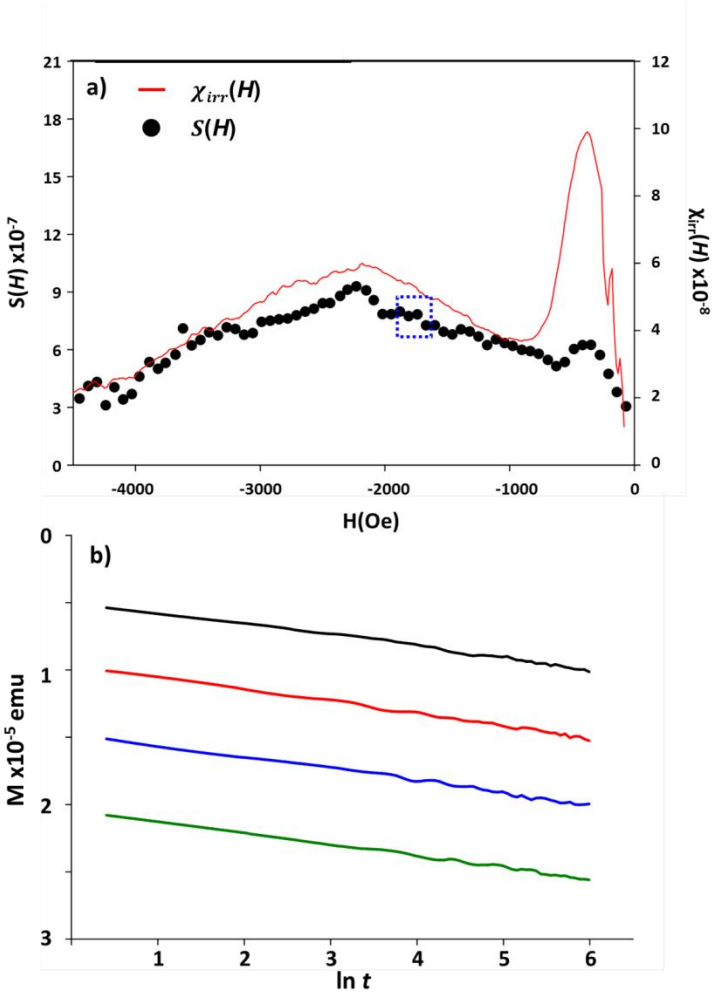

Figure 6.14. a) $S(H)$(black circles) and $\chi_{irr}(H)$ (red line) curves for a polycrystalline Co_2FeSi sample deposited at V_B=750 V and annealed at 500°C for 9 hours. b) The magnetisation decay curves for the highlighted region (dashed box) in S(H) above.

For ease of comparison V_{act} has been converted to an activation diameter (D_{act}). D_{act} is calculated by modelling V_{act} as a cylinder through the film thickness. It is immediately clear that the values of D_{act} remain almost constant with both V_B and T_A. This suggests that the initial nucleation process in each film takes place from the same volume of magnetic material. Where the films then begin to differ is in the subsequent reversal process, resulting in the extremely large coercivities (H_c) and saturation fields (H_{MS}) seen for some films (Table 6.2), whilst others remain very low.

Table 6.3. Summary of activation volume data for polycrystalline Co_2FeSi thin films.

V_B (V)	T_A (Hours)	M_s (±10% emu/cm^3)	$\chi_{irr}(H)$ (±0.1 x 10^{-7})	$S(H)$ (±1 x 10^{-7})	V_{act} (x10^{-18} cm^3)	D_{act} (±2 nm)
250	3	300	11	46	33	45
	6	90	3	28	53	58
	9	370	19	80	26	41
500	3	210	5	33	29	43
	6	460	4	8	43	52
	9	620	10	16	43	53
750	3	210	7	42	34	47
	6	570	6	9	52	58
	9	570	4	10	31	45

For the epitaxially sputtered films, the activation volumes have been found to be much smaller with D_{act} ~5 nm for all films irrespective of annealing time. The magnetic viscosity and χ_{irr} curves also show significantly different trends to those in the polycrystalline films. Both χ_{irr} and $S(H)$ exhibit a strong peaked behaviour as shown in Figure 6.15. None of the samples show bimodal behaviour of $\chi_{irr}(H)$ as one may expect from simply observing the hysteresis loops. This means that the two stage reversal shown in the hysteresis loops (Figure 6.12) is a product of reversible processes in the film.

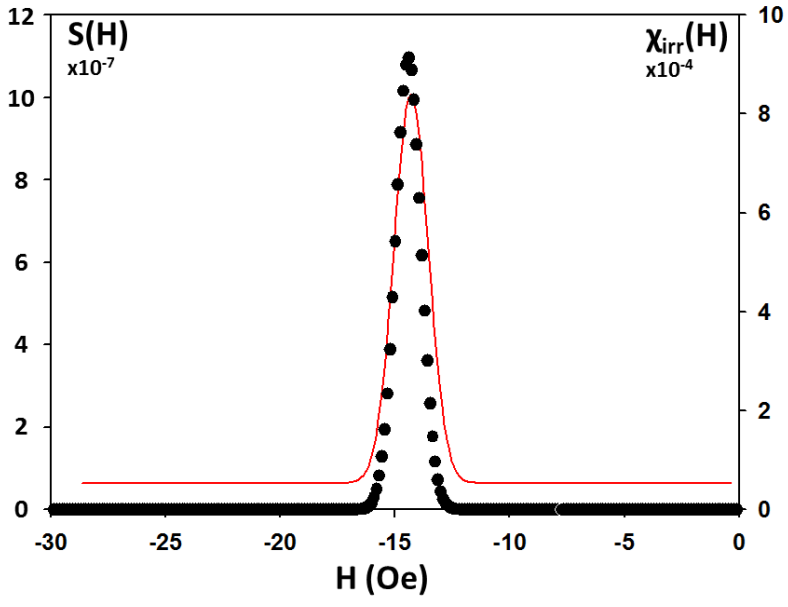

Figure 6.15. $S(H)$ (red line) and $\chi_{irr}(H)$ (black circles) for an epitaxially sputtered Co_2FeSi sample annealed at 600°C.

This is a result of the very sharp switching field distribution as the magnetisation reversal process completes within 15 Oe. The sharp switching behaviour is unusual considering how small the activation volumes in these films are. This shows just how weak and closely spaced in energy the domain wall pins in these films are. Even the narrow energy barrier distribution for these films was sufficiently wide such that the magnetisation decay curves for this material were once again linear with $\ln(t)$, so the $S(H)/\chi_{irr}(H)$ method was used to calculate H_f.

6.4. Comparison of Structural and Magnetic Phenomena

The polycrystalline and epitaxially sputtered Co_2FeSi films have very different structural and magnetic properties. The polycrystalline films exhibit a wide range of properties dependent on the initial deposition conditions. Figure 6.16 compares the magnetic activation diameter with the physical grain size in these films. It is clear from the figure that there are two different regimes in both the structural and magnetic properties.

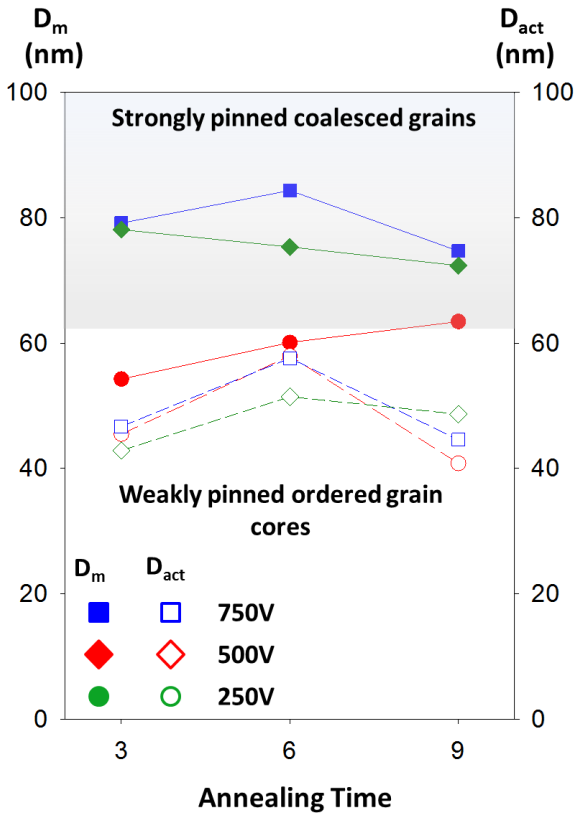

Figure 6.16. D_m (closed symbols) and D_{act} (open symbols) displayed as a function of annealing time for polycrystalline Co_2FeSi films grown with bias voltages of 250 V (circles), 500 V (rhombus) and 750 V (squares)

The films deposited using a DC bias voltage of 250 V have grain volumes roughly equal to the magnetic activation volumes. This suggests that these particles exhibit either single domain particle behaviour, where the reversal occurs through rotation of the magnetisation in the grain, or more likely, that reverse domains nucleate in the film, and the ordered grains can switch coherently due to very few domain wall pins. For the films grown at high V_B the same nucleation event occurs in these ordered 'core' grains. However, due to the large proportion of coalesced grains, there are a much higher density of strong domain wall pins at the grain boundaries where material becomes magnetically disordered. A much larger reverse field is then required to sweep out these domain wall pins.

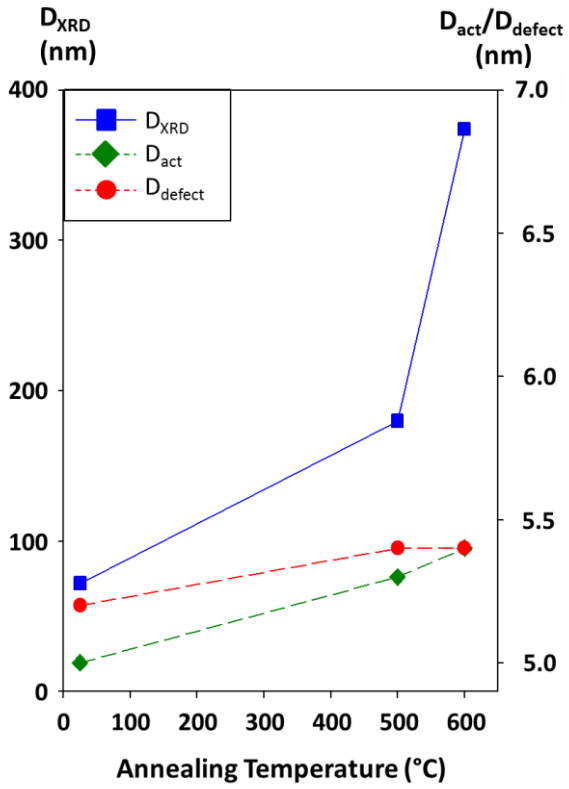

Figure 6.17. D_{XRD} (squares), D_{act} (rhombuses) and D_{defect} (circles) displayed as a function of annealing temperature for epitaxially sputtered Co_2FeSi films.

The story for the epitaxial films is much different. From the XRD results it is shown that these films are well ordered over extremely long ranges (>80 nm). Furthermore, the size of ordered regions increases with annealing temperature. However, the activation volumes are considerably smaller than the ordered regions and show very little temperature dependence. This means that the initial nucleation event is controlled by a number of magnetically soft disordered regions in the film,

whilst the subsequent reversal mechanism is controlled by another structural property. By converting the activation volumes to an activation diameter more insight into the source of this domain wall pinning can be found. This is shown in Figure 6.17 where the size of the ordered regions (D_{XRD}) and D_{act} are shown relative to one another. D_{act} is coincident within error of the mean spacing of misfit dislocation at the film/substrate interface. This suggests that the reversal mechanism in these epitaxial films is controlled by the distribution of structural defects.

It has been shown that the structure of these Co_2FeSi films have a profound effect on their magnetisation reversal. The polycrystalline films show a magnetisation reversal process dominated by the initial deposition conditions which control the number of ordered grain nucleation events, subsequently controlling the grain development process and amount and strength of domain wall pins in the material. The epitaxial films however have a magnetisation reversal process controlled by the defects that occur due to epitaxial growth. This is of particular importance as this domain wall pinning limits the rate at which magnetisation switching can occur. This may make epitaxial tunnel barrier devices unsuitable for high frequency applications. However, the effect of this could be removed by choosing specific material systems with no lattice mismatch, thus removing the majority of these misfit dislocations.

Chapter 7. The Effect of Seed Layers on Polycrystalline Films

By depositing layers between the substrate and subsequent magnetic layers the crystallographic structure and growth processes of thin films can be controlled. The effect that these seed layers have on the structure and magnetic properties of Co_2FeSi polycrystalline films has been studied. Initially, Ag seed layers have been tested because Ag is commonly used as the bottom electrode in nanopillar devices. This study has then been extended to multiple seed layers, as well as antiferromagnetic seed layers to induce an exchange bias in the Heusler alloy films.

7.1. Film Preparation

Thin film samples with structure Ag (6 nm)/Co_2FeSi (20 nm)/Ru (3 nm) were deposited onto single crystal Si and MgO (001) substrates as well as carbon coated copper TEM grids, using a HiTUS sputtering system with a base pressure better than $4x10^{-5}$ Pa. Films have been deposited using DC bias voltages of 250 V, 400 V, 550 V, 700 V, 850 V and 990 V. The bias voltage in the HiTUS system controls the energy of ions bombarding the sputter target, this changes the growth rate and subsequent grain size in the sputtered films **[122]**. The films have been post-deposition *ex-situ* annealed for 3, 6 and 9 hours at 300°C in a vacuum better than $3x10^{-3}$ Pa. As with the specimens described in the previous chapter, the post deposition annealing facilitates the growth of grains from the as-deposited matrix. However, due to the Ag seed layer, this initial as-deposited state is no longer superparamagnetic. A number of regions form larger initial crystallites which contribute to a small magnetic hysteresis of $H_c \leq$ 10 Oe for all specimens.

7.2. Magnetic Characterisation

Hysteresis loops have been measured for all specimens after annealing. These specimens all show low coercivities of less than 40 Oe. This result is itself significant over the previously studied films deposited without seed layers. For spintronic devices where fast, coherent, magnetisation reversal is required, a low coercivity is essential. In the previous study no film exhibited a coercivity of less than 80 Oe. Two examples of the hysteresis loops for these films are shown in Figure 7.1. It is immediately apparent that these films have a very different magnetic reversal process than those previously discussed. These hysteresis loops are extremely square in shape suggesting that the reversal process is dominated by a single nucleation event which reverses the majority of the material in the film.

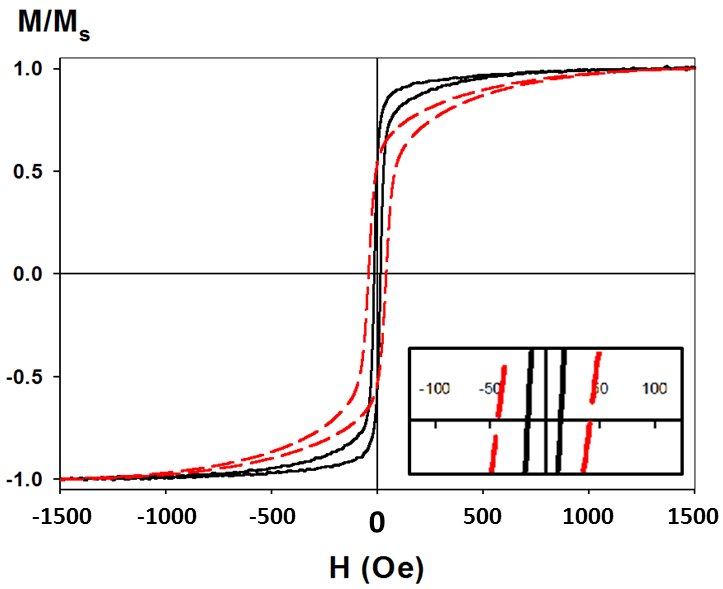

Figure 7.1. Typical *M-H* hysteresis loops for specimens deposited with V_B=250 V (solid line) and V_B=700 V (dashed line).

Figure 7.2 shows that increasing the deposition bias voltage results in an increase in H_c. This is not a consistent trend since after 700 V there is a drastic decrease, as shown in Figure 7.2a. At some point the structure of the films changes to such a degree that the coercivity is reduced to less than 10 Oe. This suggests that for the specimen deposited with V_B = 990 V there is a significant change to either the crystalline or morphological structure. The same trend however is not echoed in the data for the saturation magnetisation. Here, there is a monotonic increase in M_s with V_B, which is almost linear as shown in Figure 7.2b. This means that either there is now

more of the film crystallised into magnetically ordered Co_2FeSi phases or the grains have crystallised into the higher moment $L2_1$ phase of Co_2FeSi.

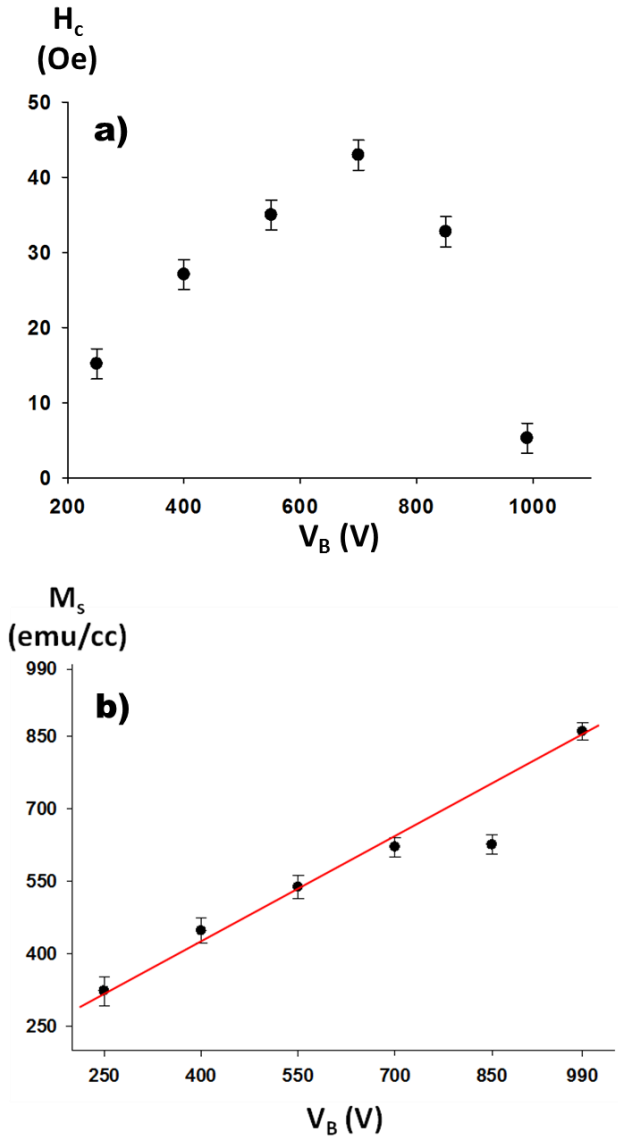

Figure 7.2. a) Variation in H_c with V_B and b) Variation in M_s with V_B for Co_2FeSi films with Ag seed layers.

The variation in magnetic properties with annealing time was also studied. The change in both H_c and M_s for samples annealed for 3, 6, and 9 hours was measured. The data for the variation of M_s with annealing time is shown in Figure 7.3a. For all samples there is an increase in M_s up to 6 hours after which M_s decreases. This initial increase is due to the re-crystallisation of nucleated grains into states of increased $B2$ and $L2_1$ ordering. For the sample deposited with a DC bias of 990 V, M_s reaches 880 ± 50 emu/cc which is 80% of the bulk value for this material **[155]**. This is evidence for

increasing amounts of $L2_1$ and $B2$ ordering in the grains as the film is unlikely to be 100% crystalline. After 6 hours M_s decreases for all samples. This is due to segregation of Si from these ordered grains, which was discussed in the previous chapter and reported for a similar material, Co_2MnSi **[123]**.

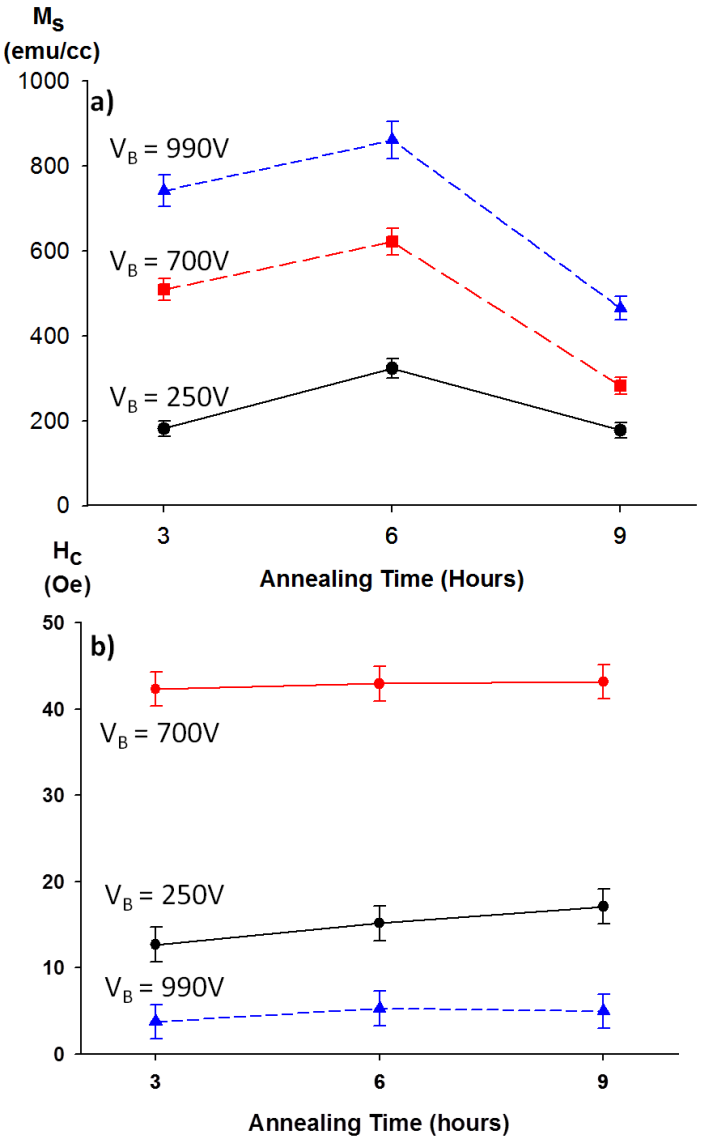

Figure 7.3. Graphs showing the variation of a) M_s and b) H_c with annealing time for films deposited with V_B = 250 V, 700 V and 990 V.

What is more interesting is the lack of variation in H_c shown in Figure 7.3b. This suggests that the seed layer has constrained the grain size of the Co_2FeSi layer such that the distribution of energy barriers in this film remains constant with annealing time.

7.3. The Effect of Seed Layers on Film Structure

7.3.1. Grain Size and Structural Ordering

The JEOL JEM-2011 has been used to take plan-view TEM images of the all films for grain size analysis. The microscope has also been used in diffraction mode to take selected area electron diffraction (SAED) patterns in order to compare crystallographic ordering within the films. A selection of bright field TEM images and SAED patterns is shown Figure 7.4.

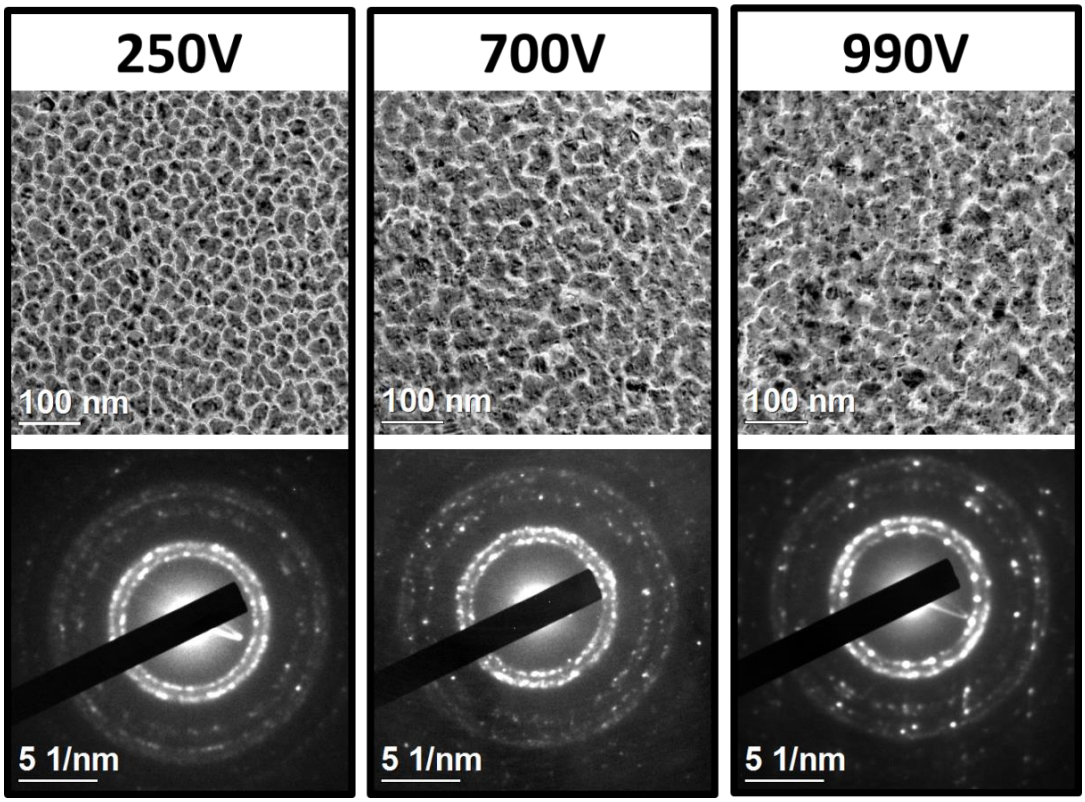

Figure 7.4. Bright field TEM images and SAED patterns for samples deposited with V_B = 250 V, 700 V and 990 V.

The first point to note is the difference in structure between the images of the films with seed layers to those previously studied without seed layers in chapter 6. For ease of comparison the two different film structures are shown in Figure 7.5. The films show an extremely segregated granular structure with each dark 'grain' surrounded by a much lighter region, which is believed to be a nano-crystalline matrix of the Co, Fe and Si but with compositional variation somewhat away from Heusler alloy stoichiometry. Most likely this material is Si rich. The grain size in these films is also reduced, with a maximum median grain diameter of 40 nm compared to those

previously discussed where D_m could be as high as 84 nm. Although this is only half of the diameter, it translates as a 4-fold decrease (as film thickness is constant) in volume which has a much larger effect on the magnetic properties. The grains for all specimens are within the range of 28 to 40 nm which means that they are almost certainly magnetically poly-domain. Therefore, the previously discussed magnetisation reversal is through domain wall motion within the grains. It can also be seen from the figure that as the deposition bias voltage is increased the amount of grain segregation decreases. The size of grains in the films follows a similar trend to that seen for H_c. There is an increase in median grain diameter up to the film deposited with V_B = 700 V after which there is a sharp decrease. This is in contradiction to the well-established trend of grain size for the HiTUS system **[122]**. This means that there is something unusual happening with the micro-structure of the ternary alloy films.

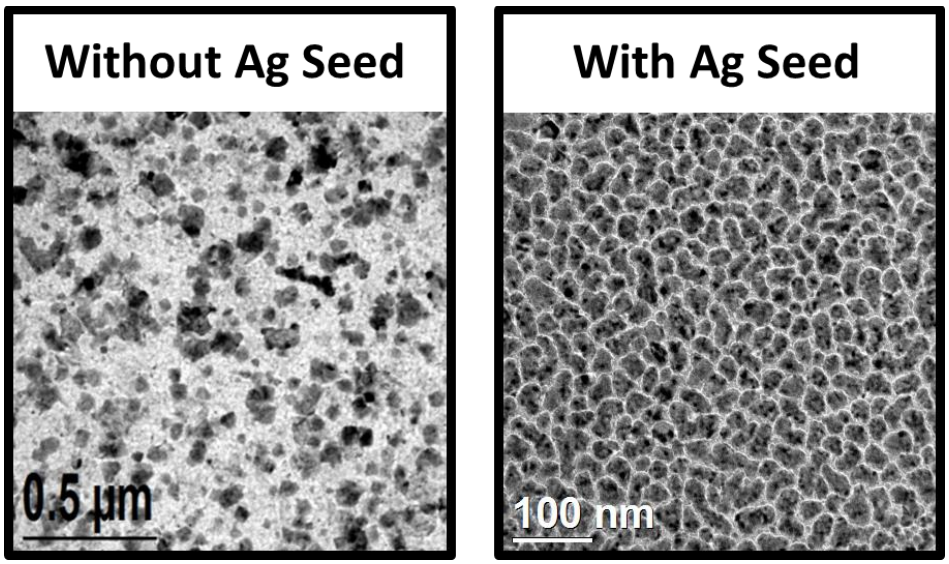

Figure 7.5. Comparison of polycrystalline Co_2FeSi thin films with and without an Ag seed layer deposited with V_B=250V and annealed for 3 hours.

The SAED patterns also seen in Figure 7.4 provide some evidence of the origin of the continued increase in M_s with V_B. Figure 7.4 shows an increase in the intensity and number of diffraction spots in the patterns with increasing V_B. This confirms that as V_B is increased so are the number of crystallised grains. As well as an increase in the number of crystallised Heusler grains, the increased intensity is most likely due to the grains themselves becoming more ordered into the Heusler phase. The result of which is the increased saturation magnetisation shown in Figure 7.2b.

7.3.2. Island Growth of Ag Seed Layers

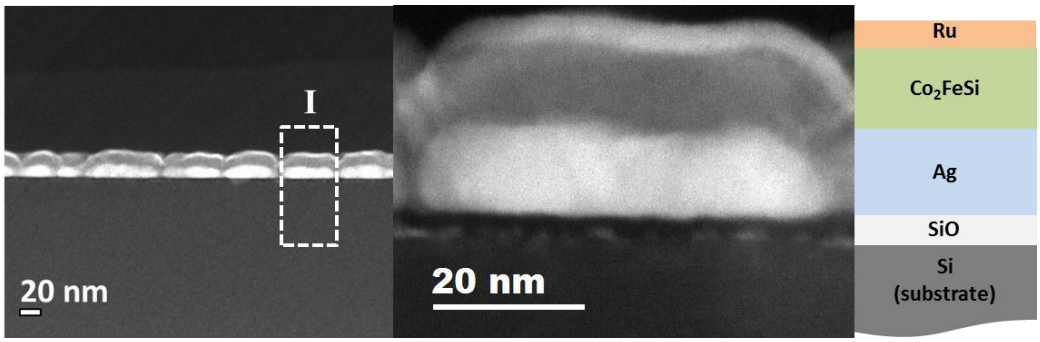

Figure 7.6. Cross-sectional STEM image, showing island growth of an Ag seed layer and Co_2FeSi film deposited with V_B=850 V.

To understand the unusual trend seen in the grain size of these films, and as a result H_c, cross sectional STEM has been carried out. The cross sectional specimen has been prepared following the method outlined in reference **[35]**. The cross sectional image of the sample is shown in Figure 7.6. It is immediately apparent from the figure that these films have grown with an unusual island structure not seen before for films deposited using the HiTUS system. The Ag seed layer was deposited with a nominal thickness of 6 nm measured by a quartz crystal thickness monitor in the HiTUS. The figure however shows islands of Ag with thicknesses approaching 12 nm, double the thickness measured during deposition.

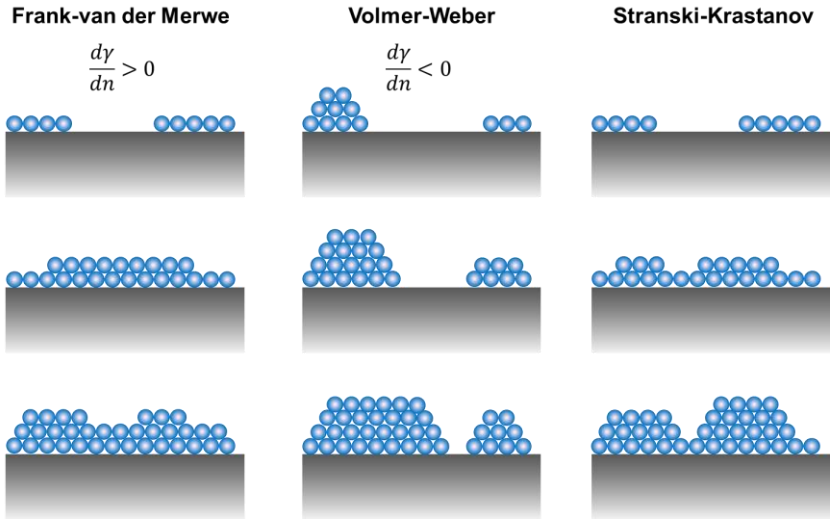

Figure 7.7. Schematic diagram of possible epitaxial growth modes **[156]**.

Ag deposits much faster than many other materials in the HiTUS system with a sputter rate of between 1.5Å/s and 2.5Å/s. This results in a large difference in chemical potential between the atoms arriving at the substrate surface and the surface

itself. From the STEM image this surface appears to be a thin (~1 nm) oxide layer. The result of this is the formation of 3D islands by a Volmer-Weber process **[157]**. The island themselves are likely to nucleate at points of specific structural variation of the surface such as peaks and troughs in the oxide layer at the Si surface. The chemical potential is such that any adatoms reaching the surface are more strongly bound to the other atoms arriving at the surface than the surface atoms, resulting in the formation of islands instead of a continuous film. From the STEM image it is also possible to discern that this process is the Volmer-Weber growth mechanism and not the more commonly found Stranski-Krastanov process as the islands are isolated from one another and not linked by an initial continuous layer. The difference between the three growth modes is shown schematically in Figure 7.7. The growth mechanism is controlled by the chemical potential of the first few deposited layers relative to the substrate. This can be modelled using equation 7.1 **[158]**:

$$\gamma(n) = \gamma_{\infty} + \gamma_{a}(n). \tag{7.1}$$

Where $\gamma(n)$ is the chemical potential of the system with n deposited atoms, γ_{∞} is the bulk chemical potential of the substrate and $\gamma_{a}(n)$ is the chemical potential of adatoms reaching the surface. The term $\gamma_{a}(n)$ actually comprises the potentials for the atom as well as further terms related to stresses due to the epitaxy between the film and the surface. The growth mode is then dependent on $d\gamma/dn$. For clarity, a layer by layer (Frank-van der Merwe) process occurs when this derivative is greater than 0 whilst if the derivative is less than 0 the Volmer-Weber mode occurs. The mixed Stranski-Krastanov mode occurs when there is a change in the chemical potentials after the first few monolayers have been deposited so that the conditions for layer by layer growth no longer exist and island growth takes over.

This island structure is clearly the origin of the unusual trend in the grain size distribution of the Co_2FeSi layers. Initially, at low deposition bias voltages, islands of Ag form with a diameter of ~30 nm. These islands then constrain the growth of Co_2FeSi such that a single grain forms on each island, with a diameter equal to that of the island, as V_B increases so does the size of the Ag islands. The same mechanism holds that a single Heusler alloy grain grows on each island so that the size of Co_2FeSi grains also increases. V_B also controls the number of nucleation sites for these Ag islands. As the number of islands increases they begin to coalesce. The cross section

image shown in Figure 7.6 is from the film deposited at 850 V and it shows that a number of the Ag islands are coalescing to form much larger islands. For the film deposited with V_B =990 V this coalescence has occurred to such an extent that the seed layer could be considered as being quasi-continuous. The much reduced grain segregation in Figure 7.4 also shows this. The continuity of the seed layer changes the growth process of the Co_2FeSi, whose structure is now controlled by single grain nucleation events with limited constraint from the seed layer. This results in much smaller grains and as a consequence a much reduced energy barrier to magnetisation reversal. The effect of this is the extremely small coercivity in the films deposited at a DC bias of 990 V.

7.4. Control of Island Growth with Cr Buffer Layers

To stop the Volmer-Weber process seen in the previous films, a layer of Cr was deposited to chemically wet the substrate before Ag deposition. Cr deposited using the HiTUS system is known to grow as a continuous film, even with layer thicknesses of less than 3 nm, due to its low deposition rate **[121]**. Cr also has a much better lattice match with Ag than either crystalline Si or the oxides at the substrate surface, again reducing any energy contribution from strain and dislocations between the two layers.

Films have been deposited under the same conditions as those previously used for the samples with just Ag seed layers. This time however, a 3 nm Cr buffer layer was deposited before the 6 nm of Ag. The result of this thin layer of Cr is dramatic. Figure 7.8 shows a bright field TEM image of the specimen in cross section. From the image it is clear that the Cr buffer layer has prevented the island formation in the Ag layer producing a film with a peak to peak surface roughness of < 1 nm. All these films have been grown at a deposition bias voltage of 850 V and the thickness of the Ag seed layer has been varied between 6 and 30 nm. This was carried out to observe the effect of Ag thickness. The use of Ag seed layers as a bottom electrode in STT-MRAM type devices would require a film thickness of greater than 50 nm to achieve a uniform current density perpendicular to the pillar. It is therefore important to understand how polycrystalline buffer layers of that thickness influence the magnetic and structural properties of the Heusler films. The second consideration in the use of Ag is that it acts as a barrier to Cr diffusion into the Co_2FeSi layer, which has been reported to lead to increased coercivities through structural disorder **[159]**.

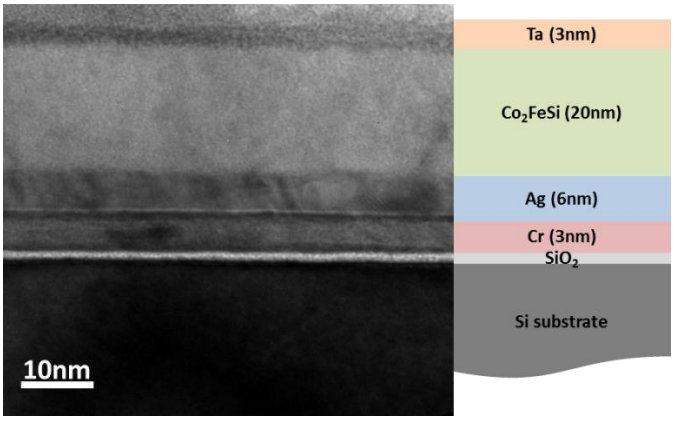

Figure 7.8. Bright field TEM image of a film cross section for a Cr (3 nm)/Ag (6 nm) dual seed layer film deposited with V_B=850 V.

Magnetically, these specimens are quite different to those deposited with just an Ag seed layer. The samples were post deposition annealed at 300°C for up to 5 hours under a vacuum of better than $3x10^{-3}$ Pa. Figure 7.9 shows a typical hysteresis loop for a Cr buffered film, annealed for 3 hours. It is immediately apparent that the shape of the hysteresis loop has changed. The squareness of the loop (M_r/M_s) has increased from 0.61 to 0.85 and the field at which saturation of the magnetisation occurs has decreased from 1000 Oe to 44 Oe. This means that the magnetisation reversal mechanism in these films is very different. The coercivity does not change, which is understandable if thought of in terms of the energy barrier distribution discussed in section 5.1.3. The energy barrier for the Cr buffered films will show a substantial peak at the energy corresponding to H_c, whereas those with no Cr buffer layer will have a much wider and flatter distribution. This accounts for both the low remanence and increased saturation field. However, the distribution is balanced at the same point as that for the Cr buffered sample, resulting in similar values for H_c.

The change in behaviour is also symptomatic of a change in the inter-granular exchange coupling in the films. For the films with only an Ag seed layer the Co_2FeSi grains are almost 100% exchange decoupled. This means that the grains within the sample must reverse their magnetisation through independent nucleation events. As a result, this process becomes controlled by the distribution of particle sizes in the film which in these films is large, with a standard deviation of 0.37. On the other hand, the films with the Cr buffer layer have a hysteresis loop typical of a film with strong exchange coupling with high remanent magnetisation, M_r/M_s = 0.88. The reversal is not entirely exchange controlled as there is not a well-defined nucleation field. This

suggests that some of the grains have small enough volume to be thermally unstable. However, after the application of a sufficiently large reverse field, the exchange coupling dominates and reverses the magnetisation of the rest of the film. To evaluate Cr diffusion into a Co_2FeSi layer the effect of the thickness of the Ag layer was also tested. As discussed previously, Cr diffusion is reported to increase the coercivity of Co_2FeSi films. This is due to the relative ease with which Cr can substitute for Fe in the Heusler structure **[63]**.

However, in polycrystalline films this effect from the Cr is likely to occur although not by the same mechanism. These polycrystalline films are strongly exchange coupled, therefore the dominant reversal mechanism is domain wall motion, where a domain is composed of a large number of magnetic grains which are magnetised in the same direction. If the domain wall encounters a Co_2FeSi grain where the composition is Co_2CrSi or more likely ($Co_2Fe_{1-x}Cr_xSi$) this will pin the domain wall as the magnetocrystalline anisotropy for this compound is reported to be slightly larger **[46]**, thus increasing H_c. This effect is shown schematically in Figure 7.10, where the red grains show the progression of the reverse domain in a film. In the film with no Cr induced pinning sites, the reverse domain is larger and wall motion is unhindered by the pinning sites (green grains).

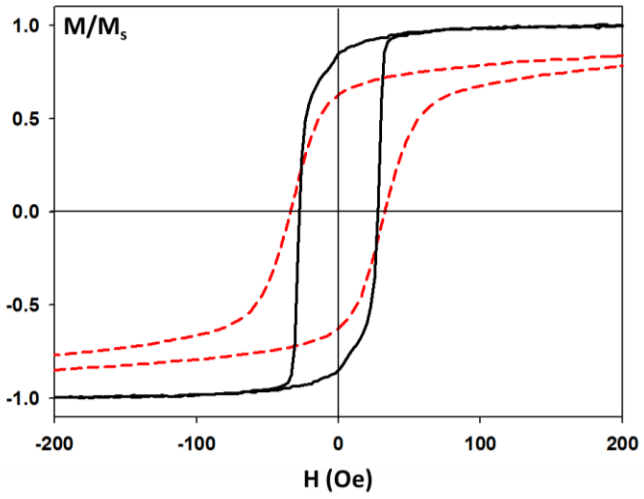

Figure 7.9. Hysteresis loops of polycrystalline samples deposited at V_B=850 V with a Cr/Ag seed layer (solid line) and just an Ag seed layer (dashed line).

Films were grown with Ag layers of thickness 6 nm, 15 nm and 30 nm with a 3 nm Cr buffer layer to measure the range over which Cr diffusion may occur. Figure 7.11a shows clearly how Cr diffusion affects the coercivity in these films. The

coercivity of the as-deposited films can be considered as the same, with slight variation due to random structural differences resulting from the growth process. The trend with annealing is more important. After heating for 1 hour the coercivity of the film with a 6 nm Ag seed layer has increased by 10 Oe, whilst the film with a 15 nm layer sees a smaller increase of only 2.5 Oe. The film with a 30 nm thick Ag seed layer shows a small decrease in H_c. This would suggest that annealing at 300°C encourages Cr diffusion through the Ag layer when the thickness is less than 30 nm. Beyond 2 hours annealing the coercivity remains constant suggesting that for all films Cr diffusion stops.

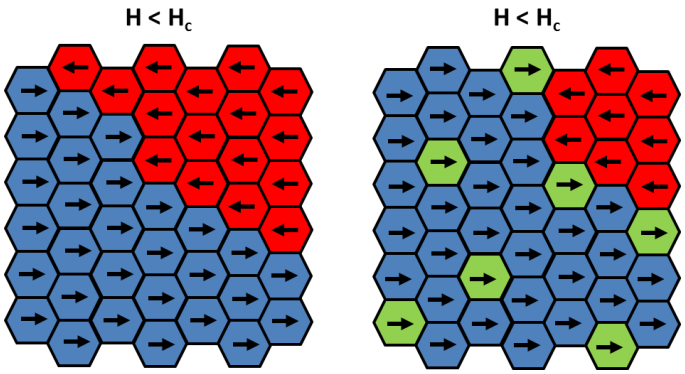

Figure 7.10. Schematic diagram showing the difference between pinned and unpinned domain wall motion in a strongly exchange coupled polycrystalline film. The blue and red grains represent the initial magnetisation direction and the reverse domain respectively. The green grains are Cr doped high anisotropy pinning sites.

Figure 7.11b shows that the increase in Ag layer thickness does not result in a return to the island growth. Island growth would exchange decouple the grains and reduce M_r/M_s by initiating reversal at lower fields. The figure shows that M_r/M_s remains constant with Ag layer thickness, showing that the Co_2FeSi grains remain exchange coupled. The decrease in H_c comes from a reduction in the anisotropy within the grains that are acting as pinning sites. The energy and therefore field required to overcome these pinning sites is lower, resulting in the observed decrease in H_c. All the films nucleate reversal at approximately the same field (30 Oe). The main difference in the loops comes from the point at which the large reversal step takes place. This field corresponds to the energy require to overcome the Cr induced domain wall pins and therefore controls the coercivity. In Co-based recording media, Cr segregation has been shown previously to reduce exchange coupling **[160]**. This is due to the segregation of the Cr to the grain boundaries. It has also been shown that the exchange coupling between grains increases with lower Cr levels **[59]**. However, in

the Co_2FeSi films in this work, the lack of variation in M_r/M_s would suggest no change in the exchange coupling in these films. This gives support to the idea that the Cr diffusion affects the anisotropy of the grains and increases the energy barrier to reversal, instead of manipulating the inter-granular exchange coupling. However, this would need to be a substantial increase in the magnetocrystalline anisotropy as the shape anisotropy for individual grains would be dominant according to the calculation shown in Figure 2.4

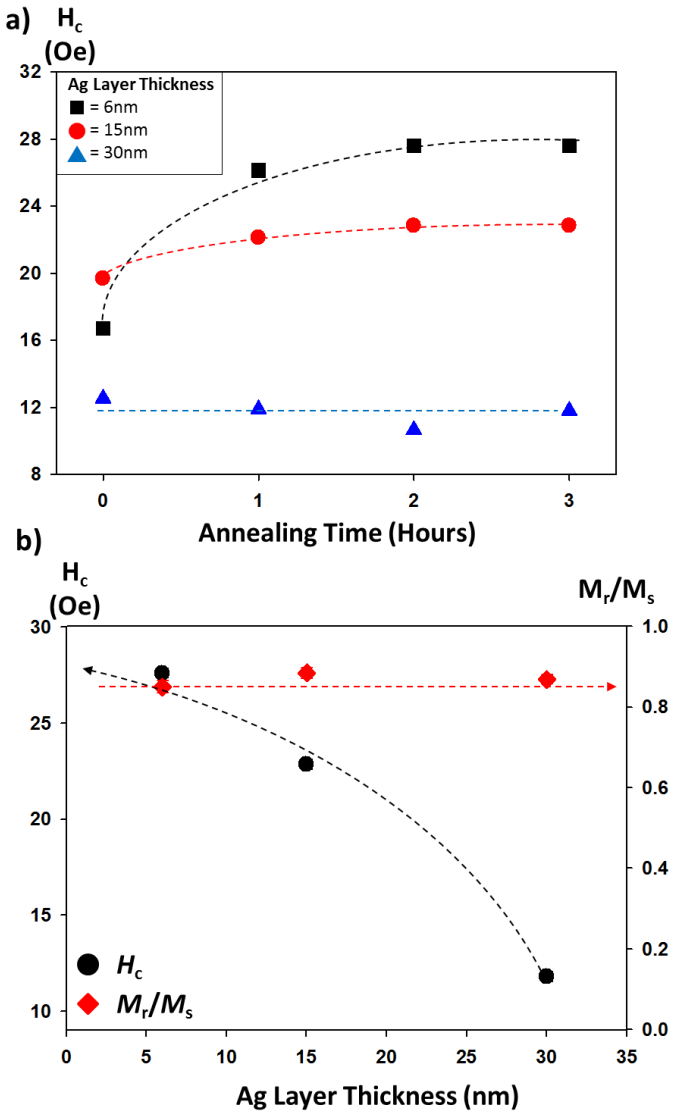

Figure 7.11. a) Graph showing the change in H_c with annealing time for polycrystalline Co_2FeSi films with 3 nm Cr buffer layer and Ag seed layers with thicknesses of 6 nm, 15 nm and 30 nm. b) Graph showing the variation of H_c (circles) and M_r/M_s (rhombuses) as a function of Ag seedlayer thickness in the same films. Trend lines are shown as a guide to the eye.

7.5. Antiferromagnetic Seed Layers

7.5.1. Exchange Bias

By using an antiferromagnetic seed layer the Co_2FeSi film can be exchange biased. Exchange bias is described as the pinning of the magnetisation of a ferromagnetic (F) layer in one direction due to the effect of an adjacent antiferromagnetic (AF) layer after field annealing. Initially discovered in 1956 **[161]**, exchange bias was little more than a curiosity until the discovery of the GMR effect **[12,13]**, after which it became widely researched due to its technological importance in spin-valve sensors.

In essence, exchange bias is a product of exchange coupling between the ferromagnetic and antiferromagnetic layers when the system is field annealed. The AF layer contributes an extra unidirectional anisotropy field to the F layer, the result of which is the pinning of the F layer in the direction in which that anisotropy acts. This is shown schematically in Figure 7.12. Experimentally, this can be achieved by heating the bilayer through the Néel temperature of the AF layer, then field cooling the stack back below the ordering temperature. This sets the direction of the AF layer and as a result the additive anisotropy to the F layer. In practice however it is often unfeasible to achieve heating through the Néel temperature. In this situation the direction of the AF layer is set by the thermal activation of a fraction of grains in the film. The observable effect of this is a shift in the hysteresis loop away from the symmetry about zero field.

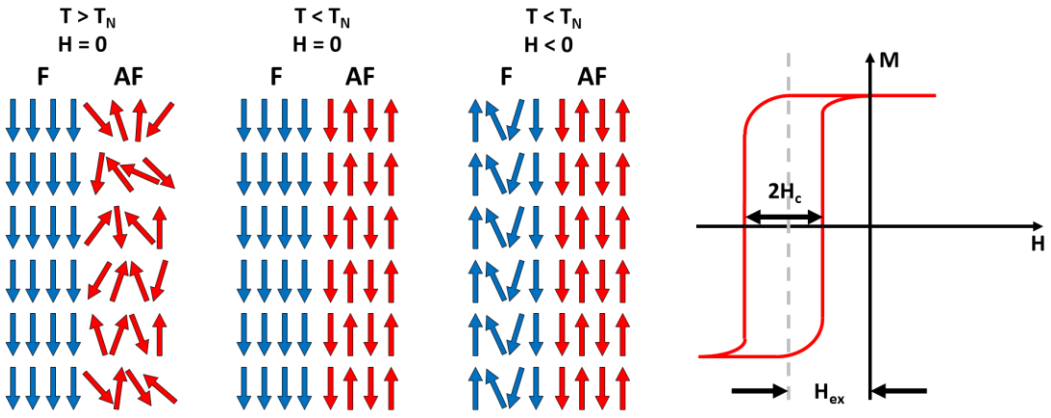

Figure 7.12. Schematic showing the directional pining of ferromagnetic spins at the F/AF interface. The effect of this pinning on the hysteresis loop of this bilayer is also shown **[47]**.

If polycrystalline Heusler alloys are going to be commercially viable in either hard drive read heads or STT-MRAM bits then one layer must have the magnetisation direction pinned. In single crystal films the effective uniaxial anisotropy is enough to pin one layer once nanoscale features are patterned. For the polycrystalline films this is not the case. As shown earlier in this chapter these display a 2D random anisotropy. This must therefore be made uni-directional by exchange biasing.

7.5.2. Film Structure

To induce the maximum exchange bias effect, IrMn with a NiCr seed layer was deposited before the Co_2FeSi. IrMn with a NiCr seed layer has previously been shown to produce exchange biased films with extremely well controlled parameters **[162,163]**. This is because the IrMn is forced to grow with the (111) planes parallel to the substrate. As it is these (111) planes that couple antiferromagnetically in IrMn, keeping them within the plane of the film is crucial to providing a large exchange bias.

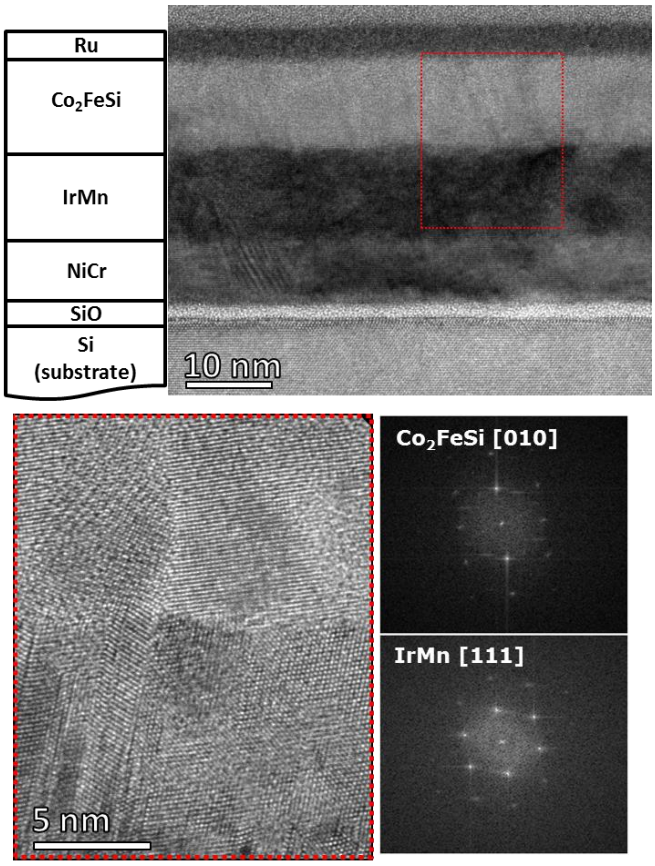

Figure 7.13. Cross section HRTEM images of exchange biased Co_2FeSi thin films with FFTs of Co_2FeSi and IrMn grains.

To check this alignment of the IrMn specimens were deposited using the HiTUS system with a constant V_B of 850 V for all layers. The films were then imaged in cross section using HRTEM. As previously found for the Cr/Ag seed layer the films have only a small surface roughness (< 1 nm) with an interface roughness of the same order. From FFTs of the individual layers it was found that both the NiCr and IrMn layers are strongly textured with their (111) planes in the plane of the film. The Co_2FeSi film however has a distribution of orientations. Growth with the (010) planes textured into the plane of the substrate appears most commonly. The fast Fourier FFTs of single grains in the film show the diffraction pattern of the (111) orientation for IrMn and the diffraction pattern of the (010) planes for Co_2FeSi.

To understand the effect of this seed layer on the exchange bias another set of specimens were grown, with variation of the deposition bias voltage to the NiCr and IrMn layers. NiCr/IrMn seed layers were deposited with sputter bias voltages of 500 V and 990 V. This resulted in a median grain diameter of (7.5 ± 0.3) nm for the film deposited with V_B = 500 V and (10.5 ± 0.3) nm with V_B = 990 V. These median diameters were calculated by measuring the lateral diameters of 100 grains in the cross section images like those in Figure 7.13. This method is not as accurate as using the Zeiss Particle analyser as was previously used for plan view samples. This method does have the advantage of being able to measure only the grains in specific layers. This is of particular interest in these films due to the change of bias voltage for some layers, whilst the Co_2FeSi layer was always deposited with V_B = 990 V. This resulted in a typical grain diameter of 18 nm, however, the statistics could not be performed on these grains due to their increased size and thus reduced number in the observable areas of the film cross-section.

7.5.3. Magnetic Measurements

The variation in seed layer grain size has a strong effect on the magnetic properties of the thin films. All films show the characteristic exchange biased loop shift. However, the film with the IrMn layer deposited with V_B = 990 V shows an exchange bias (H_{ex}) four times that of the film with the IrMn deposited with V_B=500 V. This is shown in Figure 7.14a.

Figure 7.14b shows how these values of H_{ex} vary as a function of both the IrMn layer thickness and the temperature at which the film was set. There is a monotonic increase in H_{ex} with the setting temperature, whilst the variation in H_{ex} with film

thickness is more complex. H_{ex} peaks for an IrMn film thickness of 7 nm and then gradually decreases. Both the temperature dependence and thickness dependence of the exchange bias can be explained using the York Model of exchange bias **[164]**

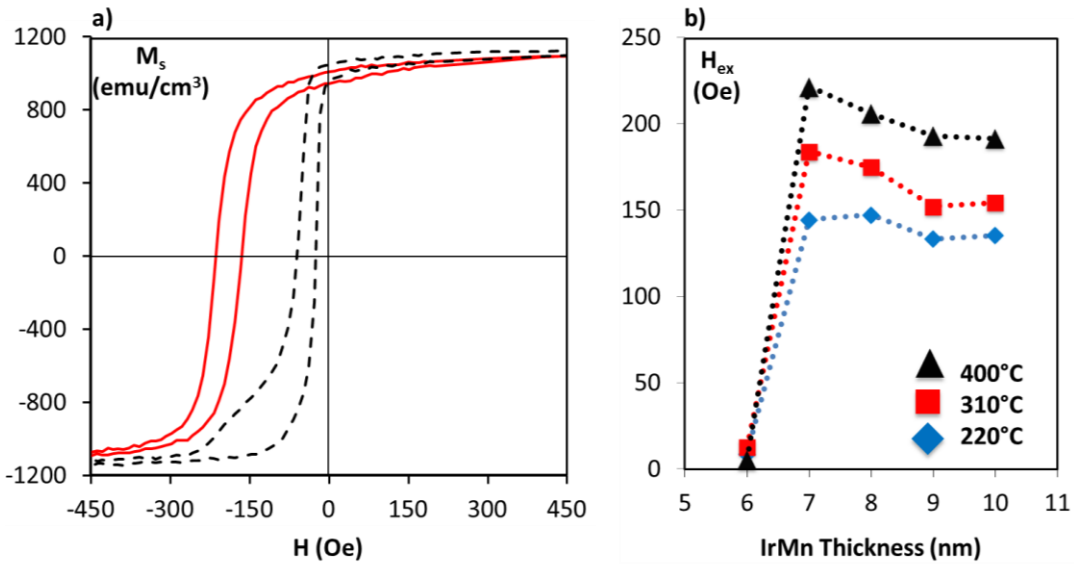

Figure 7.14. a) Hysteresis loops of thin films with IrMn deposited at V_B = 500 V (dashed line) and V_B = 990 V (solid line). b) Variation of H_{ex} with IrMn thickness for specimens deposited with V_B =990 V.

The York Model of exchange bias describes H_{ex} as being due to the fraction of antiferromagnetic grains which are 'set' in the exchange biasing direction. The fraction comes from grains whose volumes lie between the limits of the integral in equation 7.2.

$$H_{ex} = C^* \int_{V_c}^{V_{set}} f(V) dV \qquad (7.2)$$

V_c is the critical volume below which the grains are thermally unstable and V_{set} is the volume above which it is impossible to set the grains at a given temperature or field. The coefficient C^* is the interfacial exchange stiffness and contains information about the exchange coupling between the antiferromagnet and the ferromagnet as well as the strength of the uniaxial anisotropy induced by the exchange bias. It is assumed that for these samples C^* remains constant and only the grain volume distribution is affected. The effect of the sputtering bias is shown schematically in Figure 7.15.

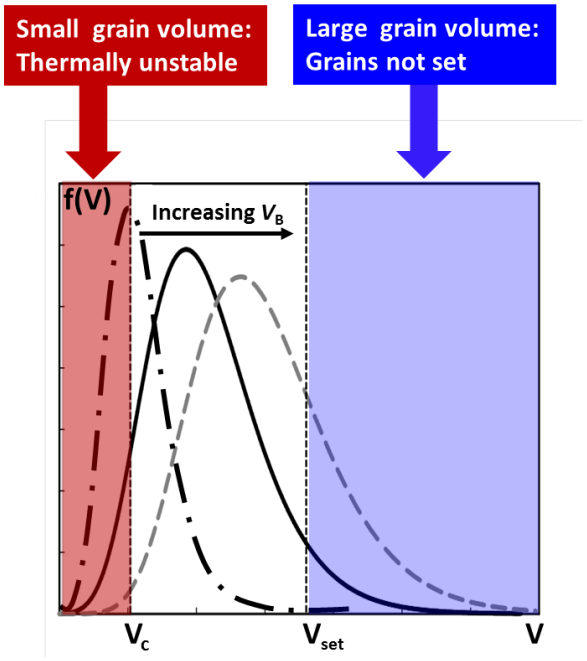

Figure 7.15. Schematic diagram of the effect of V_B in the York Model of exchange bias, where V is the volume of a grain in the antiferromagnetic layer..

The thickness dependence arises due to the shifting of the distribution inside the limits of the integral. This is best explained by describing the grain volume using equation 7.3:

$$V_{AF} = \frac{\pi D^2 t_{AF}}{4}. \qquad (7.3)$$

The grains are modelled as cylinders through the film thickness. Therefore the diameters are distributed following a lognormal function through the deposition process. However, the volume varies linearly with the thickness (t_{AF}) and this acts to shift the distribution within the limits of the integral, V_c and V_{set}.

This shows that it is possible to exchange bias polycrystalline Co_2FeSi films deposited using the HiTUS system. It is also possible to control the strength of the exchange bias through control of the grain size. This fits exactly with previously published material on conventional magnetic materials **[164]**.

7.5.4. Interfacial Mn Doping

Following the work of *Tusnoda et al.* **[165]**, the IrMn/Co_2FeSi interface has been doped with Mn to improve the exchange bias. This technique was shown to increase the exchange bias in IrMn/CoFe systems by 20% with an interfacial Mn doping of 0.3 nm,

roughly a single Mn monolayer. The system that showed the smallest exchange bias from the previous experiment was used, that is a 6 nm thick IrMn film deposited with an applied bias voltage of 990 V. This was used to demonstrate the largest possible effect from any dopant layer. The effect of this Mn layer was dramatic, as shown in Figure 7.16. Any variation in the exchange bias of, an un-doped film between this and previous studies is due to variation in film structure from deposition to deposition.

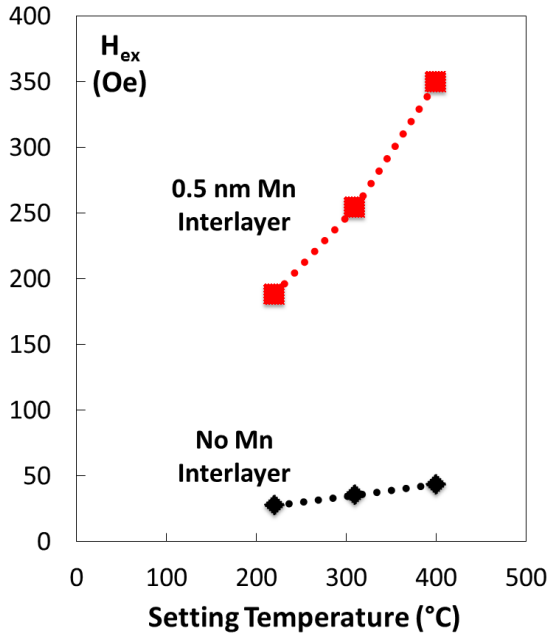

Figure 7.16. The effect of Mn interface doping on H_{ex} as a function of setting temperature.

It can be seen from Figure 7.16 that the Mn interface layer has a large effect on $H_{ex,}$ increasing H_{ex} by a minimum of 150 Oe. Even more unusual is the setting temperature dependence of the exchange bias. For the system without the Mn doping, the setting temperature has only a small effect (approximately 25 Oe). For the doped system, H_{ex} is shown to increase by 175 Oe over the 200°C temperature variation. There are a number of possible reasons for this increase and more significantly the difference in trends between the doped and un-doped systems. This is clearly not an effect of the volume distribution, therefore the Mn must affect the other term in equation 7.2. *Tsunoda et al.* **[165]** attributed this increase in H_{ex} to an increase in the effective anisotropy at the interface. However, the trend they measured with temperature is in fact the opposite of that shown here. We must consider therefore the other possible effects. The increased setting temperature is also likely to increase the diffusion of Mn into the surrounding layers. Figure 7.17 shows that the

IrMn/Co_2FeSi interface is significantly more diffuse in the film with a 0.5 nm Mn interlayer. This diffusion of Mn is likely to alter the composition of the Heusler alloy in the interface region, forming some composition of $Co_2Fe_{1-x}Mn_xSi$. Because of the changes in orbital hybridisation in this alloy it is possible that this alloy intrinsically couples more effectively to IrMn that the Co_2FeSi alone. This Mn diffusion may also act to replenish Mn in the IrMn layer which diffuses away from the interface during annealing, leaving a Mn deficient phase of IrMn at the interface. This would again affect the intrinsic interface coupling.

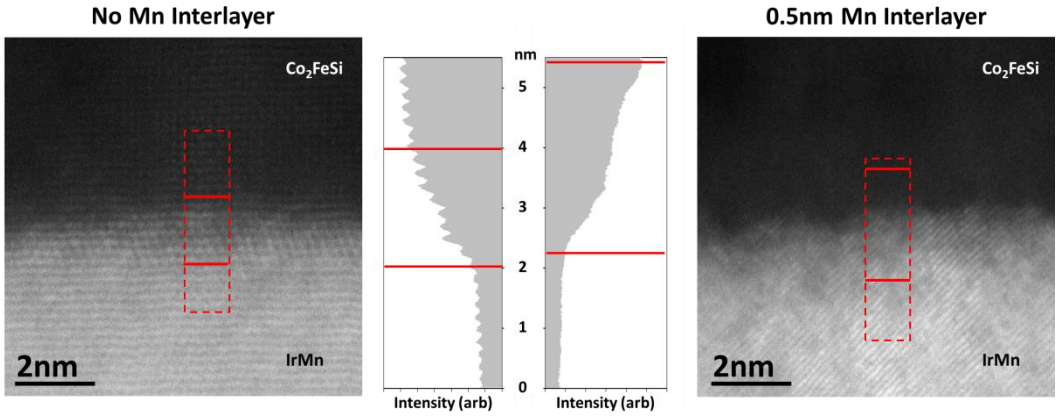

Figure 7.17. HRSTEM images of the IrMn/Co_2FeSi interface with and without the Mn interlayer. Intensity profiles across the highlighted regions show interface thickness.

The amount of control of the magnetic properties in these Heusler alloy films through the use of seed layers is astounding. It has been shown that the coercivity, loop squareness and exchange bias can all be controlled effectively through the appropriate choice of seed layer. Looking forward to the applicability of these films for device structures, it has been shown that a pinned layer in a spin valve or MTJ could be created either through exchange biasing or by control of Cr diffusion to create a high coercivity layer. The use of Cr buffer layers also maximises the loop squareness which is necessary for the free layer in devices to attain thermal stability. Possibly most important for Heusler alloy films is that these seed layers promote crystallisation of the Heusler layer into $L2_1$ and $B2$ phases. These optimised Co_2FeSi properties open up the possibility of using these films in devices.

Chapter 8. Conclusions and Further Work

8.1. Conclusions

In this work the magnetic properties of Co-based Heusler alloy compounds have been correlated with their complex microstructure. Both polycrystalline and epitaxial films have been grown using HiTUS and magnetron sputtering.

The films deposited using a HiTUS system were found to be polycrystalline with large grains forming out of an as-deposited amorphous or nano-crystalline matrix of the atomic components of the alloy after heating. These films have a wide range of magnetic properties due to the large distribution of structural properties, primarily grain sizes and phases of ordering. The polycrystalline films have a range of median diameters from 30 nm to 100 nm. In contrast, the activation volume in these films shows very little variation, typically giving activation volumes with an equivalent activation diameter of 40 - 50 nm. As a result, the polycrystalline films change from a system where magnetisation reversal is controlled by rotation of the magnetisation through the grain volume to a situation where multiple magnetic domains exist in a grain, and the magnetisation reversal mechanism is domain wall motion. The transition between these two regimes results in a number of oddly shaped hysteresis loops which exhibit two phases of magnetisation reversal.

From SAED and HRTEM it is found that these grains show extremely good crystalline ordering. However, due to the crystal growth mechanisms, the large grains in these films result from the coalescence of two or more grains. This results in regions of structural disorder in the grains which act as domain wall pins. The effect of this is seen in the hysteresis loops of the films with an increased fraction of larger grains, where the increased coercivity is the result of pinned domain wall motion. The

majority of these grains are found to lie with their [111] direction out of the plane of the film. This is the result of each of the initial grains crystallising layer-by-layer from the as-deposited matrix.

Epitaxially sputtered films are found to exhibit long range $L2_1$ ordering. This has been confirmed by both HRSTEM as well as XRD. The extent of the ordering is annealing temperature dependent. The typical size of $L2_1$ ordered regions increases from (70±15) nm in the as-deposited state to (374±8) nm after annealing at 600°C. The increase in extent of crystalline ordering results in an increase of the nucleation field for magnetisation reversal. The activation volumes in these films are however an order of magnitude smaller than those in polycrystalline films, with typical activation diameters of ~5 nm. They also show little or no annealing temperature dependence. The activation volume was found to correspond to the spacing between misfit dislocations at the film/substrate interface.

Although the polycrystalline Heusler alloy films provide a potential route to improved magnetic behaviour due to the large activation volumes, the large variation in both structural and magnetic properties must be controlled. Through the use of seed layers this has been achieved. Ag seed layers have been found to reduce the coercivity to less than 50 Oe for all grain sizes, whilst also increasing the saturation magnetisation of the films to greater than 80% of the M_s of bulk Co_2FeSi. These films did however show reduced loop squareness (M_r/M_s = 0.46) as the result of segregation of the Co_2FeSi grains. This arises from the island growth of the Ag seed layer.

The island growth of the Ag seed layer can be removed through the deposition of a 3 nm Cr buffer layer. This restores the loop squareness as the grains in the film are now exchange coupled. The Cr diffusion through the Ag layer does however result in an increase in coercivity. This is the result of the Cr implanting in the Co_2FeSi forming regions of higher anisotropy which stabilise the magnetisation of the film to the application of a field. This Cr diffusion can be controlled through increasing the thickness of the Ag layer resulting in a reduction in the coercivity back to those values found previously for the films without the Cr buffer, typically 12 – 30 Oe.

Antiferromagnetic seed layers were also tested to understand the effect of exchange biasing Heusler alloys. Using an optimised NiCr (7 nm)/ IrMn (7 nm) seed layer an exchange bias of up to 200 Oe was achieved. This exchange bias was

improved through the use of Mn interfacial doping. By inserting a 0.5 nm Mn layer at the IrMn/Co_2FeSi interface the exchange bias was increased to 375 Oe. From cross sectional STEM it was found that this Mn layer increases the interface roughness, showing diffusive contrast out to 10 monolayers, whereas the film without the Mn interlayer only showed this diffusion up to 4 monolayers. Although this roughness may affect the exchange bias, it is more likely that this inter-diffusion changes the atomic composition at the interface, thus increasing the AF/F exchange coupling and as a result the exchange bias.

Through the use of seed layers it was possible to tailor both the structure and magnetic properties of polycrystalline Heusler alloys. It was possible to achieve values of saturation magnetisation up to 90% of that of bulk Co_2FeSi. The ordered grains in these films also appear to be $L2_1$ or $B2$ ordered from SAED and HRTEM. However, the degree of spin polarisation achievable from these films remains uncertain as devices through which this could be measured have not been fabricated.

8.2. Future Work

8.2.1. Observation of Domain Structures

In order to truly understand the reversal mechanisms in both the single crystal and polycrystalline films the domain mechanisms must be observed directly. There are a number of techniques that allow this, principally Kerr effect microscopy, magnetic force microscopy (MFM) and Lorentz TEM. Each of these techniques has their own distinct advantages and disadvantages. However, a combination of these techniques would give a more complete picture of the complex magnetisation reversal processes in these films. Kerr microscopy has previously been carried out on single crystal films of the similar alloy $Co_2CrFeAl$ **[67]**. By taking images at different points along the hysteresis loop it was possible to image the progress of domain wall motion. However, this was not a dynamic measurement and the resolution is limited such that the *Barkhausen* jumps that define the activation volume may be below both the optical and time resolution limit. Kerr microscopy may however be able to shed some light on the origin of the uniaxial anisotropy in the single crystal films measured in this work, as was previously demonstrated in **[67]**.

To achieve the resolution necessary to image the 5 nm activation diameters Lorentz TEM must be considered. MFM has not been widely used in Heusler systems,

but demonstrations in other systems would suggest that this technique could be applicable to the thin films in this work. MFM has been demonstrated at a resolution of below 30 nm, making it potentially able to image the domain structure of single grains in the polycrystalline films in this work. Unfortunately, it is not usually possible to apply large fields in conventional MFM systems, which may make certain parts of the hysteresis loops difficult to access.

Lorentz TEM may provide the best possible technique for the direct observation of magnetisation reversal processes due to its high resolution (<10 nm). This has been demonstrated in a number of systems, though recently it has primarily been used to observe domain processes in nanowires for racetrack memory **[166]**. New advances in microscope technology may also allow nanometre resolution for Lorentz TEM, although as yet nothing has been published on these systems. For the polycrystalline films, this technique should be immediately applicable due to the previously demonstrated grain growth in these films when deposited onto TEM grids. For single crystal films, this technique is potentially much more difficult because the films must be thinned. This will change the magnetic properties of the films dramatically. This would make it difficult to correlate the Lorentz TEM results with the magnetic measurements.

8.2.2. Device Fabrication

The next step in this work would be the fabrication of nano-pillar GMR devices to perform measurements of magnetoresistance, as well as to demonstrate spin transfer torque induced switching in these materials. Recently, fabrication of pseudo-spin valves has been reported in polycrystalline Heusler alloy systems. These systems demonstrated CPP-GMR in both $Co_2Fe(Al_{0.5},Si_{0.5})$ and $Co_2Fe(Ga_{0.5}Ge_{0.5})$ based devices **[44]**. Relatively high GMR values of up to 10% at room temperature were reported. The devices also had low resistance when compared to previous Heusler alloy based devices **[44]**. The other important step in this study was the use of low annealing temperatures, typically 235°C but with a maximum of 350°C. This demonstrated the feasibility of the use polycrystalline Heusler alloys for commercial applications such as hard disk drive read heads. Although exceptionally high TMR values were previously demonstrated using single crystal films these required much higher annealing temperatures of above 500°C **[34]**.

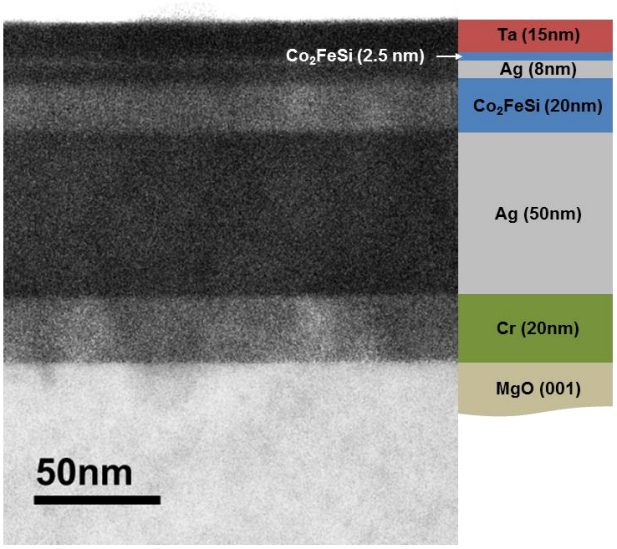

Figure 8.1. TEM image of a potential device film.

As a step towards creating a device, films have been deposited using the HiTUS system with structures similar to those used in these devices. Cross-section TEM images of these films are shown in Figure 8.1. The figure shows that these films are approaching the required properties for device structures. The interfaces in the film have low roughness, <1 nm, whilst also demonstrating single step magnetisation reversal. Figure 8.1 also shows that the 2.5 nm thick free layer remains continuous over the entire area imaged. After imaging a number of areas it was found that this layer was continuous across the entire film. These films have yet to be patterned into devices and their electronic properties measured.

List of Symbols

a	Lattice constant for cubic material
a_o	Atomic radius
A_{ex}	Exchange stiffness coefficient
$A(u)$	Aperture term in the contrast transfer function
$B(u)$	Aberration term in the contrast transfer function
β	Full width half maxima of diffraction peak
C_s	Spherical aberration coefficient
$\gamma(n)$	Chemical potential of a system with n atoms
γ_∞	Chemical potential of a substrate
γ_a	Chemical potential of an adatom
γ_{gm}	Gyromagnetic ratio
χ_{irr}	Irreversible susceptibility
d_{hkl}	Reciprocal space atomic plane spacing
D_{act}	Magnetic activation diameter
D_m	Median grain diameter
D_{XRD}	Crystallite size from X-ray diffraction
δ	Domain wall width
E_{act}	Bonding activation energy
E_F	Fermi Energy
E_{ex}	Exchange energy
E_K	Anisotropy energy
E_{ms}	Magnetostatic energy
$E(u)$	Envelope term in the contrast transfer function
ΔE	Energy barrier to reversal
$\eta(u)$	Exponent solution to the contrast transfer function
f_0	Attempt frequency
Δf	Defocus value
F_i	Force exerted in direction i
$\boldsymbol{g}$	Laue vector for reciprocal space atomic plane
$\boldsymbol{g_B}$	Laue vector for reciprocal space atomic plane meeting the Bragg condition
h,k,l	Miller indices
H_c	Coercive Field
H_{ex}	Exchange bias field
H_f	Fluctuation field
H_i	External magnetic field in direction i
H_K	Anisotropy field
H_n	Reverse domain nucleation field
J_{ex}	Exchange integral
$K_{0,1,2}$	Magnetocrystalline anisotropy constants
K_s	Shape anisotropy constant
$\boldsymbol{L}$	Laue vector describing difference between incident and exit radiation
$\boldsymbol{L_B}$	Laue vector for radiation meeting the Bragg condition
M	Magnetisation
M_r	Remanent magnetisation
M_s	Saturation magnetisation
m^*	Effective electron mass

N_d	Shape demagnetising factor
N_v	Number of valence electrons
$N_{\text{f.u.}}$	Number of valence electrons per formula unit
λ_e	Electron wavelength
λ_X	X-ray wavelength
Φ	Magnetic flux
$P_{1\,(2)}$	Spin polarisation of device electrode 1 (2)
$\rho_{\uparrow(\downarrow)}$	Resistivity of spin up (down) charge carriers
$\rho_P(T)$	Thermal resistivity
$\rho_{\uparrow\downarrow}$	Thermal spin scattering resistivity
r_a	Atomic separation
r_d	Radius of an electron *d* orbital
$\mathbf{S}_{i(j)}$	Spin angular momentum of atom *i* (*j*)
$S_1(H)$	1st Order magnetic viscosity coefficient
$S_2(H)$	2nd Order magnetic viscosity coefficient
$s_{\uparrow(\downarrow)}$	Fraction of electrons with spin up (down)
$\sigma_{\ln D}$	Standard deviation of ln(*D*)
$T(u)$	Contrast transfer function (CTF)
t_A	Annealing time
T	Magnetisation relaxation time
τ_{STT}	Spin transfer toque
θ_B	Bragg angle
Θ	Debye temperature
U	Spatial frequency
μ_i	Magnetic moment in direction *i*
ν_{res}	Resonant frequency
ν_{cg}	Crystal growth velocity
ν_o	Atomic jump frequency
V_{act}	Magnetic activation volume
V_B	HiTUS sputtering bias voltage
$\overline{x}_{\ln D}$	Mean of ln(*D*)

List of Abbreviations

AGFM	Alternating gradient force magnetometer
AMR	Anisotropic magnetoresistance
CIP	Current-in-plane
CMOS	Complementary metal-oxide-semiconductor
CPP	Current-perpendicular-to-plane
DCD	DC demagnetised
DRAM	Dynamic random access memory
EDX	Electron dispersive X-ray spectroscopy
fcc	Face centred cubic
FFT	Fast Fourier transform
FWHM	Full width half maximum
GMR	Giant magnetoresistance
hcp	Hexagonal close packed
HiTUS	High target utilisation sputtering

HMF	Half metallic ferromagnet
(HR)STEM	(High resolution) Scanning transmission electron microscopy
(HR)TEM	(High resolution) Transmission electron microscopy
IRM	Isothermal remanence
MOSFET	Metal-oxide-semiconductor field effect transistor
MRAM	Magnetic random access memory
MTJ	Magnetic tunnel junction
RKKY	Ruderman Kittel Kasuya Yoshida
Spin-FET	Spin field effect transistor
STT	Spin transfer torque
TMR	Tunnelling magnetoresistance
VSM	Vibrating sample magnetometer
WBDF	Weak-beam dark-field
XRD	X-ray diffraction

References

1 Sze, S. M. & Ng, K. K. *Physics of Semiconductor Devices*. Wiley, (2006).
2 Moore, G. E. *Proceedings of the IEEE* **86**, 82-85, (1998).
3 Rizzo, B. D. *NVIDIA Introduces GeForce GTX TITAN: DNA Of The World's Fastest Supercomputer, Powered By World's Fastest GPU*, <http://nvidianews.nvidia.com/Releases/NVIDIA-Introduces-GeForce-GTX-TITAN-DNA-of-the-World-s-Fastest-Supercomputer-Powered-by-World-s-Fa-925.aspx> (2013).
4 Kim, N. S., Austin, T., Baauw, D., Mudge, T., Flautner, K., Hu, J. S., Irwin, M. J., Kandemir, M. & Narayanan, V. *Computer* **36**, 68-75, (2003).
5 Awschalom, D. D. & Flatte, M. E. *Nature Physics* **3**, 153-159, (2007).
6 Prinz, G. A. *Science* **282**, 1660-1663, (1998).
7 Prinz, G. A. *Journal of Magnetism and Magnetic Materials* **200**, 57-68, (1999).
8 Datta, S. & Das, B. *Applied Physics Letters* **56**, 665-667, (1990).
9 Thomson, W. *Proceedings of the Royal Society of London* **8**, 546-550, (1856).
10 Brataas, A., Kent, A. D. & Ohno, H. *Nature Materials* **11**, 372-381, (2012).
11 Parkin, S. S. P. *Physical Review Letters* **67**, 3598-3601, (1991).
12 Binasch, G., Grünberg, P., Saurenbach, F. & Zinn, W. *Physical Review B* **39**, 4828-4830, (1989).
13 Baibich, M. N., Broto, J. M., Fert, A., Van Dau, F. N., Petroff, F., Etienne, P., Creuzet, G., Friederich, A. & Chazelas, J. *Physical Review Letters* **61**, 2472-2475, (1988).
14 Mott, N. F. *Proceedings of the Royal Society of London. Series A, Mathematical and Physical Sciences* **153**, 699-717, (1936).
15 Mott, N. F. *Proceedings of the Royal Society of London. Series A, Mathematical and Physical Sciences* **156**, 368-382, (1936).
16 Campbell, I. A., Fert, A. & Pomeroy, R. *Philosophical Magazine* **15**, 977-983, (1967).
17 Fert, A. & Campbell, I. A. *Physical Review Letters* **21**, 1190-1192, (1968).
18 Thompson, S. M. *Journal of Physics D: Applied Physics* **41**, 093001, (2008).
19 Nakatani, T. M., Furubayashi, T. & Hono, K. *Journal of Applied Physics* **109**, 07B724-723, (2011).
20 Julliere, M. *Physics Letters A* **54**, 225-226, (1975).
21 Miyazaki, T. & Tezuka, N. *Journal of Magnetism and Magnetic Materials* **139**, 231-234, (1995).
22 Moodera, J. S., Kinder, L. R., Wong, T. M. & Meservey, R. *Physical Review Letters* **74**, 3273-3276, (1995).
23 Butler, W. H., Zhang, X. G., Schulthess, T. C. & MacLaren, J. M. *Physical Review B* **63**, 054416, (2001).
24 Ikeda, S., Hayakawa, J., Ashizawa, Y., Lee, Y. M., Miura, K., Hasegawa, H., Tsunoda, M., Matsukura, F. & Ohno, H. *Applied Physics Letters* **93**, 082508-082503, (2008).
25 Slonczewski, J. C. *Journal of Magnetism and Magnetic Materials* **159**, 1-7, (1996).
26 Berger, L. *Journal of Applied Physics* **55**, 1954-1956, (1984).
27 Maekawa, S., Valenzuela, S. O., Saitoh, E. & Kimura, T. *Spin Current*. OUP Oxford, (2012).
28 de Groot, R. A., Mueller, F. M., Engen, P. G. v. & Buschow, K. H. J. *Physical Review Letters* **50**, 2024-2027, (1983).
29 Felser, C. & Hilllebrands, B. *Journal of Physics D: Applied Physics* **40**, (2007).

30 Kandpal, H. C., Fecher, G. H. & Felser, C. *Journal of Physics D: Applied Physics* **40**, 1507, (2007).

31 Blum, C. G. F., Jenkins, C. A., Barth, J., Felser, C., Wurmehl, S., Friemel, G., Hess, C., Behr, G., Buchner, B., Reller, A., Riegg, S., Ebbinghaus, S. G., Ellis, T., Jacobs, P. J., Kohlhepp, J. T. & Swagten, H. J. M. *Applied Physics Letters* **95**, 161903-161903, (2009).

32 Keizer, R. S., Goennenwein, S. T. B., Klapwijk, T. M., Miao, G., Xiao, G. & Gupta, A. *Nature* **439**, 825-827, (2006).

33 Son, Y.-W., Cohen, M. L. & Louie, S. G. *Nature* **444**, 347-349, (2006).

34 Tezuka, N., Ikeda, N., Mitsuhashi, F. & Sugimoto, S. *Applied Physics Letters* **94**, 162504-162503, (2009).

35 Lazarov, V. K., Yoshida, K., Sato, J., Hasnip, P. J., Oogane, M., Hirohata, A. & Ando, Y. *Applied Physics Letters* **98**, 242508-242503, (2011).

36 Ambrose, T., Krebs, J. J. & Prinz, G. A. *Applied Physics Letters* **76**, 3280-3282, (2000).

37 Ebke, D., Schmalhorst, J., Liu, N. N., Thomas, A., Reiss, G. & Hutten, A. *Applied Physics Letters* **89**, 162506-162503, (2006).

38 Inomata, K., Okamura, S., Miyazaki, A., Kikuchi, M., Tezuka, N., Wojcik, M. & Jedryka, E. *Journal of Physics D: Applied Physics* **39**, 816, (2006).

39 Nakatani, T. M., Rajanikanth, A., Gercsi, Z., Takahashi, Y. K., Inomata, K. & Hono, K. *Journal of Applied Physics* **102**, 033916-033918, (2007).

40 Shan, R., Sukegawa, H., Wang, W. H., Kodzuka, M., Furubayashi, T., Ohkubo, T., Mitani, S., Inomata, K. & Hono, K. *Physical Review Letters* **102**, 246601, (2009).

41 Nakatani, T. M., Furubayashi, T., Kasai, S., Sukegawa, H., Takahashi, Y. K., Mitani, S. & Hono, K. *Applied Physics Letters* **96**, 212501-212503, (2010).

42 Sukegawa, H., Kasai, S., Furubayashi, T., Mitani, S. & Inomata, K. *Applied Physics Letters* **96**, 042508-042503, (2010).

43 Furubayashi, T., Kodama, K., Goripati, H. S., Takahashi, Y. K., Inomata, K. & Hono, K. *Journal of Applied Physics* **105**, 07C305-303, (2009).

44 Nakatani, T. M., Du, Y., Takahashi, Y. K., Furubayashi, T. & Hono, K. *Acta Materialia* **61**, 3695-3702, (2013).

45 Good, P. I. & Hardin, J. W. *Common Errors in Statistics (and How to Avoid Them)*. Wiley, (2009).

46 Trudel, S., Gaier, O., Hamrle, J. & Hillebrands, B. *Journal of Physics D: Applied Physics* **43**, 193001, (2010).

47 Cullity, B. D. & Graham, C. D. *Introduction to Magnetic Materials*. Wiley, (2009).

48 Heisenberg, W. *Z. Physik* **38**, 411-426, (1926).

49 O'Handley, R. C. *Modern Magnetic Materials: Principles and Applications*. Wiley, (1999).

50 Morrish, A. H. & Society, I. M. *The Physical Principles of Magnetism*. Wiley, (1965).

51 Ruderman, M. A. & Kittel, C. *Physical Review* **96**, 99-102, (1954).

52 Kasuya, T. *Prog. Theor. Phys.* **16**, 45-57, (1956).

53 Yosida, K. *Physical Review* **106**, 893-898, (1957).

54 Campbell, I. A. *Journal of Physics F: Metal Physics* **2**, L47, (1972).

55 Parkin, S. S. P., More, N. & Roche, K. P. *Physical Review Letters* **64**, 2304-2307, (1990).

56 Ashcroft, N. & Mermin, D. *Solid State Physics*. Thomson Learning, (1976).

57 Crangle, J. *Solid-State Magnetism*. Van Nostrand Reinhold, (1991).

58 Parkin, S. S. P., Bhadra, R. & Roche, K. P. *Physical Review Letters* **66**, 2152-2155, (1991).

59 O'Grady, K., Chantrell, R. & Sanders, I. *IEEE Transactions on Magnetics* **29**, 286-291, (1993).

60 Hirohata, A. & Otani, Y. in *Epitaxial Ferromagnetic Films and Spintronic Applications* (eds A. Hirohata & Y Otani) Ch. 9, 207-235 Research Signpost, (2009).

61 Trudel, S., Wolf, G., Hamrle, J., Hillebrands, B., Klaer, P., Kallmayer, M., Elmers, H.-J., Sukegawa, H., Wang, W. & Inomata, K. *Physical Review B* **83**, 104412, (2011).

62 Hashimoto, M., Herfort, J., Schonherr, H. P. & Ploog, K. H. *Applied Physics Letters* **87**, 102506-102503, (2005).

63 Hirohata, A., Kurebayashi, H., Okamura, S., Tezuka, N. & Inomata, K. *IEEE Transactions on Magnetics* **41**, 2802-2804, (2005).

64 Moosbuhler, R., Bensch, F., Dumm, M. & Bayreuther, G. *Journal of Applied Physics* **91**, 8757-8759, (2002).

65 Stoner, E. C. & Wohlfarth, E. P. *Philosophical Transactions of the Royal Society. Section A* **240**, 599-642, (1948).

66 Jiles, D. *Introduction to magnetism and magnetic materials, 2nd ed*. Chapman and Hall, (1998).

67 Hamrle, J., Blomeier, S., Gaier, O., Hillebrands, B., Schafer, R. & Jourdan, M. *Journal of Applied Physics* **100**, 103904-103904, (2006).

68 Néel, L. *Ann. Geophys.* **5**, (1949).

69 Suh, H.-J., Heo, C., You, C.-Y., Kim, W., Lee, T.-D. & Lee, K.-J. *Physical Review B* **78**, 064430, (2008).

70 Street, R. & Woolley, J. C. *Proceedings of the Physical Society. Section A* **62**, 562-572, (1949).

71 Gaunt, P. *Journal of Applied Physics* **59**, 4129-4132, (1986).

72 Néel, L. *J. Phys. Radium* **12**, 339-351, (1951).

73 Wohlfarth, E. P. *Journal of Physics F: Metal Physics* **14**, 155, (1984).

74 Street, R., Woolley, J. C. & Smith, P. B. *Proceedings of the Physical Society. Section B* **65**, 679, (1952).

75 El-Hilo, M., O'Grady, K. & Chantrell, R. W. *Journal of Magnetism and Magnetic Materials* **248**, 360-373, (2002).

76 Mee, C. D. & Daniel, E. D. *Magnetic recording technology*. McGraw-Hill, (1996).

77 Dutson, J. D., O'Grady, K., Bin, L., Kubota, Y. & Platt, C. L. *IEEE Transactions on Magnetics* **39**, 2344-2346, (2003).

78 Nishino, Y., Kato, M., Asano, S., Soda, K., Hayasaki, M. & Mizutani, U. *Physical Review Letters* **79**, 1909-1912, (1997).

79 Wernick, J. H., Hull, G. W., Geballe, T. H., Bernardini, J. E. & Waszczak, J. V. *Materials Letters* **2**, 90-92, (1983).

80 König, M., Wiedmann, S., Brüne, C., Roth, A., Buhmann, H., Molenkamp, L. W., Qi, X.-L. & Zhang, S.-C. *Science* **318**, 766-770, (2007).

81 Heusler, F. S., W.; Haupt, E. . *Verhandlungen der Deutschen Physikalischen Gesellschaft* **5**, 219-223, (1903).

82 Sukegawa, H., Wang, W., Shan, R., Nakatani, T., Inomata, K. & Hono, K. *Physical Review B* **79**, 184418, (2009).

83 Block, T., Felser, C., Jakob, G., Ensling, J., Mühling, B., Gütlich, P. & Cava, R. J. *Journal of Solid State Chemistry* **176**, 646-651, (2003).

84 Graf, T., Felser, C. & Parkin, S. S. P. *Prog Solid St Chem* **39**, 50-50, (2011).

85 Yamada, S., Sagar, J., Honda, S., Lari, L., Takemoto, G., Itoh, H., Hirohata, A., Mibu, K., Miyao, M. & Hamaya, K. *Physical Review B* **86**, 174406, (2012).

86 Galanakis, I., Dederichs, P. H. & Papanikolaou, N. *Physical Review B* **66**, 174429, (2002).

87 Fujii, S. I., Shoji, A. S. *Journal of the Physical Society of Japan* **64**, 6, (1995).

88 Meinert, M., Schmalhorst, J.-M., Glas, M., Reiss, G., Arenholz, E., Böhnert, T. & Nielsch, K. *Physical Review B* **86**, 054420, (2012).

89 Kandpal, H. C., Fecher, G. H., Felser, C. & Schönhense, G. *Physical Review B* **73**, 094422, (2006).

90 Wurmehl, S., Fecher, G. H., Kandpal, H. C., Ksenofontov, V., Felser, C., Lin, H.-J. & Morais, J. *Physical Review B* **72**, 184434, (2005).

91 Gercsi, Z. & Hono, K. *Journal of Physics: Condensed Matter* **19**, 326216, (2007).

92 Chadov, S., Fecher, G. H., Felser, C., Minar, J., Braun, J. & Ebert, H. *Journal of Physics D: Applied Physics* **42**, 084002, (2009).

93 Kohn, W. *Reviews of Modern Physics* **71**, 1253-1266, (1999).

94 Vladimir, I. A., Aryasetiawan, F. & Lichtenstein, A. I. *Journal of Physics: Condensed Matter* **9**, 767, (1997).

95 Slater, J. C. *Physical Review* **49**, 537-545, (1936).

96 Pauling, L. *Physical Review* **54**, 899-904, (1938).

97 Kübler, J. *Theory of Itinerant Electron Magnetism*. OUP Oxford, (2000).

98 Balke, B., Fecher, G. H. & Felser, C. *Applied Physics Letters* **90**, 242503-242503, (2007).

99 Kubota, T., Tsunegi, S., Oogane, M., Mizukami, S., Miyazaki, T., Naganuma, H. & Ando, Y. *Applied Physics Letters* **94**, 122504-122503, (2009).

100 Li, G.-N., Jin, Y.-J. & Lee Jae, I. *Chinese Physics B* **19**, 097102, (2010).

101 Takamura, Y., Nakane, R., Munekata, H. & Sugahara, S. *Journal of Applied Physics* **103**, 07D719-713, (2008).

102 Oogane, M., Shinano, M., Sakuraba, Y. & Ando, Y. *Journal of Applied Physics* **105**, 907C903-903, (2009).

103 Schneider, H., Jakob, G., Kallmayer, M., Elmers, H. J., Cinchetti, M., Balke, B., Wurmehl, S., Felser, C., Aeschlimann, M. & Adrian, H. *Physical Review B* **74**, 174426, (2006).

104 Sagar, J., Sukegawa, H., Lari, L., Lazarov, V. K., Mitani, S., O'Grady, K. & Hirohata, A. *Applied Physics Letters* **101**, 102410-102414, (2012).

105 Ksenofontov, V., Wojcik, M., Wurmehl, S., Schneider, H., Balke, B., Jakob, G. & Felser, C. *Journal of Applied Physics* **107**, 09B106-103, (2010).

106 Yang, F. J., Wei, C. & Chen, X. Q. *Applied Physics Letters* **102**, 172403-172404, (2013).

107 Niculescu, V., Budnick, J. I., Hines, W. A., Raj, K., Pickart, S. & Skalski, S. *Physical Review B* **19**, 452-464, (1979).

108 Miura, Y., Nagao, K. & Shirai, M. *Physical Review B* **69**, 144413, (2004).

109 Bruski, P., Erwin, S. C., Ramsteiner, M., Brandt, O., Friedland, K. J., Farshchi, R., Herfort, J. & Riechert, H. *Physical Review B* **83**, 140409, (2011).

110 Nagao, K., Miura, Y. & Shirai, M. *Physical Review B* **73**, 104447, (2006).

111 Kazutaka, A., Yoshio, M., Yasunori, S. & Masafumi, S. *Journal of Physics: Condensed Matter* **21**, 064244, (2009).

112 Yoshio, M., Hirohisa, U., Yoshihiro, O., Kazutaka, N. & Masafumi, S. *Journal of Physics: Condensed Matter* **19**, 365228, (2007).

113 Saito, T., Katayama, T., Ishikawa, T., Yamamoto, M., Asakura, D., Koide, T., Miura, Y. & Shirai, M. *Physical Review B* **81**, 144417, (2010).

114 Hashemifar, S. J., Kratzer, P. & Scheffler, M. *Physical Review Letters* **94**, 096402, (2005).

115 Shirai, M., ; Miura, Yoshio,; Abe, Kazutaka. in *Epitaxial Ferromagnetic Films and Spintronic Applications* (ed Atsufumi.; Otani Hirohata, Yoshichika) Ch. 8, 187-205 Research Signpost, (2009).

116 Sakuraba, Y., Hattori, M., Oogane, M., Ando, Y., Kato, H., Sakuma, A., Miyazaki, T. & Kubota, H. *Applied Physics Letters* **88**, 192508-192503, (2006).

117 Yuasa, S., Nagahama, T., Fukushima, A., Suzuki, Y. & Ando, K. *Nature Materials* **3**, 868-871, (2004).

118 Mavropoulos, P., Ležaić, M. & Blügel, S. *Physical Review B* **72**, 174428, (2005).

119 Tsunegi, S., Sakuraba, Y., Oogane, M., Takanashi, K. & Ando, Y. *Applied Physics Letters* **93**, 112506-112503, (2008).

120 Wang, W., Sukegawa, H., Shan, R., Furubayashi, T. & Inomata, K. *Applied Physics Letters* **92**, 221912-221913, (2008).

121 Vopsaroiu, M., Fernandez, G. V., Thwaites, M. J., Anguita, J., Grundy, P. J. & Grady, K. O. *Journal of Physics D: Applied Physics* **38**, 490, (2005).

122 Vopsaroiu, M., Thwaites, M. J., Rand, S., Grundy, P. J. & O'Grady, K. *IEEE Transactions on Magnetics* **40**, 2443-2445, (2004).

123 Hirohata, A., Ladak, S., Aley, N. P. & Hix, G. B. *Applied Physics Letters* **95**, 252506-252506-252503, (2009).

124 Fleet, L. R., Cheglakov, G., Yoshida, K., Lazarov, V. K., Nakayama, T. & Hirohata, A. *Journal of Physics D: Applied Physics* **45**, 032001, (2012).

125 Stuart, R. V. *Vacuum Technology, Thin Films, and Spluttering: An Introduction*. Academic, (1983).

126 Geiersbach, U., Bergmann, A. & Westerholt, K. *Journal of Magnetism and Magnetic Materials* **240**, 546-549, (2002).

127 Williams, D. B. & Carter, C. B. *Transmission Electron Microscopy: A Textbook for Materials Science. Spectrometry*. Plenum Press, (1996).

128 Rose, H. *Optik* **85**, 19-24, (1990).

129 Wall, J., Langmore, J., Isaacson, M. & Crewe, A. V. *Proceedings of the National Academy of Sciences* **71**, 1-5, (1974).

130 Cullity, B. D. & Stock, S. R. *Elements of X-Ray Diffraction (3rd Edition)*. Prentice Hall, (2001).

131 Flanders, P. J. *Journal of Applied Physics* **63**, 3940-3945, (1988).

132 O'Grady, K., Lewis, V. G. & Dickson, D. P. E. *Journal of Applied Physics* **73**, 5608-5613, (1993).

133 Richter, H. J., Hempel, K. A. & Pfeiffer, J. *Review of Scientific Instruments* **59**, 1388-1393, (1988).

134 Zijlstra, H. *Review of Scientific Instruments* **41**, 1241-1243, (1970).

135 Roos, W., Hempel, K. A., Voigt, C., Dederichs, H. & Schippan, R. *Review of Scientific Instruments* **51**, 612-613, (1980).

136 Chantrell, R. W. & Grady, K. O. *Journal of Physics D: Applied Physics* **25**, 1, (1992).

137 van de Veerdonk, R. J. M., Xiaowei, W. & Weller, D. *IEEE Transactions on Magnetics* **38**, 2450-2452, (2002).

138 El-Hilo, M., O'Grady, K. & Chantrell, R. W. *Journal of Magnetism and Magnetic Materials* **109**, L164-L168, (1992).

139 Foner, S. *Review of Scientific Instruments* **27**, 548-548, (1956).

140 Mallinson, J. *Journal of Applied Physics* **37**, 2514-2515, (1966).

141 Lu, K., Wang, J. T. & Wei, W. D. *Journal of Applied Physics* **69**, 522-524, (1991).

142 Scott, M. & Luborsky, F. *Butter-Worths Co. Ltd, London*, 151, (1983).

143 Lu, K. & Wang, J. T. *Journal of Crystal Growth* **94**, 448-454, (1989).

144 O'Grady, K. & Bradbury, A. *Journal of Magnetism and Magnetic Materials* **39**, 91-94, (1983).

145 Hirohata, A., Kikuchi, M., Tezuka, N., Inomata, K., Claydon, J. S., Xu, Y. B. & van der Laan, G. *Current Opinion in Solid State and Materials Science* **10**, 93-107, (2006).

146 Hÿtch, M. J., Snoeck, E. & Kilaas, R. *Ultramicroscopy* **74**, 131-146, (1998).

147 Rouviere, J.-L. & Sarigiannidou, E. *Ultramicroscopy* **106**, 1-17, (2005).

148 Lewis, V. G. *Development and Applications of an Alternating Gradient Force Magnetometer* Doctor of Philosophy Thesis, University of Wales, Bangor, (1995).

149 Gans, R. *Annalen der Physik* **407**, 28-44, (1932).

150 Joffe, I. & Heubergber, R. *Philosophical Magazine* **29**, 1051-1059, (1974).

151 Taniguchi, S. *Science reports of the Research Institutes, Tohoku University. Ser. A, Physics, chemistry and metallurgy* **7**, 12, (1955).

152 Costa-Krämer, J. L., Menéndez, J. L., Cebollada, A., Briones, F., García, D. & Hernando, A. *Journal of Magnetism and Magnetic Materials* **210**, 341-348, (2000).

153 Gaier, O. *A Study of Exchange Interaction, Magnetic Anisotropies, and Ion Beam Induced Effects in Thin Films of Co_2-Based Heusler Compounds* PhD Thesis, Technischen Universitat Kaiserslautern, (2009).

154 El-Hilo, M., O'Grady, K., Chantrell, R. W. & Dickson, D. P. E. *Journal of Magnetism and Magnetic Materials* **123**, 30-34, (1993).

155 Zander, M., Herfort, J., Kumakura, K., Scöhnherr, H. P. & Trampert, A. *Journal of Physics D: Applied Physics* **43**, 305004, (2010).

156 Herman, M. A., Richter, W. & Sitter, H. *Epitaxy: Physical Principles and Technical Implementation*. Springer, (2004).

157 Bauer, E. *Zeitschrift für Kristallographie - Crystalline Materials* **110**, 372-394, (1958).

158 Markov, I. V. *Crystal Growth for Beginners: Fundamentals of Nucleation, Crystal Growth and Epitaxy (2nd Edition)*. World Scientific, (2003).

159 Oogane, M., Yilgin, R., Shinano, M., Yakata, S., Sakuraba, Y., Ando, Y. & Miyazaki, T. *Journal of Applied Physics* **101**, 09J501-503, (2007).

160 Futamoto, M., Inaba, N., Hirayama, Y., Ito, K. & Honda, Y. *MRS Online Proceedings Library* **517**, null-null, (1998).

161 Meiklejohn, W. H. & Bean, C. P. *Physical Review* **102**, 1413-1414, (1956).

162 Aley, N. P., Vallejo-Fernandez, G., Kroeger, R., Lafferty, B., Agnew, J., Lu, Y. & O'Grady, K. *IEEE Transactions on Magnetics* **44**, 2820-2823, (2008).

163 Aley, N. P., Bowes, M., Kroger, R. & O'Grady, K. *Journal of Applied Physics* **107**, 09D722-723, (2010).

164 O'Grady, K., Fernandez-Outon, L. E. & Vallejo-Fernandez, G. *Journal of Magnetism and Magnetic Materials* **322**, 883-899, (2010).

165 Yagami, K., Tsunoda, M. & Takahashi, M. *Journal of Applied Physics* **89**, 6609-6611, (2001).

166 Basith, M. A., McVitie, S., McGrouther, D. & Chapman, J. N. *Applied Physics Letters* **100**, 232402-232405, (2012).

List of Publications

1. "Heusler-Alloy Films for Spintronic Devices (*Invited*)"
   A. Hirohata, J. Sagar, L. Lari, L. R. Fleet, and V. K. Lazarov
   Appl. Phys. A. **111**, 2, pp 423-430 (2013)

2. "Room-Temperature Structural Ordering of a Heusler Compound Fe_3Si"
   S. Yamada, J. Sagar, S. Honda, L. Lari, G. Takemoto, H. Itoh, A. Hirohata, K. Mibu, M. Miyao, and K. Hamaya
   Phys. Rev. B. **86**, 174406 (2012)

3. "The Effect of Seed Layers on Polycrystalline Co_2FeSi Thin Films"
   J. Sagar, C. N. T. Yu, C. Pelter, J. Wood, L. Lari, A. Hirohata, and K. O'Grady
   IEEE. Trans. Magn. **48**, 11, pp 4006-4009 (2012)

4. "The Effect of Interface Structure on Exchange Biased Heusler Alloy Films"
   H. Endo, A. Hirohata, J. Sagar, L. R. Fleet, T. Nakayama, and K. O'Grady
   IEEE. Trans. Magn. **48**, 11, pp 2896-2898 (2012)

5. "The Effect of Interfaces on Magnetic Activation Volumes in Single Crystal Co_2FeSi Heusler Alloy Thin Films"
   J. Sagar, H. Sukegawa, L. Lari, V. K. Lazarov, S. Mitani, L. O'Grady, and A. Hirohata
   Appl. Phys. Lett. **101**, 102410 (2012)

6. "Activation Volumes in Heusler Alloy Thin Films"
   J. Sagar, L. R. Fleet, A. Hirohata, and K. O'Grady
   IEEE. Trans. Magn. **47**, 10, pp 2440-2443 (2011)

7. "The Effect of Grain Size on Exchange-Biased Heusler Alloys"
   H. Endo, A. Hirohata, J. Sagar, L. R. Fleet, T. Nakayama and K. O'Grady
   J. Phys. D: Appl. Phys. **44**, 345003 (2011)

List of Presentations

1. J. Sagar, L.R. Fleet, K. O'Grady and A. Hirohata
"Activation Volumes in Heusler Alloy Thin Films"
Presented at **Intermag Conference 2011**, Taipei, Taiwan (**AO-09**)

2. H. Endo, A. Hirohata, J. Sagar, L. R. Fleet, T. Nakayama and K. O'Grady
"Effect of Grain Size on Exchange-Biased Heusler Alloys"
Presented at **Intermag Conference 2011**, Taipei, Taiwan (**AO-09**)

3. J. Sagar, L. R. Fleet, A. Hirohata and K. O'Grady
"Magnetic and Structural Characterisation of Co_2FeSi Polycrystalline Thin Films"
Presentated at **Spintech6 conference 2011**, Matsue, Japan (**FP-19**)

4. J.Sagar, H. Sukegawa, M. Hazenberg, L. Lari, V. K. Lazarov, S.Mitani, K. O'Grady and A. Hirohata
"Activation Volumes in Epitaxial Co_2FeSi Thin Films"
Presented at **56th MMM conference 2011**, Scottsdale, Arizona, USA (**CU-01**)

5. A. Hirohata, L. R. Fleet, M. J. Walsh, J. Sagar, G. Cheglakov, K. Yoshida, V. K. Lazarov, Y. Ohba and T. Nakayama
"Crystalline Formation of Polycrystalline Co-Based Full Heusler Alloy Films Observed by HRTEM with In-Situ Annealing (invited)"
Presented at **56th MMM conference**, Scottsdale, Arizona, USA (**AA-02**)

6. J. Sagar, H. Sukegawa, L. R. Fleet, L. Lari, V. K. Lazarov, S. Mitani and A. Hirohata
"Structure and Compositional Characterisation of Single Crystal and Polycrystalline Co_2FeSi Heusler Alloy Thin Films"
Presented at **CMMP 2011 conference**, Manchester, UK

7. L. R. Fleet, M. J.Walsh, J. Sagar, T. Nakayama, A. Hirohata
"Low Temperature In-Situ Crystallisation of Co_2FeSi Heusler Alloy Thin Films"
Presented at **Intermag conference 2012**, Vancouver, Canada (**EB-09**)

8. J. Sagar, C. Yu, C. Pelter, J. Wood, L. Lari, V. K. Lazarov, A. Hirohata, K. O'Grady
"Effect of Seed Layers on Polycrystalline Co_2FeSi Thin Films"
Presented at **Intermag conference 2012**, Vancouver, Canada (**FU-06**)

9. H. Endo, A. Hirohata, J. Sagar, L. R. Fleet, T. Nakayama, and K. O'Grady
"Effect of Interface Structure on Exchange Biased Heusler Alloy Films"
Presented at **Intermag conference 2012**, Vancouver, Canada (**AR-08**)

10. L. R. Fleet, M. J.Walsh, J. Sagar, T. Nakayama, A. Hirohata
"Low Temperature In-Situ Crystallisation of Co_2FeSi Heusler Alloy Thin Films"
Presented at **ICM conference 2012**, Busan, Korea (**SK-03**)

11. J. Sagar, H. Sukegawa, L. Lari, V. K. Lazarov, S. Mitani and A. Hirohata
"Characterisation of Epitaxial and Polycrystalline Co_2FeSi Thin Films"
Presented at **ICM conference 2012**, Busan, Korea (**SK-03**)

12. M. Rummey, J. Sagar, A. Vick, L. R. Fleet, Y. Zhang and A. Hirohata
"Structural and magnetic properties of epitaxial Fe:MgO anti-granular films"
Presented at **Joint MMM-Intermag conference 2013**, Chicago, USA (**EV-12**)

13. J. Sagar, L. Lari, A. Hirohata and K. O'Grady
"Optimisation of Seed Layers for Polycrystalline Co_2FeSi Heusler Alloy Thin Films"
Presented at **Joint MMM-Intermag conference 2013**, Chicago, USA (**AG-06**)

14. J. Sagar, C. Yu, H. Sukegawa, S. Mitani and A. Hirohata
"Control of polycrystalline Co_2FeSi grain structure using Ag seed layers and application to nanopillar devices"
Presented at **MML conference 2013**, Kyoto, Japan (**P-148**)

15. J. Sagar, H. Endo, C. N. T. Yu, L. R. Fleet, L. Lari, A. Hirohata and K. O'Grady
"The Effect of Seed Layers on Polycrystalline Co_2FeSi Thin Films" (Invited)
Presented at **JSPS York-Tohoku Symposium**, York, UK